Snake-inspired Aerial Gliding: Computational Analysis of the Fluid Dynamics and Aerodynamic Performances

---

A

Dissertation

Presented to

the faculty of the School of Engineering and Applied Science

University of Virginia

---

in partial fulfillment

of the requirements for the degree

Doctor of Philosophy

by

Yuchen Gong

May 2024

APPROVAL SHEET

This

Dissertation

is submitted in partial fulfillment of the requirements
for the degree of

Doctor of Philosophy

Author: Yuchen Gong

This Dissertation has been read and approved by the examing committee:

Advisor: Haibo Dong

Advisor:

Committee Member: Chloe Dedic

Committee Member: Daniel Quinn

Committee Member: Sarah Sun

Committee Member: Matthew Reidenbach

Committee Member:

Committee Member:

Accepted for the School of Engineering and Applied Science:

Jennifer L. West, School of Engineering and Applied Science

May 2024

Abstract

Small animals' locomotion, such as swimming, flapping, walking, and gliding motivated many bio-inspired robots. The flying snake happens to be a very unique species and a good representative of gliders. This research conducts a comprehensive numerical analysis on the aerodynamic phenomena of flying snakes, particularly focusing on their unique mode of locomotion known as aerial undulation. By simulating the flow dynamics around a bio-inspired snake-like model, this study extends the understanding of how Chrysopelea, the flying snake, utilizes a combination of horizontal and vertical undulations during gliding to manipulate airflow and enhance aerodynamic performance.

Employing an advanced incompressible flow solver with immersed boundary method and Tree-Local Mesh Refinement (TLMR), the research meticulously investigates the effects of angle of attack (AOA), undulation frequency, and Reynolds number on the formation of complex vortex structures, including leading-edge vortices (LEV), trailing-edge vortices (TEV), and tip vortices (TV). The study reveals that horizontal undulations at an optimal 45° AOA significantly enhance lift, primarily through the modulation of LEVs. Furthermore, variations in undulation frequency and Reynolds number are shown to influence the stability of vortex structures and lift production, respectively. In exploring vertical bending locomotion, the paper highlights

how changes in vertical wave undulation amplitudes and dorsal-ventral bending affect the aerodynamics, demonstrating that certain configurations can significantly augment lift and gliding efficiency. Additionally, the investigation into two-dimensional cross-sectional interactions of snake body segments uncovers the pivotal role of vortex-body interactions in modulating aerodynamic forces, offering insights into the potential for tailoring body posture for improved flight stability and efficiency.

By presenting the complex flow mechanisms and aerodynamic benefits of snake-like undulating and bending motions, this research provides a foundational basis for future explorations into more complex locomotion patterns of gliding animals. Moreover, the findings have implications for the design of bio-inspired robotic systems, potentially leading to the development of more efficient and maneuverable aerial vehicles. The synthesis of numerical simulations with detailed aerodynamic analyses opens new avenues for understanding the physics of natural gliders and translating these insights into innovative technological applications.

This dissertation is dedicated to my parents and grandparents, for their endless love and support of my goals.

Acknowledgements

First, I would present my deepest gratitude to Dr. Haibo Dong for his invaluable guidance, patience, and expert advice throughout my PhD journey. As the advisor of my academic and research life, he has left an indelible mark on both my work and my character. This journey has never been easy and Haibo stood by me through every challenge and choice and he is always there to support. I sincerely thank him and consider him a good mentor as well as a good friend.

I would like to express my sincere gratitude to my committee members, Chloe Dedic, Daniel Quinn, Matthew Reidenbach, and Sarah Sun, for their inspiring guidance, warm encouragement, and constructive comments in my research and my journey to pursue the degree.

I would like to give my special thanks to my collaborator, Jake Socha, from Virginia Polytechnic Institute and State University (Virginia Tech) who provided this great research in flying snake and valuable guidance and comments on my current work.

I would also like to thank my current and previous groupmates, Pan Han, Junshi Wang, Yu Pan, Wei Zhang, John Kelly, Alec Menzer, Jiacheng Guo, Zihao Huang, Menglong Lei, Andrew Davis and all other Flow Simulation Research Group (FSRG) members for their assistance, generosity, and advice throughout my PhD. study and life.

Finally, I would like to express my profound gratitude to my family. To my parents, Xintao Gong and Shumei Chen, I love you and thank you for your unwavering love, support, and sacrifice provided the foundation upon which this journey was built. To Yuning, my love, thank you for supporting me through my hardest time and I will be strong and supportive in our future journey. And to all family and friends, your belief in me has been my greatest source of strength and motivation, which has led and will lead me to more than I can be.

The work presented in this dissertation was supported by the National Science Foundation (NSF) under grant number CBET-2027534 and the Mechanical and Aerospace Engineering Department at the University of Virginia .

Contents

Abstract **iii**

Acknowledgements **vi**

List of Figures **xiii**

List of Tables **xxvii**

1 Introduction **1**

1.1 Motivation and goals 1

1.2 Aerodynamics of the flying snake 3

1.3 Undulation enables and stablizes snake gliding 4

1.4 Intra-body interaction 7

1.5 Current Objects 10

1.6 Outline of the dissertation 13

2 Methodology **17**

2.1 Numerical Method 17

2.2 Solver Validation 19

2.2.1 2D validation 19

2.2.2 3D revolving wing model 19

2.3 Flying snake kinematics reconstruction 21

2.4 Case Setup 28

2.5 Performance Definitions 30

3 Effect of 3D formation and horizontal undulation motion 32

3.1 Aerodynamic performance and wake structures of the steady cases 32

3.1.1 Problem definition 32

3.1.2 Aerodynamic Performances 34

3.1.3 Vortex Structure Near the Body 35

3.1.4 Effect of Body Shapes 37

3.2 Aerodynamic performance and wake structures of the baseline moving case . . 39

3.3 Effects of the Angle of Attack 51

3.4 Effects of undulation frequency 57

3.5 Effect of Reynolds Number 62

3.6 Discussion:The comparison between 2D and 3D models 64

3.7 Conclusions 65

4 Effect of vertical bending undulation 68

4.1 Baseline case 68

4.2 Effect of the vertical wave undulation 72

4.2.1 Aerodynamic performance 73

4.2.2 Surface Pressure and Force Distribution 76

4.2.3 Vortex Dynamics and Flow Analysis 77

4.3 Effect of the dorsal-ventral bending 80

4.3.1 Aerodynamic performance 81

4.3.2 Vortex Dynamics and Flow Analysis 83

4.4 Rolling motion of the flying snake 89

4.4.1 The definition of rolling moment and rolling stability 89

4.4.2 Rolling performance of steady snake 91

Aerodynamic performance 91

Vortex dynamics and related pressure 92

4.4.3 Effect of horizontal undulation in rolling 95

Aerodynamic performance 95

Vortex dynamics and pressure contour 97

4.4.4 Effect of Vertical wave undulation in rolling 101

Rolling performance 101

Rolling stability 102

Vortex Dynamics 104

Pressure contour and span-wise flow 105

4.5 Conclusions 108

5 The intra-body interactions between snake body segments 112

5.1 Problem statement 112

5.2 Solitary foil: aerodynamic performance and wake dynamics 115

5.3 Two tandem foil system: aerodynamic performance and wake dynamics 117

5.3.1 Aerodynamic performance 117

5.3.2 Wake structure 121

5.4 Effects of Reynolds number 123

5.4.1 Aerodynamic performance 123

5.4.2 Vortex dynamics 125

5.5 Effects of the pitching motion 129

5.5.1 Effect of Pitching Amplitude 129

5.5.2 Effect of Pitching frequency 131

5.6 Effects of heaving motion 133

5.6.1 The introduction of heaving motion 133

5.6.2 Effect of heaving amplitude 135

5.6.3 Effect of heaving frequency 139

5.6.4 Expansion to three foils 140

5.7 Conclusions and discussion 143

6 Conclusions **146**

6.1 Summary of Contributions 146

6.1.1 Concluding remarks 146

6.1.2 Contributions and and means of dissemination 151

6.2 Future Work 153

A Kinematics of the undulating flying snake model **155**

A.1 Model 1: Pure horizontal undulating model 155

A.2 Model 2: Vertical wave undulating model 155

A.3 Model 3 & 4: Dorsal-ventral bending undulating model 155

Bibliography **160**

List of Figures

1.1 Examples of shape and posture changes in representative terrestrial gliders during the early portion of the trajectory, in the non-equilibrium descent phase, just after takeoff. Courtesy of National Geographic Television. Adapted and modified from Socha et al. [2]. 2

1.2 (a) The snake applies undulating motion and forms an "S" shape in the aerial gliding[30]. During gliding, their anterior and posterior body create the tandem configuration[8]; (b) Perspective view of the 3D flying snake model with several slice cuts showing different tandem snake airfoil configurations. (c) Side view of the flying snake motion during gliding, indicating the pitching angle change of the posterior body. 9

2.1 Ghost Cell Immersed Boundary Method 18

2.2 (a)The schematic of the computational domain and boundary conditions is depicted. (b) Application of Adaptive Mesh Refinement (AMR) blocks and the setup of the airfoil shape and Angle of Attack (AoA) are presented. (c) Vorticity contour at Reynolds number (Re) of 1000 from the current solver is compared with the simulation work by Krishnan et al. [43]. (d) Time-averaged lift and drag coefficients for Re=500 at various AoA from the current solver and the simulation work are shown. 20

2.3 (a) Experimental setup with wing shape from [61]. (b) Lift production results somparison for Re=120, AOA= 50 ∘. (c1) and (c2) Vorticity for experimental results (top) and the computational results (bottom). 22

2.4 (a) Skeletal structure for the snake model. (b) Definitions of the horizontal (θ) and vertical (ψ) bending angles. (c) Schematic of the skeletal structure that controls the kinematics. $\vec{V}_k$ stands for the global coordinates of discrete body segments. l_k is the length of each segment and s_k represents the accumulative arc length of the snake. 23

2.5 Three-axis-view schematics of the flying snake model under different parameters. Red and blue circles indicate the head and tail tip of the model, respectively. The configurations are: (a) without vertical wave undulation ($\psi_m = 0°$), (b) with a vertical wave undulation amplitude at $\psi_m = 10°$, and (c) dorsal-ventral bending amplitudes at $\psi_{DV} = 5°$ and $-5°$ applied to the configuration in (b). 26

2.6 Definitions of (a) the angle of attack (AOA), the effective angle of attack (eAOA), and the local pitch angle (α_L), and (b) the snake curvature based on the inscribed circles. (c) The κ and α_L curves as a function of body location, in black and blue lines, respectively. The corresponding locations indicated in (b) are also displayed. 28

2.7 (a) Cartesian grid setup and nested topological local mesh refinement (TLMR) blocks with specified boundary conditions. The zoom-in figure highlights the relativity of the blocks. (b) Results from the mesh independence study displaying instantaneous C_L and C_D for a dense grid ($\Delta = 0.035c$, 13.98 million grids), a coarse grid ($\Delta = 0.082c$, 3.02 million grids), and a base grid ($\Delta = 0.041c$, 10.39 million grids) utilized for subsequent analyses. 29

3.1 (a) Body wave shape of flying snake *Chrysopelea paradisi* in ventral view; (b) Top view of the reconstructed 3D model using the math equation; (c) Side view of the model; (d) Cross-sectional geometry applied in the snake body model [2]. 33

3.2 Static cases with different wave shapes corresponding to time at t/T=0.1, 0.2, 0.3 and 0.4. 34

3.3 The instantaneous lift coefficient on the flying snake at non-dimensional time 140 to 160. 35

3.4 (a) Perspective view of wake structure of the baseline case at peak lift distribution. The iso-surfaces are plotted using Q-criterion with $Q = 200$ and flooded by X-vorticity ω_X; (b) Vortex structure near the snake body at peak lift distribution. Z-vorticity ω_Z is applied to visualize the vortices on six slices cutting through the body. ω_X and ω_Z are all normalized by U/c. 37

3.5 (a) Pressure difference (ΔC_P) between the dorsal and ventral surface.(b) Lift coefficient (C_L) distribution along the body. 38

3.6 Time-averaged lift (C_L) and drag (C_D) coefficients of different cases. 39

3.7 (a) and (b) show the perspective view of wake structure of Case 2 and 3 at peak lift timeframe; (c) and (d) show the lift coefficient (C_L) distribution along the body of the two cases, respectively. 40

3.8 Flow information for the baseline case (AOA=35°, Re=500 and $f_\theta = 1$). (a) The instantaneous lift coefficient history. (b) Three-dimensional wake structures of flying snake model in the R-L stroke at (i) t/T=0.00, (ii) t/T=0.17, (iii) t/T=0.23 and (iv) t/T=0.34 respectively, from a perspective view. The iso-surface of the wake structures is visualized by Q-criterion with the value of Q=120. The solid arrow indicates the directions of trailing edge vortex tubes (TEV) and the dashed line arrow indicates the directions of leading-edge vortex tubes (LEV).The head turning motion in this stroke is indicated with blue arrow. 42

3.9 Comparison of instantaneous vortex structure at t/T=0.23 (lift trough) and t/T=0.34 (lift peak), (a) and (b), respectively. (c) and (d) show the 2D spanwise vorticity contour (showing LEV1, LEV2 and TEV1, TEV2) on the anterior snake body at the corresponding timeframes. The slice-cuts are located at z/c= -3, -1, 1, and 3. (e) and (f) show pressure coefficient iso-surface visualized by $C_P = -0.4(blue)$ and $C_P = 0.4(red)$ at the two timeframes, respectively. 46

3.10 Lift distribution over the cycle along the body. 47

3.11 (a) and (b) are the perspective views of the snake with 2D spanwise LEV vortices on slice-cuts at t/T=0.23 (lift trough) and t/T=0.34 (lift peak), respectively; (c) Normalized circulation |Γ| of LEV at the anterior body on different slice-cuts at t/T=0.23 and 0.34. Γ is normalized by UL; (d) and (e) are the top view of the snake showing the lift coefficient surface contour at t/T=0.23 (lift trough) and t/T=0.34 (lift peak), respectively; (f) Local lift coefficient distribution along the body at t/T=0.23 and 0.34. 49

3.12 (a) and (b) show the vortex structure at static position A (same shape as t/T=0) and B (same shape as t/T=0.34) and the LEV and TEV on 2D slice cuts, respectively. (c) and (d) show the lift distribution contour on the contour when they are at peak lift production. The cycle-averaged lift distribution on the model dorsal surface is shown with the baseline case (e1), static position A (e2) and B (e3); (f) shows the corresponding normalized lift distributions along the body (from snout to vent, SVL). 51

3.13 (a) Cycle-averaged lift and drag coefficients at various AOAs; (b) Lift-to-drag ratio and cot(γ) (glide angle function) (c)Instantaneous lift coefficient at AOA 20°, 35°, 45°, and 60°, respectively. 52

3.14 Comparison of flow structures at different AOAs (20°, 45°, and 60°), including vortex structure and 2D spanwise vortices on slice-cut [(a1)–(c1)], lift coefficient surface contour [(a2)–(c2)], and pressure iso-surface visualized by C_P = -0.4 (blue) and C_P = 0.4 (red) [(a3)–(c3); (d) normalized circulation of LEV at anterior snake body on different slice-cuts at t/T = 0.34 (peak lift) with AOA 20°, 35°, 45°, and 60°; (e) normalized circulation of LEV at anterior snake body on different slice-cuts at t/T= 0.23 (trough lift) with AOA 35° and 45°. 54

3.15 (a)-(d) cycle-average C_L contour on the straight body's surface at AOA 20°, 35°, 45°, and 60°, respectively; (e) C_L distribution along the body at t/T=0.34, at four different AOAs, respectively. (f) Normalized cycle-averaged chord C_L distribution along the body at different AOAs. 56

3.16 (a) Cycle-averaged $\overline{C_L}$ and $\overline{C_D}$, at different undulating reduced frequencies. (f=0.889, 1, 1.143, 1.333,1.667 and 2, corresponding with simulation period of T=9/8, 1, 7/8, 3/4, 2/3 and 1/2); (b) Lift-to-drag ratio at different undulating frequencies; (c) Instantaneous force history during a repeating undulating cycle at corresponding frequencies. 58

3.17 Comparison of flow structures at t/T=0.34 with different undulating frequencies f= 0.889 (a1), 1.143 (b1), 1.333 (c1) and 2 (d1). C_L contour on the surface of the snake model body at four frequencies are shown respectively in (a2), (b2), (c2) and (d2). 60

3.18 (a) Normalized circulation of LEV at anterior snake body on different slice-cuts at t/T=0.34 (peak lift) with various frequencies. (b) C_L distribution along the body at t/T=0.34, with five frequencies, respectively. (c)-(f) cycle-average C_L contour on the straight body surface at four frequencies respectively; (c) Normalized cycle-averaged C_L distribution along the body at different frequencies. 61

3.19 (a) Vortex structure and 2D spanwise LEV and TEV vortices on slice-cut at Re=1000. (b) Instantaneous force history curve during a repeating undulating cycle at corresponding Reynolds number (Re=250, 500, and 1000). (c). Normalized circulation of LEV at anterior snake body on different slice-cuts at t/T=0.34 (peak lift) at corresponding Reynolds number. 63

4.1 (a) The instantaneous force coefficients as a function of time in one undulatory cycle. The right-to-left (R–L) motion is shown in grey. 3D wake structures of the flying snake model in the R–L stroke at (b) $t/T = 0.00$, (c) $t/T = 0.21$, (d) $t/T = 0.41$, and (e) $t/T = 0.50$ are presented in perspective view, respectively. The wake structures are visualized by Q-criterion at a value Q = 800 (in transparent white) and at 1200 (in blue). The solid arrow indicates the directions of trailing-edge vortex tubes (TEV), and the dashed line arrow indicates the directions of leading-edge vortex tubes (LEV). 70

4.2 (a) The instantaneous lift coefficient history during one undulatory cycle. The same figure is referenced twice for emphasis. (b) and (c) represent the vortex structure at $t/T = 0.21$ and $t/T = 0.41$, respectively. (1) – (3) corresponds to the XOY plane slice cut at $z/c = -3$, 0, and 3, respectively. The spanwise vorticity contour is presented with the legend listed below. 71

4.3 Cycle-averaged aerodynamic performance of the snake model with different vertical wave undulation amplitudes (ψ_m). (a) Lift, drag, and power coefficients; (b) Lift-to-drag ratio, lift-power ratio, and drag-power ratio. 74

4.4 Instantaneous aerodynamic performance of the snake model with different vertical wave undulation amplitudes ψ_m at 2.5°, 10°, and 20° over one undulatory cycle. (a) Lift coefficients; (b) Drag coefficients; (c) Power coefficient. 76

4.5 (a) Lift distribution along the body at $t/T = 0.41$ at different vertical wave undulation amplitudes ψ_m at 2.5°, 10° and 20°.; (b) – (d) ΔC_P contour on the surface of the snake model body at the different amplitudes, respectively. 77

4.6 Comparison of instantaneous vortex structure at $t/T = 0.41$ with different bending amplitudes ψ_m of 2.5° and 20° for (a), (b) respectively. (c1)–(c3), (d1)–(d3) show the 2D spanwise vorticity contour (showing LEV1, LEV2, and TEV1, TEV2) on the anterior snake body at the corresponding timeframe. The XOY slice-cuts are located at $z/c = -3$, 0, 3 respectively. 79

4.7 Comparison of instantaneous pressure contour at $t/T = 0.41$ with different vertical wave undulation amplitudes ψ_m of 2.5°, 10°, and 20° for (a), (b), and (c) respectively. (1), (2), and (3) represent the position of the XOY slice-cuts' location at $z/c = -3$, 0, 3. 81

4.8 Cycle-averaged aerodynamic performance of the snake model with different dorsal-ventral bending amplitudes (ψ_{DV}). (a) Lift, drag, and power coefficients; (b) Lift-to-drag ratio, lift-power ratio, and drag-power ratio. 82

4.9 Instantaneous aerodynamic performance of the snake model with different dorsal-ventral bending amplitudes ψ_{DV} at 5°, 0° (baseline), and $-5°$ over one undulatory cycle. (a) Lift coefficients; (b) Drag coefficients; (c) Power coefficient. . . 83

4.10 Comparison of instantaneous vortex structure at $t/T = 0.41$ with different bending amplitudes ψ_{DV} of $-5°$ and 5° for (a), (b) respectively. (c1)–(c3), (d1)–(d3) show the 2D spanwise vorticity contour (showing LEV1, LEV2, and TEV1, TEV2) on the anterior snake body at the corresponding timeframe. The XOY slice-cuts are located at $z/c = -3$, 0, 3 respectively. 85

4.11 Comparison of cycle averaged (a) local U velocity pressure contour and (b) pressure contour with different dorsal-ventral bending amplitudes ψ_{DV} of (1) $-5°$, (2) 0°, and (3) 5°. The position of the XOY slice-cuts is at $z/c = 0$. 86

4.12 Comparison of instantaneous pressure contour at $t/T = 0.41$ with different bending amplitudes ψ_{DV} of $-5°$, and 5° for (a) and (b), respectively. (1), (2), and (3) represent the position of the XOY slice-cuts' location at $z/c = -3, 0, +3$. 88

4.13 Schematic of the rolling motion of the gliding snake in (a)top view, (b)side view and (c)front view. 89

4.14 The instantaneous force coefficients for different static shapes (shape at t/T=0.2, 0.4 and 0.7) in one time unit. (a) Lift Coefficient. (b) Drag Coefficient (c) Rolling Moment Coefficient. 92

4.15 The vortex dynamics for (a) peak and (b) trough lift for different static shapes. The shapes are at (1) t/T=0.2, (2) t/T=0.4 and (3) t/T=0.7 93

4.16 The pressure contour at different XOY planes for different static shapes. The shapes are at (a1) ~(a3) t/T=0.2, (b1) ~(b3) t/T=0.4 and (c1) ~(c4) t/T=0.7. The red dashed arrow indicates the local moment. 94

4.17 The instantaneous XOY plane vorticity ω_z and spanwise flow w (in Z direction) contour as in shape at (a)t/T=0.2, (b)t/T=0.4. Two different rolling angles (1)$\beta = 0°$ and (2)$\beta = 5°$is presented. 95

4.18 (a) Instantaneous rolling moment history in one cycle for horizontal undulation motion with two rolling angles. (b1)~(b3) vortex topology at left moment peak, neutral position and right peak for $\beta = 5°$ case. 96

4.19 The pressure contour on different XOY planes for the horizontal undulating model at different time frames (a1) ~(a3) t_1/T = 0.13, (b1) ~(b3) t_2/T = 0.28 and (c1) ~(c3) t_3/T = 0.58. The red dashed arrow indicates the local moment. 98

4.20 The instantaneous Z vorticity ω_z and spanwise flow w (in Z direction) contour n different XOY planes for the horizontal undulating model at different time frames (a1)~(a3) t_1/T=0.13, (b1)~(b3) t_2/T=0.28 and (c1)~(c4) t_3/T=0.58. . . . 99

4.21 The instantaneous force coefficients for different vertical wave undulation amplitude ψ_m. (a) Lift Coefficient. (b) Drag Coefficient (c) Rolling Moment Coefficient. 101

4.22 The instantaneous force coefficients for different rolling angles β at $\psi_m = 10°$. (a) Lift Coefficient. (b) Drag Coefficient (c) Rolling Moment Coefficient. . . . 102

4.23 (a)The average moment for different vertical wave undulation amplitudes ψ_m at small rolling angles. (b) The regression slope κ for different vertical wave undulation amplitude ψ_m. 103

4.24 (a) Instantaneous rolling moment history in one cycle for the undulation motion with vertical wave amplitude $\psi_m = 10°$ with two rolling angles. (b) vortex topology at right moment peak ((1) t_1/T = 0.45), neutral position ((2) t_2/T = 0.73) and left peak ((3) t_3/T = 0.91)for $\beta = 5°$ case. 104

4.25 The pressure contour on different XOY planes for the horizontal undulating model at different time frames (a1)~(a4) t_1/T=0.45, (b1)~(b3) t_2/T=0.73 and (c1)~(c4) t_3/T=0.91. The red dashed arrow indicates the local moment. 106

4.26 The instantaneous Z vorticity ω_z and spanwise flow w (in Z direction) contour n different XOY planes for the horizontal undulating model at different time frames (a1)~(a4) t_1/T=0.45, (b1)~(b3) t_2/T=0.73 and (c1)~(c4) t_3/T=0.91. . . . 107

5.1 Schematic of two-foil system with pitching and heaving motion applied to the anterior body. 114

5.2 Aerodynamic performance for solitary foil 116

5.3 Aerodynamic performance of two tandem flying snake airfoils at Re = 1000. (a1 $\sim$ a3): Time-averaged lift coefficients for upstream foil, downstream foil, and system average; (b1 $\sim$ b3): Lift-to-drag ratio for upstream foil, downstream foil, and system average. 118

5.4 (a1) Vorticity contours and (a2) pressure contours for the configuration Δx = 3.75c, Δy = -0.75c at the snapshot of the maximum lift production on downstream foil. (b1) and (b2) show the same information in the snapshot of the minimum lift production. 120

5.5 (a) Vortex contours and (b) time-averaged stream-wise velocity fields of two tandem flying snake airfoils under different configurations: (1) Δx = 3.75c, Δy = 1.25c (2) Δx = 3.75c, Δy = -0.75c (3) Δx = 3.75c, Δy = -2.00c 122

5.6 Schematic of vortex interaction when the downstream foil is located (a) in the middle of (b) below (c) above the upstream wake. 122

5.7 Aerodynamic performance of two tandem flying snake airfoils at Re = 500. (a1)-(a3): Time-averaged lift coefficients for upstream foil, downstream foil, and system average; (b1 $\sim$ b3): Lift-to-drag ratio for upstream foil, downstream foil, and system average. 124

5.8 Aerodynamic performance of different Reynolds number at configuration Δx = 3.75c, Δy = -0.75c 126

5.9 Time-averaged stream-wise velocity fields of two tandem flying snake airfoils under different Reynolds numbers: (a) Re= 500, (b) Re=750, (c) Re=1000, (d) Re=1500. 126

5.10 Vorticity contour for the configuration Δx = 3.75c, Δy = -0.75c at Re = 500, 750 and 1500 for (a), (b) and (c). (1) and (2) represent the snapshot of the maximum and minimum lift production on foil 2, respectively. 128

5.11 Aerodynamic performance of different pitching amplitudes at configuration Δx = 3.75c, Δy = -0.75c 129

5.12 Evolutions of the vortex structures in one pitching period for the pitching amplitude 5° (a1 $\sim$ a4) and 15° (b1 $\sim$ b4). 130

5.13 Schematic of vortex interaction when the downstream foil is at (a) maximum (b) minimum pitching amplitude. 131

5.14 Aerodynamic performance of different pitching frequencies at configuration Δx = 3.75c, Δy = -0.75c 132

5.15 (a) and (b) show the instantaneous vorticity and pressure contour at T=3, respectively. (c) and (d) show the same information for T=5 133

5.16 Instantaneous force history of the case with heaving motion. The time axis has been normalized with heaving motion period $T = 3.2t^*$. 134

5.17 At (a) $t_1 = 7.10T$, (b) $t_2 = 7.31T$, (c) $t_3 = 7.62T$, and (d) $t_4 = 7.84T$, the evolution of the (1) vortex structures and (2) pressure contour are presented over one complete heaving period. The time frames are selected based on trough and peak lift production instances for foil 1 and foil 2, as indicated in the force history shown in Fig. 5.16. 136

5.18 Cycle-averaged lift coefficient and lift-to-drag ratio at different heaving amplitudes (ΔH_m). 137

5.19 At $\Delta H_m = 0.3c$ and $\Delta H_m = 0.5c$, the vortex structures (a), pressure contour (b), and time-averaged stream-wise velocity (c) are depicted. The vortex and pressure contours are selected at the peak lift time frame. 138

5.20 Cycle-averaged lift coefficient and lift-to-drag ratio at different heaving periods T ($T = \frac{1}{f}$). 139

5.21 At (a)T = 1.0 and (b)T = 6.0, the (1) vortex structures, (2) pressure contour and (3) time-averaged stream-wise velocity are presented. The vortex and pressure contour are chosen at peak lift time frame. 141

5.22 (a)Vortex dynamics of three foils. (b) Time-averaged stream-wise velocity. . . . 141

A.1 Top and perspective view for the pure horizontal undulating model (Model 1: $\theta_m = 93°$ and $\nu_\theta = 1.4$). at (a) t/T=1/8, (b) t/T=2/8, (c) t/T=3/8 and (d) t/T=4/8, respectively. 156

A.2 Top, side perspective view for the vertical wave undulating model (Model 2: $\psi_m = 10°$) at (a) t/T=1/8, (b) t/T=2/8, (c) t/T=3/8 and (d) t/T=4/8, respectively. The horizontal undulation is not changed. 157

A.3 Top, side perspective view for the dorsal-ventral bending model (Model 3: $\psi_{DV} = +5°$) at (a) t/T=1/8, (b) t/T=2/8, (c) t/T=3/8 and (d) t/T=4/8, respectively. The horizontal undulation and the vertical wave undulation are not changed. . . 158

A.4 Top, side perspective view for the dorsal-ventral bending model (Model 4: $\psi_{DV} = -5°$) at (a) t/T=1/8, (b) t/T=2/8, (c) t/T=3/8 and (d) t/T=4/8, respectively.T he horizontal undulation and the vertical wave undulation are not changed. 159

List of Tables

3.1 Aerodynamic performances and curved body portion for different shapes. . . . 39

3.2 Percentage of pressure force and viscous force in lift generation for different Reynolds number. 64

3.3 Cycle average lift coefficient and drag coefficient at 2D, 3D static, and 3D horizontal moving. 64

4.1 Instantaneous lift coefficient at peak and trough value for different vertical wave undulation amplitudes at 2.5°, 10°, and 20°. 75

4.2 Aerodynamic Coefficients and Moment Results for Different Rolling Angles . . 97

5.1 Aerodynamic performance of three steady tandem foils at configuration $L = 3.75c$ and $H = -0.5c$ 142

1 Introduction

1.1 Motivation and goals

Gliding is a type of aerial locomotion allowing significantly enhanced horizontal mobility for some animals in exchange for potential energy or wind energy [1]. More animals have evolved the ability of gliding, including mammals, frogs, lizards, snakes, ants, fish, and squid. In comparison, active flight is relatively uncommon among animals, occurring only in four groups: birds, bats, insects, and extinct pterosaurs [2]. Each gliding animal has evolved unique structures to improve gliding performances, such as the enlarged pectoral and pelvic fins of flying fish [3], the patagial skins of mammals [4], [5], the enlarged feet skin of frogs [6], and the strong muscle and ligament extended membrane wings of Draco lizards [7]. The flying snake is a unique species and a good representative of gliders. As a member of limbless reptiles, it does not create bilateral wings or stretch its skin as a flight membrane. Instead, they rotate and expand their ribs to flatten their body [8], applying undulating motion and passing traveling waves down the body, similar to the postural adjustment mechanism of some ants and lizards [9]–[11].In socha et al.'s early study[12], it has been identified that the glide trajectory of C. paradisi is characterized by an initial ballistic dive, transitioning into a phase where the glide path becomes increasingly horizontal. During the dive, the snake adopts a wide 'S' shape in planview, commencing aerial undulation where high-amplitude traveling waves move posteriorly along the body. This aerial undulation, especially noticeable in the mid-glide phase, features the front part of the body approximately parallel to the ground, while the rear part moves vertically in a cyclic manner.

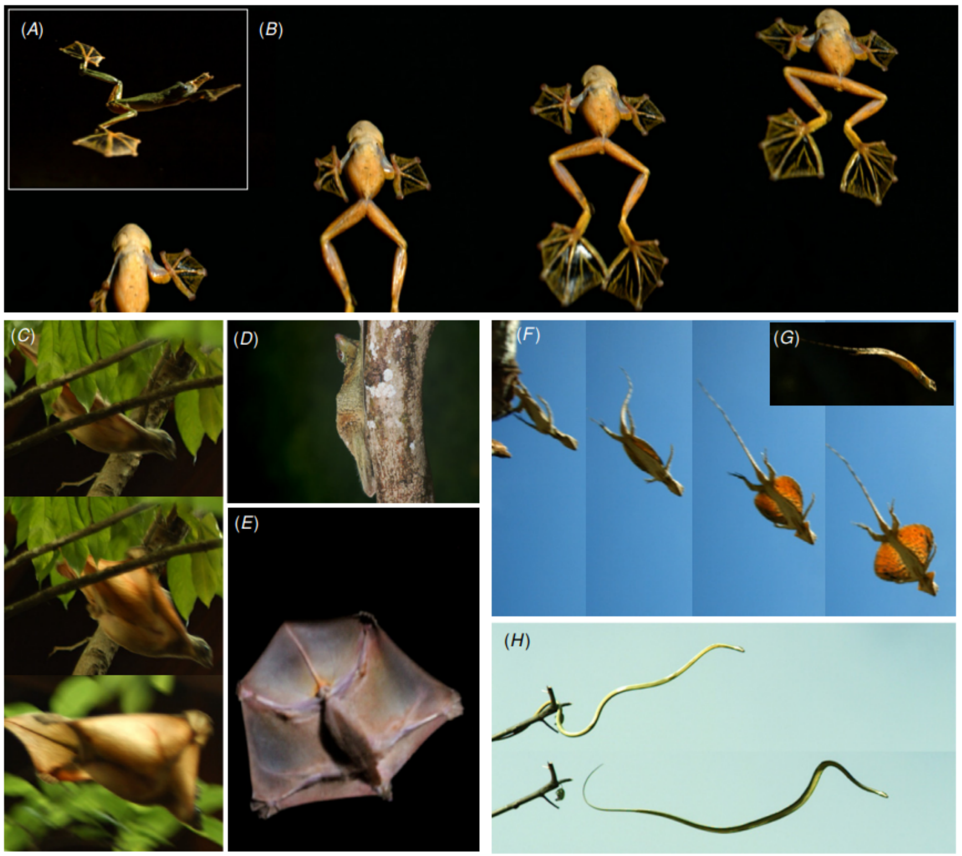

FIGURE 1.1: Examples of shape and posture changes in representative terrestrial gliders during the early portion of the trajectory, in the non-equilibrium descent phase, just after takeoff. Courtesy of National Geographic Television. Adapted and modified from Socha et al. [2].

1.2 Aerodynamics of the flying snake

The aerodynamic performance of various gliding animals has been widely studied, from the dexterous maneuvers of flying squirrels to the expansive glides of birds and insects. By employing a combination of direct observation, high-speed videography, and advanced computational fluid dynamics, we uncover the complex interplay between body morphology, glide dynamics, and aerodynamic forces that govern gliding flight. The grey flying squirrel engage in non-equilibrium gliding, characterized by dynamic velocities, forces, and force coefficients, often generating lift surpassing the requirement for body weight balance[13]. Bats employ unique flight mechanisms such as using a leading edge vortex for enhanced lift during slow speeds and an inverted wing posture during upstrokes to support their weight.They also have adapted wing structure for specialized features and control mechanisms that likely contribute to flight performance, particularly in manoeuvrability[14].Tree frogs employ two primary turning mechanisms during gliding: banked turns and crabbed turns. They exhibit marginal aerodynamic stability, with slight stability in pitch and roll motions but a slight instability in yaw motion [15].

Appealingly, unlike most gliders with mainly static postures, the flying snake exhibits significant body motion, akin to small flapping animals [11]. From a fluid dynamics standpoint, natural flyers experience low-speed and small-size operations in a low Reynolds number (Re) regime where viscous and inertial forces are crucial. The flow is highly unsteady, with lift production and vortex structure manipulation characterizing flight control pressure force [16].Yeaton et al.[17]summarized a new reduced-order gliding model incorporates self-similarity in motion equations, emphasizing how lift and drag alone can shape glide trajectories, without assuming equilibrium.Pitch angle emerges as a critical control parameter in this model, influencing glide angle and speed by altering lift and drag forces. Recent research, including flow visualizations and force measurements, has revealed that insects and hummingbirds utilize unsteady aerodynamic mechanisms for high lift generation required for their flight [18]–[21]. High-lift aerodynamic mechanisms include delayed/absence-of stall indicated by the presence of a leading-edge vortex (LEV), wake-capture, wing-body, and wing-wake interactions [22]–[24].

Eldredge et al. [25] summarized the physics of LEV formation under various canonical wing motions, revealing intricacies in LEV strength influenced by translation speed and other parameters [26]–[29]. This work aims to uncover some mysteries of snake gliding by investigating the link between snake gliding behaviors and its aerodynamic performance, focusing on lateral undulation motions, vertical bending adjustments, and other kinematic aspects.

1.3 Undulation enables and stablizes snake gliding

Additionally, Yeaton et al. [30] conducted experiments on seven snakes over 36 trials and reported that the vertical wave undulation had a high amplitude of up to 30°. They also observed a body angle in the vertical plane termed *dorsoventral bending* that changed throughout each flight trajectory, starting from a positive angle where the head was higher than the rest of the body and ending with a negative angle where the head dived below the tail, leading to potential interactions between the body segments. A study by Miklasz et al. [31] found that when snakes glide, the front and back sections of their body tend to align in a tandem formation. They placed a second snake foil downstream of the first to investigate this phenomenon. The experiments found that the lift increases by 26% for the downstream foil, and the lift-to-drag ratio (L/D) increases by 54% when it is located at a vertical and horizontal distance of -0.9 and 3 chord lengths. In their study, Jafari et al. [32] analyzed the interaction between two bodies for the 2D cross-sectional shape of a flying snake. They found that the performance of a tandem foil system is highly dependent on their relative positions, as the L/D could either decrease by 10% or increase by 12%, and the vortex-body interaction is found to be the main determinant of the aerodynamics in this tandem-body system. This interaction subsides in strength as the staggered downstream body exceeds three chord lengths apart from the upstream body. Gong et al. [33] examined the movement of the posterior foil in response to vertical bending motion. They reported a heaving motion on the posterior body when a vertical wave undulation is applied, resulting in a constant distance change for the trailing foil over a motion cycle. By adjusting the amplitude and frequency of this heaving motion, the downstream foil is able to capture the upstream vortices and take advantage by increasing the lift generation and the L/D. Thus, the tandem-body system can be further improved when the vertical motion is considered.

Stability is a critical aspect of the aerodynamic performance and maneuverability of flying and gliding animals. . For insects, stabilization control is generally performed by their reflex control systems because it demands very fast responses, while maneuver control and steady-state control are performed intentionally [34]–[37]. The hovering flight with stability control has been widely studied and the mechanism has been revealed, including lateral motion, flapping counter-torque and aerodynamic damping, etc[38], [39].Certain bird species adapt to varying aerodynamic demands by altering their wing shapes, inspiring a novel morphing wing design for drones featuring artificial feathers capable of rapid geometric adjustments and achieving roll control through asymmetric adjustment of the wing configuration[40].

Similarly, a wide range of species from flying squirrels to gliding lizards and, notably, the intriguing flying snakes have also evolved unique adaptations that enable them to glide through the air, navigating and adjusting their flight paths with remarkable precision. Flying squirrel

Previous work done by Jafari et al.[41] explored the pitching stability by introducing two-dimensional theoretical models to examine the pitch stability of these serpents. The models incorporate previously recorded force coefficients to depict the aerodynamic forces, with mass variation simulating the undulating motion.

The phenomenon of rolling stability, in particular, plays a pivotal role in their ability to maintain a desired orientation and counteract disturbances that might cause them to veer off course. In the natural world, the ability to glide from one point to another is not merely a feat of distance but a complex interplay of aerodynamic forces and control mechanisms. Gliding animals leverage their body morphology, adjusting their shape and posture in mid-air to manipulate aerodynamic forces to their advantage. The concept of rolling stability is central to this process, as it determines an animal's capacity to sustain a stable glide without succumbing to unwanted rolling motions that could lead to a loss of control.

Understanding the principles of rolling stability in gliding animals is not only fascinating from a biological standpoint but also holds significant implications for the field of bio-inspired design. By studying how these animals achieve and maintain rolling stability during flight, researchers can uncover insights that may inform the development of advanced aerial vehicles and robotics, drawing inspiration from nature's own solutions to the challenges of aerial maneuverability and stability.

1.4 Intra-body interaction

During the process of aerial gliding, the flying snakes *Chrysopelea* exhibit a tendency to adopt a foil-foil interaction configuration as well. As a highly specialized gliding species, flying snakes utilize a distinct form of locomotion that involves bending their bodies to create a large amplitude undulating motion (Figure 1.2 (a)). The curved position creates an S-shape, allowing the anterior and posterior sections of the snake's body to align in a tandem formation. (Figure 1.2 (b)). Miklasz *et al.* first mentioned this formation and studied the interaction between the bodies using two in-line simple cylindrical foils[31].From their research, it was found that the lift on the downstream foil varies depending on the vertical displacement between the snake's anterior and posterior sections. Later on, a higher resolution of snake cross-sectional shape has been reported and investigated both experimentally [42] and numerically [43]. The shape of the cross-section is a semi-triangle with a flat ventral surface and rounded edges at both ends (See Figure 1.2), which was proven to play a significant role in generating lift. Based on this shape, the interactions between the tandem body segments has been further investigated by Jafari *et al.* [32]. Their study covered a wide range horizontal (called as "the gap") and vertical (called as "the staggered") distances. Furthermore, different combination of the orientation (the AOA of the airfoil) between the two foils were studied. Their results revealed that the the maximum value of the average lift-to-drag ratio reached 2.2 and was almost 10% higher compared with the maximum lift-to-drag ratio of a single airfoil. This optimal tandem arrangement modified the separated flow and the wake size, leading to enhanced lift in cases where the wake vortices are formed closer to the models.

Nevertheless, it should be noted that previous research has left certain unanswered inquiries that still require resolution. First of all, the range of relative position between the anterior and posterior bodies has not been fully investigated. In the previous studies done by Miklasz *et al.* and Jafari *et al.*, all the posterior body was placed below the anterior body. However, from the 3D reconstruction of flying snake gliding presented in Figure 1.2 (b), which was originated from the video of real snake gliding from [30], it has been observed that the posterior bodies can be lifted higher than the anterior body. This type of configuration in the vertical direction is prooven to be caused by the vertical bendingt of the undulation motion. According to Yeaton *et al.*'s model [30], the vertical bending consists of a sinusoidal wave (called "vertical wave") and a up-and-down motion of the posterior body (called "dorsal-ventral bending"). It can be observed that there are various arrangements for tandem bodies caused by these motions. We presented the perspective view of one timeframe when the snake is performing aerial gliding in air and chose three vertical planes which is parallel to the incoming flow. In red and light gray planes, the posterior body is placed slightly below the anterior one. However, in the blue plane, there appears three cross-sections simultaneously, while the middle cross-section is above the head cross-section. This shows the aforementioned cases where the posterior body is higher than the anterior body, which has yet to be thoroughly investigated. Secondly, in Figure 1.2 (c) we presented a series of timeframes of the light gray vertical plane using the side view. The anterior body stays still while the posterior body is dynamically moving with the pitching-down motion. This reflects the aforementioned dorsal-ventral bending motion and the underlying flow physics in this phenomenon remain unexplored. Some preliminary results studying the dynamic motion of the posterior body have been presented in the work done by Gong *et al.* [33] with heaving motion, but the pitching motion which affects the angle of attack of the posterior body is under-investigated.

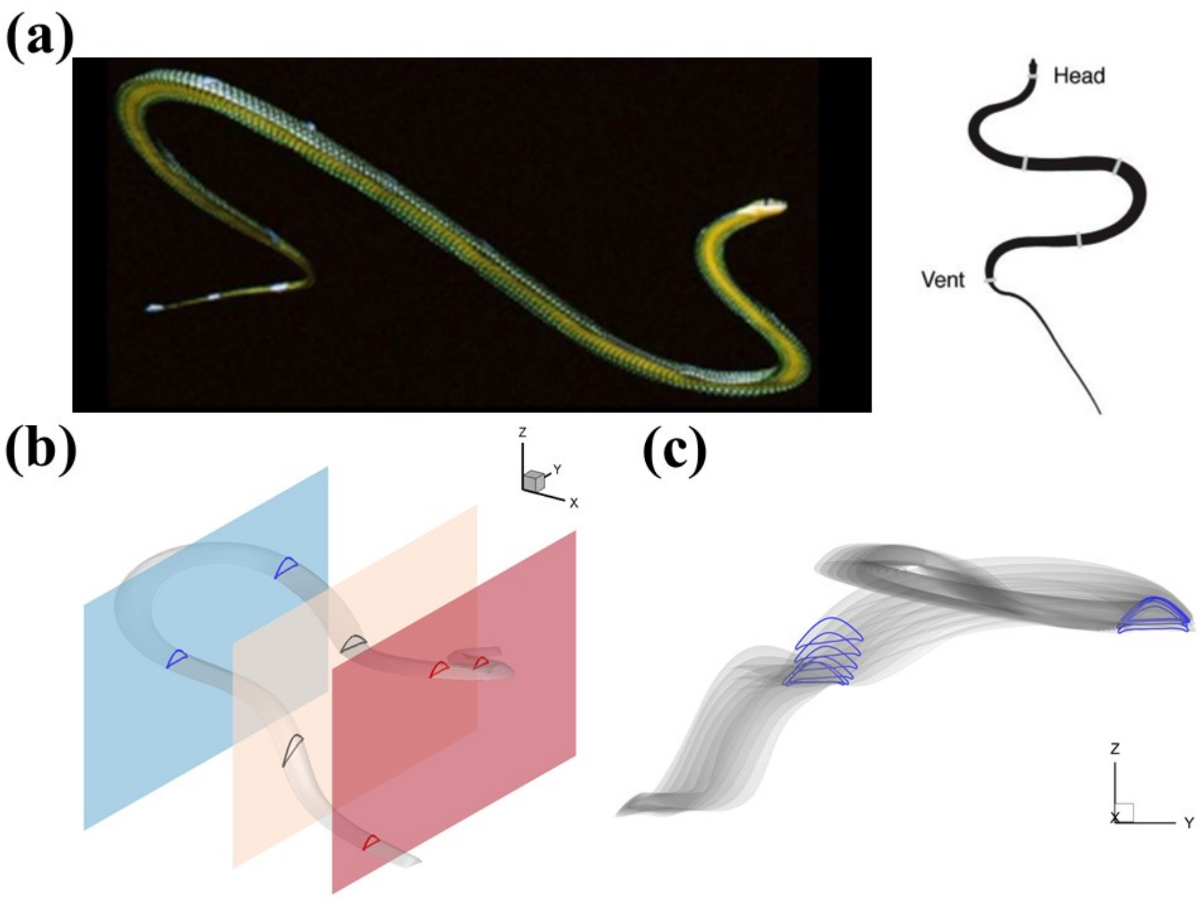

FIGURE 1.2: (a) The snake applies undulating motion and forms an "S" shape in the aerial gliding[30]. During gliding, their anterior and posterior body create the tandem configuration[8]; (b) Perspective view of the 3D flying snake model with several slice cuts showing different tandem snake airfoil configurations. (c) Side view of the flying snake motion during gliding, indicating the pitching angle change of the posterior body.

1.5 Current Objects

The two most distinctive features of flying snake gliding are the flattened body and large-amplitude lateral undulation. Prior experimental and computational studies have shed light on the aerodynamics of flying snakes. Miklasz et al. [31] studied the effect of cross-sectional body shapes, and Holden et al. [42] experimentally analyzed a specific body shape derived from stereo imaging of flying snakes. Their results indicated significant lift capabilities and maximum lift-to-drag ratios at certain angles of attack (AOA). Krishnan et al. [43] further explored these findings through Computational Fluid Dynamics (CFD), revealing critical insights into lift performance and vortex structures.

In addition to these studies, the 3D kinematics of gliding flying snakes in natural settings have been examined. Socha et al. [8] and Yeaton et al. [17] have provided detailed analyses of the snake's gliding trajectories, postural changes, and aerodynamics, including a mathematical model for aerial undulation.

Drawing from these preliminary findings, we formulate our research questions as follows:

Q #1: What is the fundamental lift generation fluid dynamic mechanism in a 3D flying snake model with large-amplitude horizontal undulation? The S-shape posture induced by horizontal waves creates a unique vortex formation essential for lift generation.

Q #2: How does a flying snake improves its aerodynamic performance and gliding efficiency through vertical body bending?

Q #3: Is there potential self-interaction between body segments in a tandem flying snake configuration, and how can it be advantageous aerodynamically? The interaction between snake body segments, especially in tandem configurations, remains a relatively unexplored area that could unveil complex aerodynamic interactions.

Q #4: How does a flying snake control its aerodynamic force moments, aiding maneuverability through undulation motion? Understanding the control mechanisms of flying snakes can provide insights into their exceptional maneuverability and stability during gliding.

This research aims to address these questions through detailed 2D and 3D computational studies, employing high-accuracy numerical simulations to explore the aerodynamics of flying snake gliding under various conditions.To answer the previous mentioned questions, we conducted a few studies to answer the aerodynamic performance and flow fields of these 2D and 3D flying snake will be compared and analyzed in detail to unveil the underlying physical mechanisms.

Object 1: Effect of 3D formation and horizontal undulation motion

This work focuses on the impact of three-dimensional formation and horizontal undulation motion on the aerodynamics of gliding snakes. Using a computational model based on the snake's cross-sectional shape and kinematics, this project aims to:

- Analyze vortex dynamics in static and undulating snake models to compare their aerodynamic performance.

- Identify fundamental flow phenomena and lift enhancement mechanisms in models with horizontal undulation.
- Explore how angle of attack, undulation frequency, and Reynolds number affect the aerodynamic performance.

Object 2: Effect of vertical bending undulation

This work examines the role of vertical bending undulation, including dorsal-ventral bending with various amplitudes and dynamic motions, in flying snake gliding:

- Quantify the impact of vertical wave undulation on the gliding performance, particularly focusing on modified body width.
- Identify flow phenomena related to dorsal-ventral bending and uncover fundamental mechanisms enhancing gliding efficiency.

Object 3: The rolling control in snake gliding

This work examines the rolling motion and the control with the horizontal and vertical undulation and the static stability control in flying snake gliding:

- Identify the rolling moment performance in static flying snake and examine the effect of shape
- Identify the role of horizontal undulation and how it affects the vortex dynamics.

- Identify flow phenomena related to vertical wave undulation and uncover fundamental mechanisms enhancing rolling stability.

Object 4: The intra-body interactions between the body segments

This work also investigates the tandem configuration observed in flying snakes vertical bending motion, where the anterior and posterior bodies are aligned in line. Using 2D numerical models of snake cross-sectional airfoils, the study aims to:

- Analyze the effect of spatial arrangement on tandem snake airfoils' aerodynamics.
- Study vortex-body interactions when heaving and pitching motions are applied to the posterior body, identifying performance enhancement mechanisms.
- Investigate the impact of motion amplitude and frequency on the aerodynamics of the posterior body and its interaction with vortex formation.

1.6 Outline of the dissertation

Chapter 2 is the methodology section, which describes details of the computational fluid dynamics techniques and reconstruction of flying snake modeling. Section 2.1 and 2.2 introduces the immersed boundary reconstruction method as well as the solver validation. Section 2.3 introduces the joint- based kinematics reconstruction and section 2.4 provides case setup for the methodology. And section 2.5 defined some parameters applied in the performance study. The results of Chapter 2 can be found in the following publication:

- Zhang, W., Pan, Y., Gong, Y., Dong, H., & Xi, J. (2021, August). A Versatile IBM-Based AMR Method for Studying Human Snoring. In *Fluids Engineering Division Summer Meeting* (Vol. 85284, p. V001T02A039). American Society of Mechanical Engineers.

Chapter3 presents the simulation result of the horizontal-undulating model. The baseline case is chosen at $AOA = 35°$, Reynolds number $Re = 500$, and $f = 1$. In Section 3.1, we first discuss the effect of shapes in static snake models with the detailed analysis of aerodynamic performance and vortex structure. In section 3.2, we will discuss the baseline moving case's performance and wake structures. Also, the comparison between the static models and the baseline case will be discussed. Finally, three parametric studies of the effects of AOA, the undulation frequency, and the Reynolds number will be presented in Section 3.3 to section 3.5.The results of Chapter 3 formed the basis of the following publications:

- Gong, Y., Wang, J., Zhang, W., Socha, J. J., & Dong, H. (2022). Computational analysis of vortex dynamics and aerodynamic performance in flying-snake-like gliding flight with horizontal undulation. *Physics of Fluids*, 34(12), 121907.

- Gong, Y., Wang, J., Socha, J., & Dong, H. (2022). Aerodynamics and flow characteristics of a flying snake gliding with undulating locomotion. In *AIAA SCITECH 2022 Forum* (p. 1054).

Chapter 4 presents the simulation results for the vertical-undulating model. In Section 4.1, we will examine the aerodynamic performance of the baseline case, along with the vortex structures that lead to the change in performance. In Section 4.2, we will compare different vertical wave undulation amplitudes. In Section 4.3, we will conduct a parametric study to investigate the effects of dorsal-ventral bending with varying amplitudes. In Section 4.4, we will bring the detailed analysis to the rolling moment control and the effect of horizontal shape, horizontal and vertical undulation motion. The results of Chapter 4 formed the basis of the following publications:

- Gong, Y., Huang, Z., & Dong, H. TVertical Bending and Aerodynamic Performance in Flying Snake-Inspired Aerial Undulation. *Bioinspiration & Biomimetics* (Under Review).

Chapter 5 investigates the tandem configuration observed in flying snakes vertical bending motion.Section 5.2 presents the aerodynamic performance of a solitary flying snake airfoil. The results validated our solver, and we confirmed that the choice of AOA=35°as the baseline case corresponds to the highest lift production. In section 5.3, the aerodynamic performance and wake structures of a two-foil system are studied with the configuration range of $3c \leq \Delta x \leq 4c$ and $-2c \leq \Delta y \leq 2c$. In section 5.4, the effect of Reynolds number is investigated. The aerodynamic performance is provided with the same range at Re=500. The vortex wake and interaction is presented and discussed in detail for a chosen configuration with different Reynolds number. In section 5.5, the effects of pitching motion with different pitching amplitudes and frequencies are discussed in section 5.4.In section 5.6, the aerodynamic performance and flow structure is studied with the effect of heaving amplitude and frequencies. The results of Chapter 5 formed the basis of the following publications:

- Gong, Y., & Dong, H. (2023). Computation study about the interaction between the tandem flying snake airfoils with dynamic motion. In *AIAA SCITECH 2023 Forum* (p. 2460).

- Gong, Y., He, A. & Dong, H. Numerical analysis of the interaction between two tandem flying snake foils with pitching motion. Target: *Biomemetics MDPI*. (Under process)

Chapter 6 summarizes the conclusions of the current computational studies and points toward future work.

2 Methodology

2.1 Numerical Method

In this study, the 2D unsteady viscous incompressible Navier-Stokes equations, written in index form as

$$\frac{\partial u_i}{\partial x_i} = 0; \quad \frac{\partial u_i}{\partial t} + \frac{\partial u_i u_j}{\partial x_j} = -\frac{\partial p}{\partial x_i} + \frac{1}{Re}\frac{\partial u_i^2}{\partial x_i \partial x_j}, \tag{2.1}$$

govern the flow. In the equations, p is pressure, u_i denotes Cartesian velocity components, and Re is the Reynolds number, given by the equation $Re = \frac{U_\infty c}{\nu}$. An in-house immersed boundary method-based finite difference flow solver is employed to solve the equations, which are discretized spatially using a cell-centered collocated arrangement of the primitive variables and integrated in time using a fractional step method, which is second-order accurate in time. The convection and diffusion terms are solved using an Adams-Bashforth scheme and implicit Crank-Nicolson scheme, respectively. The immersed boundary method utilizes a ghost-cell method to employ a complex interface boundary over a stationary Cartesian grid. A schematic is shown in Fig. 2.1. The process begins with identifying each cell on the cartesian grid. Fluid cells are cells with the center outside the body, and solid cells are made of cells completely

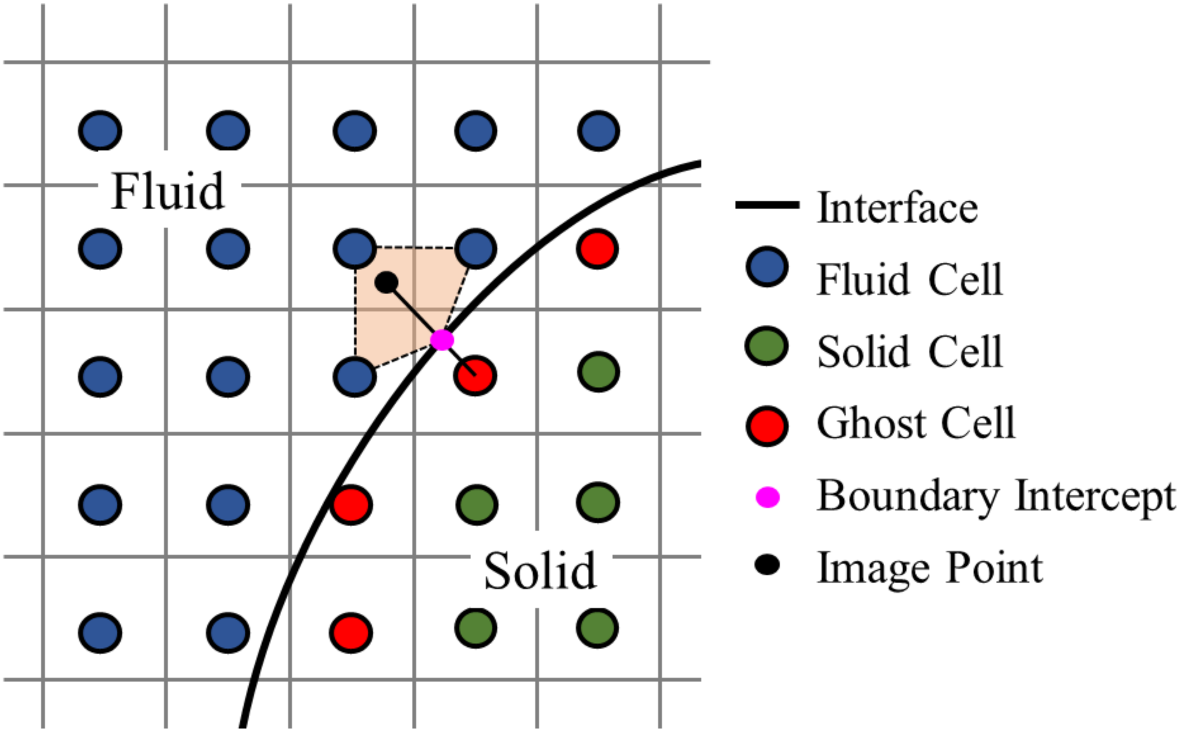

FIGURE 2.1: Schematic of Ghost Cell Immersed Boundary Method.

inside the body and not adjacent to the boundary. Ghost cells have a cell center inside the body and have neighboring cells outside the body. In order to preserve the boundary condition and maintain second order accuracy, a line is extended from the ghost cell through the boundary normal to the interface. An image point is defined as equidistant to the boundary intercept as the ghost cell center. An interpolation process is then used to calculate the values at the image point from the surrounding fluid cells, which is then used to obtain the value on the ghost cell. This method allows for simulation of complex moving boundaries on a stationary grid, without the computationally expensive re-meshing required by commercially available CFD solvers. It has been successfully employed in previous biological swimming studies [44]–[49], insect and bird flying[50]–[53], bio-inspired canonical problems [54]–[57], and has been previously validated extensively [46], [55], [58]. More details can be found in [59], [60].

2.2 Solver Validation

2.2.1 2D validation

The force and flow validation are critical for evaluating the performance of the snake gliding. Here we provided a validation in Figure 2.2 to compare with the previous studies done by Holden et al. [42] with 2D flying snake cross-section.

We applied the same geometry of the cross-section shape as their 2D and our 3D study and it was also scaled such that the chord length $c = 1$. For the mesh setup, we applied the same mesh size ($\Delta x = \Delta y = 0.004$) as that used in [43]. The uniform flow velocity was set to be $U_\infty = 1$ and the flow comes from $+x$ direction as shown in Figure 2.2(a). More details about the chord length and AOA are presented in Figure 2.2(b). For this validation study, we first picked the case at $Re = 1000, AOA = 35°$ and presented the spanwise vorticity contour of flow past the foil in Figure 2.2(c). The contours are in good agreement with the Figure 8(c) in [43].

We also performed the simulation at Reynolds number 500 for 50 time units until it reached steadiness. The time-averaged lift and drag coefficients with AOA change (within the range of 0° to 45° at the increment of 5°) are presented in Figure 2.2(d). The results showed good agreement between the current solver and previous work.

2.2.2 3D revolving wing model

To further validate the computational solver for snake study, body-body interacting flows, the experimental work of Dewey et al. [61] is reproduced using the solver to verify its accuracy. In this experiment, the aerodynamic efficiency observed in insects is partly ascribed to the creation

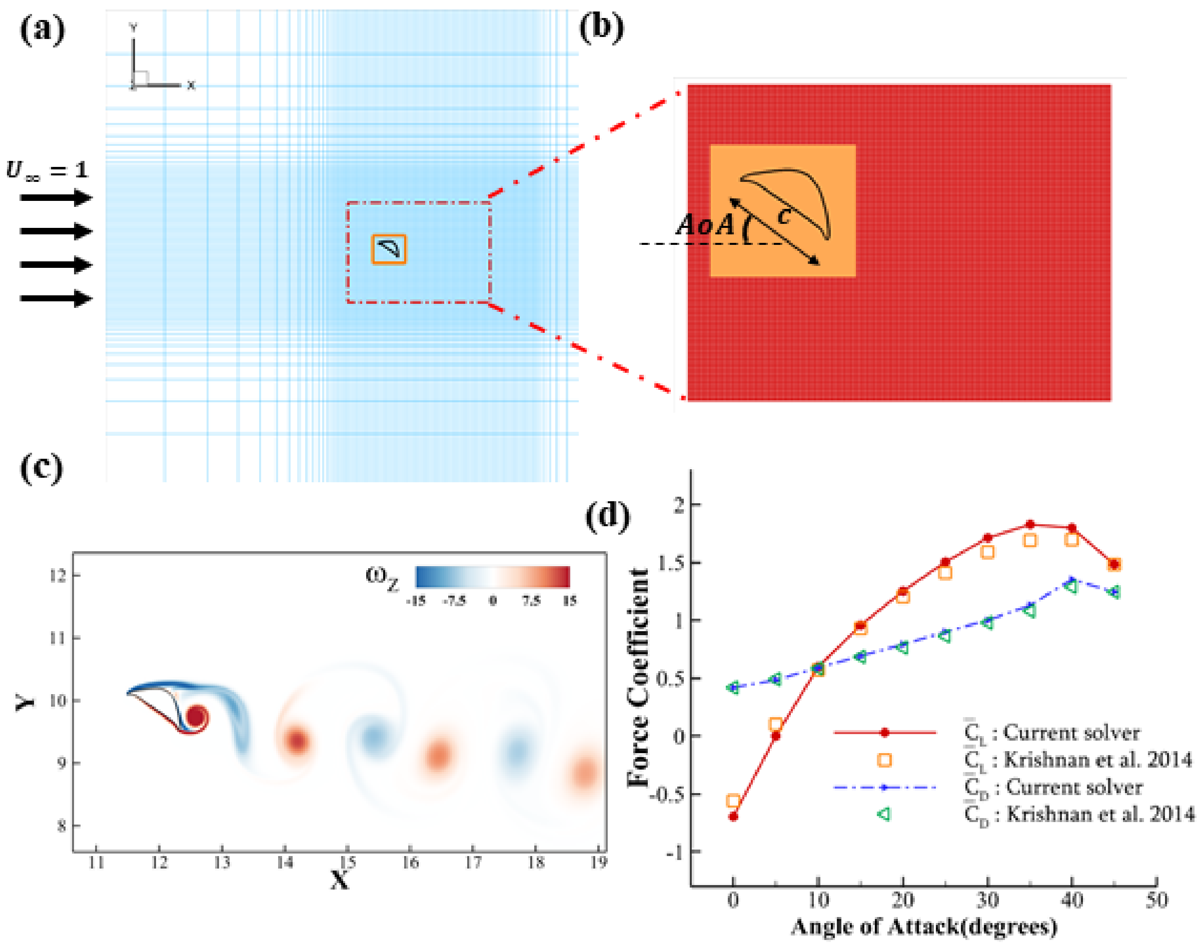

FIGURE 2.2: (a)The schematic of the computational domain and boundary conditions is depicted. (b) Application of Adaptive Mesh Refinement (AMR) blocks and the setup of the airfoil shape and Angle of Attack (AoA) are presented. (c) Vorticity contour at Reynolds number (Re) of 1000 from the current solver is compared with the simulation work by Krishnan et al. [43]. (d) Time-averaged lift and drag coefficients for Re=500 at various AoA from the current solver and the simulation work are shown.

and sustenance of a stable vorticity zone, known as the leading-edge vortex (LEV), which is critical for flight. A theory positing the stability of LEV involves a spiraling axial flow within the vortex core, which dissipates energy to the tip vortex, thus establishing a leading-edge spiral vortex akin to the aerodynamic patterns observed in delta wing aircraft. Notably, this spiraling flow is prominent in the flapping wings at higher Reynolds numbers (Re), approximately 5000, but such structures are not discernibly replicated at lower Re, specifically around 100.. Digital particle image velocimetry (DPIV) is also used to produce a vortex field and cycle-average velocity.

The results from the experimental data along with the computational comparison from our solver are shown in Fig. 2.3. In Figure 2.3(b), we present the revolving wing lift production from the start and the lift coefficient for experimental data is given by the points, along with the computational data shown by the lines. From this, we see that almost every data point is within the experimental error. This confirms the validity of our solver in calculating the hydrodynamic performance in multi-foil interacting systems. Figure 2.3 (c1) and (c2) contain the vorticity from the experimental data and the computational data. From the figure, both the leading-edge vortex structure of the experimental and computational data match very closely, further validating our computational solver for wake analysis in 3D moving body interacting flows.

2.3 Flying snake kinematics reconstruction

The snake model herein adapts a joint-based hierarchical skeletal structure that is bound to a polygonal-mesh skin using the 3D modeling software *Autodesk Maya*® (Autodesk Inc., Mill

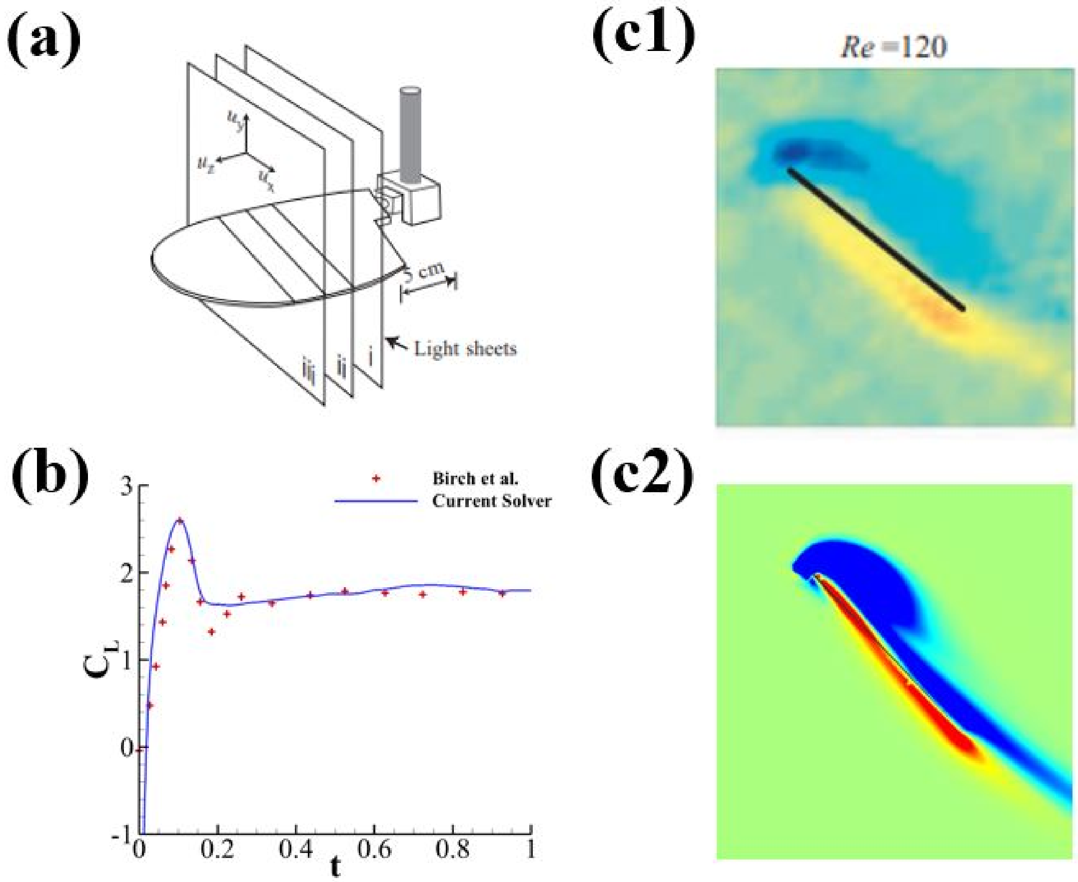

FIGURE 2.3: (a) Experimental setup with wing shape from [61]. (b) Lift production results somparison for Re=120, AOA= 50 ∘. (c1) and (c2) Vorticity for experimental results (top) and the computational results (bottom).

Valley, California, U.S.) [62], as shown in Figure 2.4(a). The undulatory motion is decomposed into the joint rotations and is then applied to the joints along the snake body to realize the gliding kinematic. This technique has been successfully applied in the previous work [50], [63]. The gliding snake kinematic can be decomposed into the horizontal undulation and the vertical undulation as reported by Yeaton et al. [30]. The horizontal decomposition is realized through applying a horizontal bending angle (θ) to each of the body segments, which has been evaluated in our previous study, and the vertical undulation is realized through the vertical bending angle (ψ). The bending angle definitions are illustrated in Figure 2.4(b).

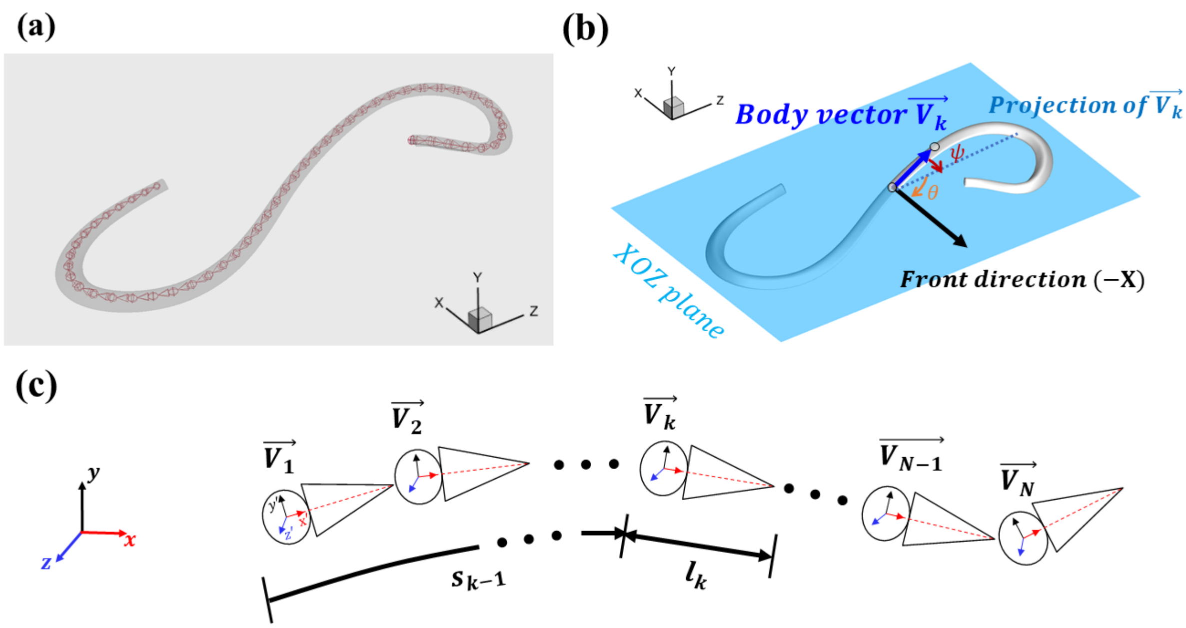

FIGURE 2.4: (a) Skeletal structure for the snake model. (b) Definitions of the horizontal (θ) and vertical (ψ) bending angles. (c) Schematic of the skeletal structure that controls the kinematics. $\vec{V}_k$ stands for the global coordinates of discrete body segments. l_k is the length of each segment and s_k represents the accumulative arc length of the snake.

Figure 2.4(c) shows the schematics for the skeletal structure that controls the flying snake gliding kinematics. Previously, Jafari et al. proposed a n-chain model to control the snake motion during gliding[64].The snake was modeled as an articulated chain of airfoils connected with revolute joints. This was implemented either by directly prescribing the joint angles as periodic functions of time (kinematic undulation), or by assuming periodic torques acting at the joints (torque undulation). Similary in our model reconstruction, the rotation of each joint is dependent on the local body arc length s_k, and it is approached by the summation of finite numbers of distances between joints. Therefore, the global coordinate for each joint's location can be expressed as:

$$\vec{S}_k(x_k, y_k, z_k) = \sum_{j=1}^{k} l_j \vec{V}_j \tag{2.2}$$

where $\vec{S}_k$ represents the coordinate of the k-th joint ($k = 1, 2, \ldots, N$, where N is the total joint number), l_j represents the segment length between two neighboring joints, and $\vec{V}_j$ is the unit vector describing joint orientation. The multiplication of $l_j \vec{V}_j$ represents the displacement added by the j-th joint and the summation adds up to be the position of the current joint. Thus, we can calculate the arc length s_k (until the k-th joint) of the snake body using the following summation:

$$s_k = \sum_{j=1}^{k} |l_j \vec{V}_j| \tag{2.3}$$

The joint direction $\vec{V}_k$ in equation (1) is described with the following unit vector:

$$\vec{V}_k = \cos(\psi_k)\cos(\theta_k), -\sin(\psi_k), \cos(\psi_k)\sin(\theta_k)^T \tag{2.4}$$

where θ_k and ψ_k represent the horizontal and vertical bending angles of the k-th joint at the snake body. These bending angles by definitions are functions of time for each joint along the body, and they are calculated as:

$$\theta_k(s_k,t) = \theta_m \sin\left[\frac{\pi}{2}\cos\left(\frac{2\pi\nu_\theta}{L}s_k - 2\pi f_\theta \frac{t}{T} + \phi_\theta\right)\right] \tag{2.5}$$

$$\psi_k(s_k,t) = \psi_m \cos\left(\frac{2\pi\nu_\psi}{L}s_k - 2\pi f_\psi \frac{t}{T} + \phi_\psi\right) + \psi_{DV}\frac{s_k}{L} \tag{2.6}$$

Equations 2.5 and 2.6 describe the change in horizontal and vertical undulation angles on the k-th joint at a given time t, over a motion cycle period of T. θ_m and ψ_m represent the maximum horizontal and vertical bending angle, respectively. ν_θ, f_θ, and ϕ_θ are the wave number, undulatory frequency, and the phase shift that are related to the horizontal motion, and ν_ψ, f_ψ and ϕ_ψ are those related to the vertical motion. s_k is the accumulative body arc length. In the previous study by Gong et al., when only considering the horizontal undulation, the optimal aerodynamic performance was found with $\theta_m = 93°$ and $\nu_\theta = 1.4$. These parameters were kept constant in the current study to analyze the impact of vertical undulations. The relation between the horizontal and vertical motion with regard to the wave number and undulatory frequency is described as $f_\psi = 2f_\theta$, and $\nu_\psi = 2\nu_\theta$, according to Ref.[30]. Furthermore, the effect of the full body pitching motion described by Yeaton et al. is also studied herein. This is realized through including an additional term, ψ_{DV}, to Equation 2.6, which allowed for a vertical offset along the length of the body, L.

Figure 2.5 illustrates the three-axis-view schematics to describe the setup for the flying snake

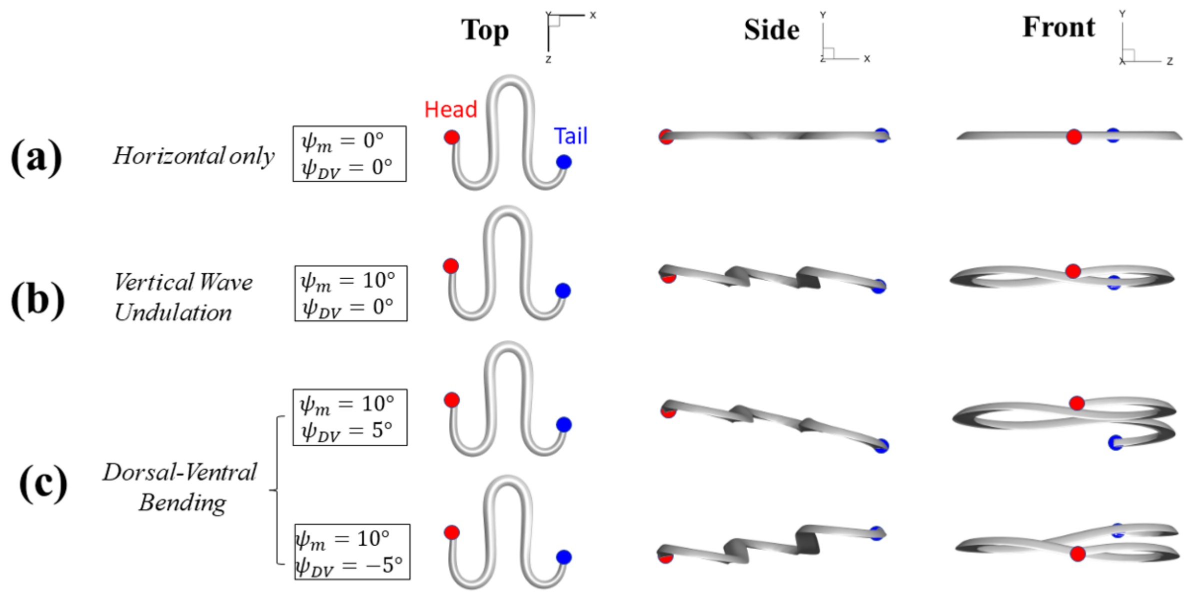

FIGURE 2.5: Three-axis-view schematics of the flying snake model under different parameters. Red and blue circles indicate the head and tail tip of the model, respectively. The configurations are: (a) without vertical wave undulation ($\psi_m = 0°$), (b) with a vertical wave undulation amplitude at $\psi_m = 10°$, and (c) dorsal-ventral bending amplitudes at $\psi_{DV} = 5°$ and $-5°$ applied to the configuration in (b).

model with different vertical bending patterns. The head and tail of the model are marked with red and blue dots, respectively. The horizontal undulation model is presented in Figure 2.5 (a) as a reference. The baseline case for studying the effect of vertical wave undulation is set with $\psi_m = 10^\circ$ and $\psi_{DV} = 0^\circ$, depicted in Figure 2.5 (b). The top view maintains an S-shaped posture similar to the pure horizontal undulation configuration, but the front view exhibits an "8" shape on the snake body, with the side view showing a neutral model position without dorsal-ventral bending. Figure 2.5 (c) demonstrates configurations considering dorsal-ventral bending with maximum amplitudes of $\psi_{DV} = 5^\circ$ and -5°. While the top views are akin to previous configurations, the side views display the tail-down/up motion corresponding to positive and negative ψ_{DV} values, respectively.

The uniform incoming flow acting on the twisted snake body creates different angles of attack at various locations, introduced by the vertical wave undulation. The study adapts the effective angle of attack (eAOA), calculated as the difference between the angle of attack (AOA) and the local pitch angle (α_L), with the chord-line direction defined as the snake body width. The local pitch angle (α_L) is the angle between the chord-line and the horizontal plane, as shown in Figure 2.6(a).

To link the local pitch angle (α_L) with horizontal undulation, curvature (κ) is used to describe the horizontal shape of the snake, as depicted in Figure 2.6(b). The curvature at a point on the midline curve, defined as the reciprocal of the radius (r) of the inscribed circle, is expressed as $\kappa = \frac{1}{r}$. The relationship between κ and α_L is illustrated in Figure 2.6 (c), with κ and α_L shown in black and blue lines, respectively. A dashed line at $\kappa = 0.1$ highlights the region where curvature is below 0.1 in grey, indicating that body parts with lower curvatures have higher local pitch angles, with straighter body segments exhibiting higher α_L and curved sections showing lower α_L.

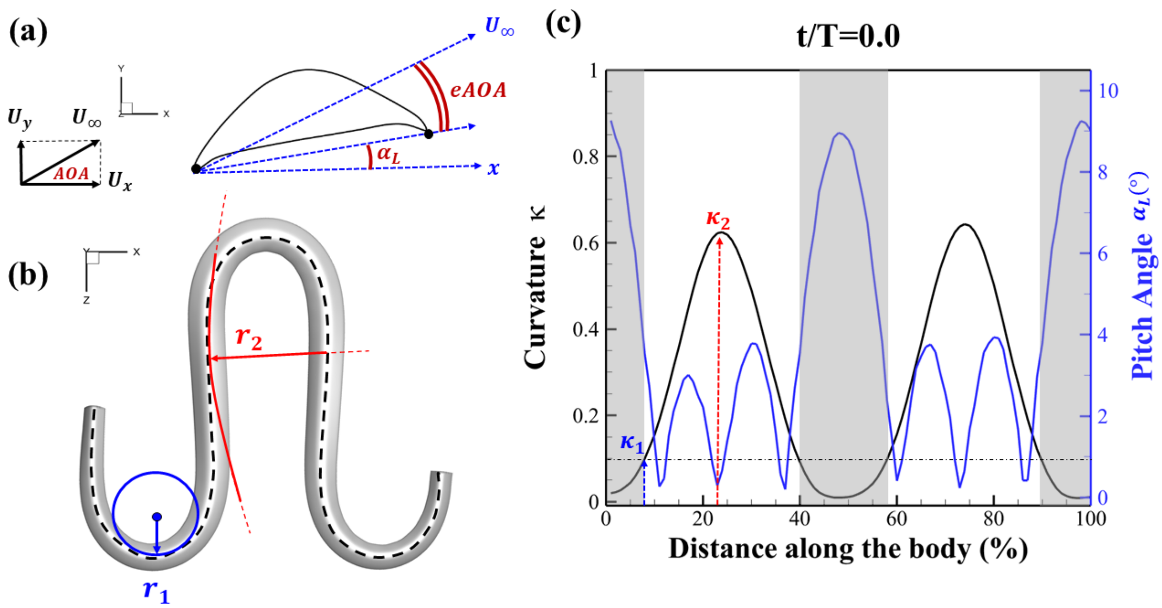

FIGURE 2.6: Definitions of (a) the angle of attack (AOA), the effective angle of attack (eAOA), and the local pitch angle (α_L), and (b) the snake curvature based on the inscribed circles. (c) The κ and α_L curves as a function of body location, in black and blue lines, respectively. The corresponding locations indicated in (b) are also displayed.

2.4 Case Setup

The schematic of the computational domain is depicted in Figure 2.7 (a). A domain size of $80c \times 100c \times 100c$ with an x-y-z coordinate system is established, featuring a minimum grid spacing at $\Delta = 0.164c$, as shown in the dense dark blue region in Figure 2.7 (a). Employing a tree-topological local mesh refinement (TLMR) technique allows for further refinement of the mesh around the flying snake model with efficient computational resource utilization [65]. As detailed in the zoomed-in schematic of Figure 2.7 (a), a larger parent mesh refinement block (light blue) encompasses the wake region to enable a semi-dense grid spacing at $\Delta = 0.082c$, and a smaller block (orange) surrounds the snake model to capture the near-body vortices with a dense grid spacing at $\Delta_{\min} = 0.041c$, resulting in a total grid count of 10.4 million. This mesh refinement approach has been previously applied in bio-inspired flight studies [66]. An incoming flow velocity is imposed in the x- and y-direction at an angle of attack (AOA) of 35°, with homogeneous Neumann boundary conditions applied at the remaining boundaries.

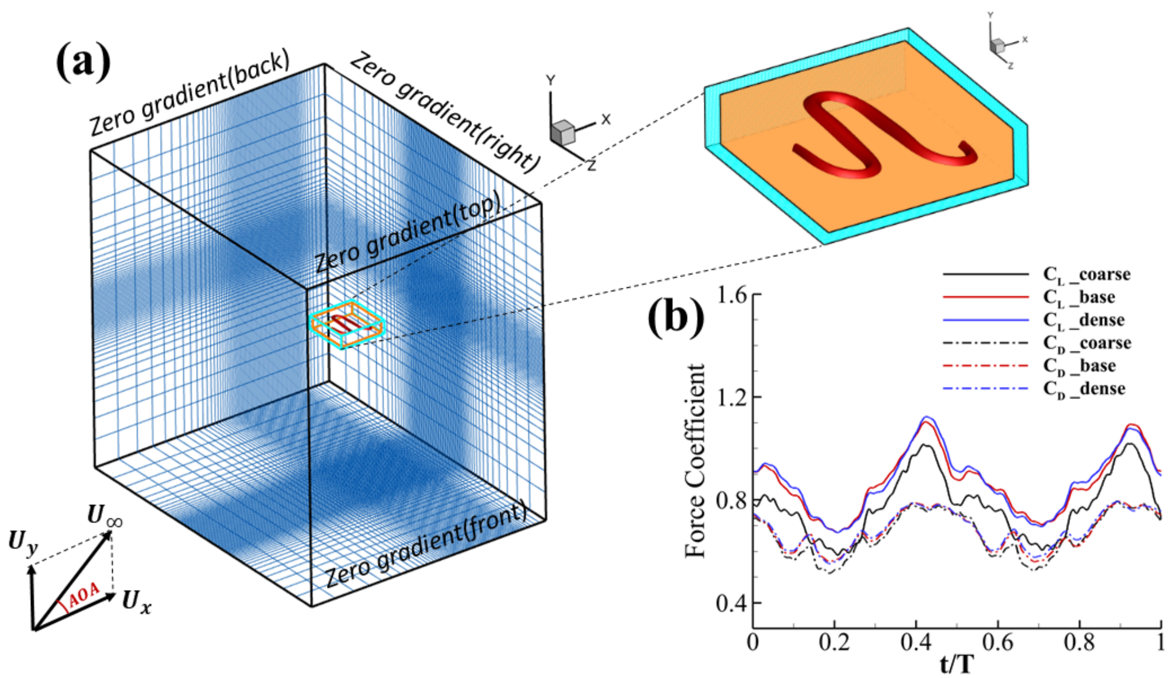

FIGURE 2.7: (a) Cartesian grid setup and nested topological local mesh refinement (TLMR) blocks with specified boundary conditions. The zoom-in figure highlights the relativity of the blocks. (b) Results from the mesh independence study displaying instantaneous C_L and C_D for a dense grid ($\Delta = 0.035c$, 13.98 million grids), a coarse grid ($\Delta = 0.082c$, 3.02 million grids), and a base grid ($\Delta = 0.041c$, 10.39 million grids) utilized for subsequent analyses.

A grid-independent study was conducted utilizing three grid sizes: $\Delta = 0.082c$ (coarse), $\Delta = 0.041c$ (base), and $\Delta = 0.035c$ (dense). The lift and drag coefficients, C_L and C_D, defined as the lift and drag forces normalized by $\frac{1}{2}\rho U_\infty^2 cL$, are employed to assess the mesh sizes. The force coefficients over a motion cycle are illustrated in Figure 2.7 (b), where the solid line represents

C_L and the dashed line denotes C_D. The peak difference in C_L and C_D between the base grid and the dense grid are 1.8% and 0.05%, respectively, while the cycle-averaged lift and drag coefficient differences between the base and dense mesh are both under 0.1%. Consequently, it is concluded that the base mesh suffices for the computations, and the analyses herein are executed using the base mesh.

2.5 Performance Definitions

To solve for the aerodynamic forces, lift force F_L and drag force F_D, the solver directly integrates the projected surface pressure and shear force over each body. Lift force is defined as the sum of force parallel to the incoming flow direction and the drag force is perpendicular to the flow direction. The resulting force coefficients C_L, C_D, are computed by

$$C_L = \frac{F_L}{0.5\rho U_\infty^2 cL}, C_D = \frac{F_D}{0.5\rho U_\infty^2 cL}. \tag{2.7}$$

The total power is defined as the rate of the output work done by the flying snake to complete its motion. It is given mathematically by

$$P_u = \oint (-pn_i + \tau_{ij}n_j)\Delta u_i dS, \tag{2.8}$$

where n is the unit normal to the surface, and Δu_i is the velocity of the element dS relative to its surrounding fluid in the i-th direction. The coefficient of power can then be calculated as

$$C_{pw} = \frac{P_u}{0.5\rho U_\infty^3 c}. \tag{2.9}$$

3 Effect of 3D formation and horizontal undulation motion

3.1 Aerodynamic performance and wake structures of the steady cases

While aerial gliding, its body applies undulating motion and passes traveling waves down the body(Figure 3.1 (a)). The changing body shape will provide impact on the snake performance. To start with, we studied the flying-snake 3D model with several different static horizontal wave shape profiles. Initially, the aerodynamics performance, surface pressure results, and three-dimensional vortex structures of the baseline model are analyzed and compared. Then we studied the effects of the wave shapes by choosing several different timeframes' static snake postures.

3.1.1 Problem definition

Figure 3.1 (b) shows one of the models generated with a set of specific parameters: $\theta_{\max} = 93^{\circ}$, $\nu_{\theta} = 1.4$, $f = 1$, $t/T = 0$ $(T = 1/f)$. The maximum horizontal bending angle θ_m and spatial period number ν_θ is a set of parameters observed in real flying snake gliding experiments. The curvature κ of the snake is also defined with the osculating circle of the midline curve. This concept is used for the discussion of different snake shapes.

The equation and parameters describing vertical bending are not introduced in this study so that the effect of the pure horizontal body shape can be studied. Figure 3.1(c) shows no vertical (in Y direction) deformation. This steady shape is set up as starting case (Case 0) in our simulation.

In Figure 3.1 (d), the cross-section shape of the flying snake body was shown. It was originated from high-speed video and also applied in previous experiments and numerical study [42]. Its chord length is defined as C and the body length is also defined as $L = 35c$. This body-chord ratio is measured from the video [2].

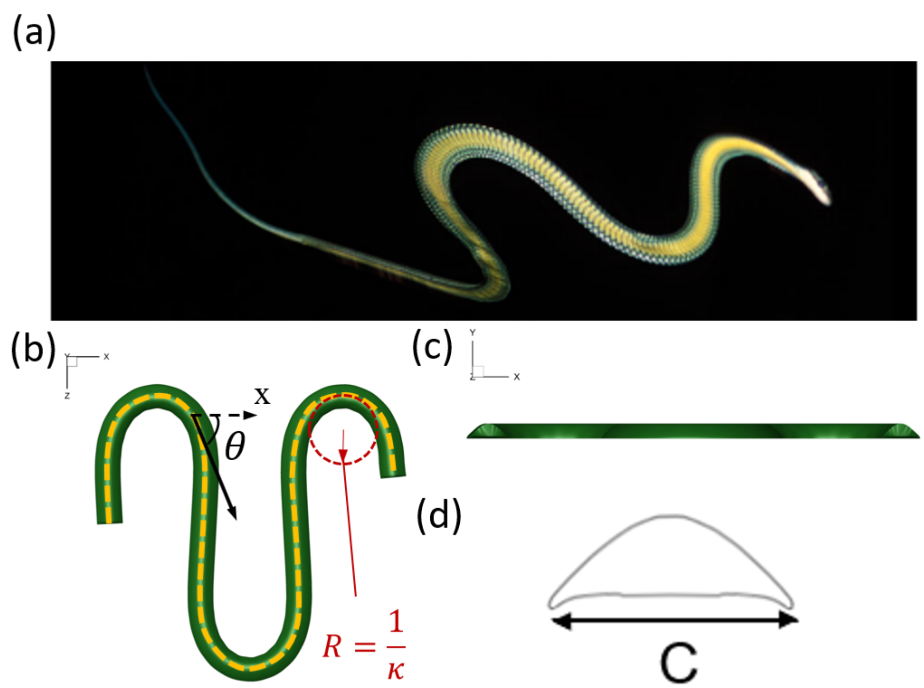

FIGURE 3.1: (a) Body wave shape of flying snake *Chrysopelea paradisi* in ventral view; (b) Top view of the reconstructed 3D model using the math equation; (c) Side view of the model; (d) Cross-sectional geometry applied in the snake body model [2].

To further study the effect of snake wave shape, a phase shift is introduced through changing different time t. Given the symmetry of the wave function, only the first half of the undulation motion is adopted to create different static shapes models with $t/T = 0.1, 0.2, 0.3, 0.4$. The corresponding phase change will be $-0.2\pi, -0.4\pi, -0.6\pi, -0.8\pi$ as shown in Figure 3.2 (a)-(d) (As our Case 1 to 4).

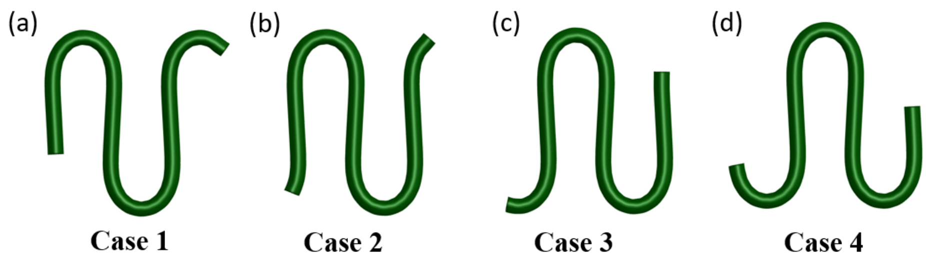

FIGURE 3.2: Static cases with different wave shapes corresponding to time at t/T=0.1, 0.2, 0.3 and 0.4.

3.1.2 Aerodynamic Performances

Figure 3.3 shows the instantaneous lift and drag coefficient for the starting case 0. To reach a steady state, the force history is presented between the non-dimensional time $t = 140 - 160$. Normalized time t^* is calculated with freestream velocity U and chord length c ($t^* = tU/c$). Time-averaged force coefficient is also calculated within this timeframe to eliminate the influence of the initial condition. From the time history, we can observe the oscillation caused by the vortex shedding and regeneration process on the surface, which will be discussed in a later section.

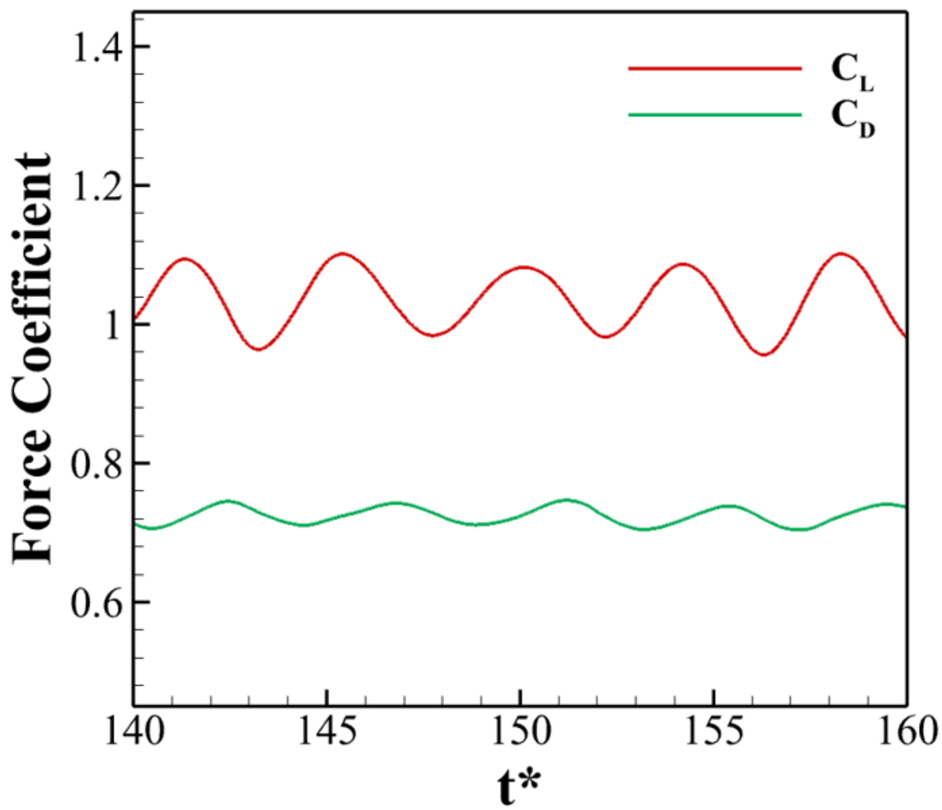

FIGURE 3.3: The instantaneous lift coefficient on the flying snake at non-dimensional time 140 to 160.

3.1.3 Vortex Structure Near the Body

Figure 3.4 illustrates the vortex structure around and at the wake of the computational model in gliding. The snapshot of the vortex is taken at a local lift peak. The iso-surface structures are visualized using the Q-criterion with a value of 200. The main feature on the body that can be identified is the edge vortices (EV) generated on the straight part of the body. Topologically speaking, the straight tube hints at 2D leading-edge vortices (LEV) expanding it spanwise (the third dimension in space). Similarly, trailing-edge vortex tubes (TEV) can also be observed below the LEV. Interaction between each plane may merge into different structures such as hairpin vortices. This process and structure were investigated and reported in the three-dimensional flow around a flat plate by Taira et al..[67], especially with larger aspect ratios.The tip vortex (TV) is also a prominent vortex structure observed at the head. The blue contoured, counter-clockwise rotating TV shares a similar vortex loop structure at the head (tip) as the simulation done by Taira et al.[67] with low-aspect-ratio wings or Li et al.[68] with revolving wings.

One unique vortex structure observed in the current snake model is the side (edge) vortices (SV). SVs are generated on the turning curved part of the snake body. They share some similar topology shape as the TV since they are all formed on the edge of the model. However, SV is more complicated than the TV. Due to the turning of the body, this particular section can be treated as a wing with span-wise flow only. The flow passes along both leading and trailing edges with a velocity perpendicular to the cross-section. The spinning vortex loop pairs with a curved shape comes from the vortex loops generated on both sides of the body and merged together. EV, TV, and SV are formed on different parts of the snake model, interacting with each other all the time, contributing to a complicated wake topology.

Surface Pressure

Leading-edge vortices (LEV) and trailing-edge vortices (TEV) are observed on the body of the snake. The presence of LEV and TEV creates regions of low and high pressure, respectively, generating a pressure differential along the entire body. This differential contributes to lift generation. Figure 3.5 (a) displays the pressure coefficient difference between the dorsal and ventral surfaces of the body. A relatively darker region of high-pressure difference ΔC_P on the leading edge of the dorsal surface indicates the location of leading-edge vortices. This observation aligns with Figure 3.5 (b), which shows the lift distribution C_L along the body.

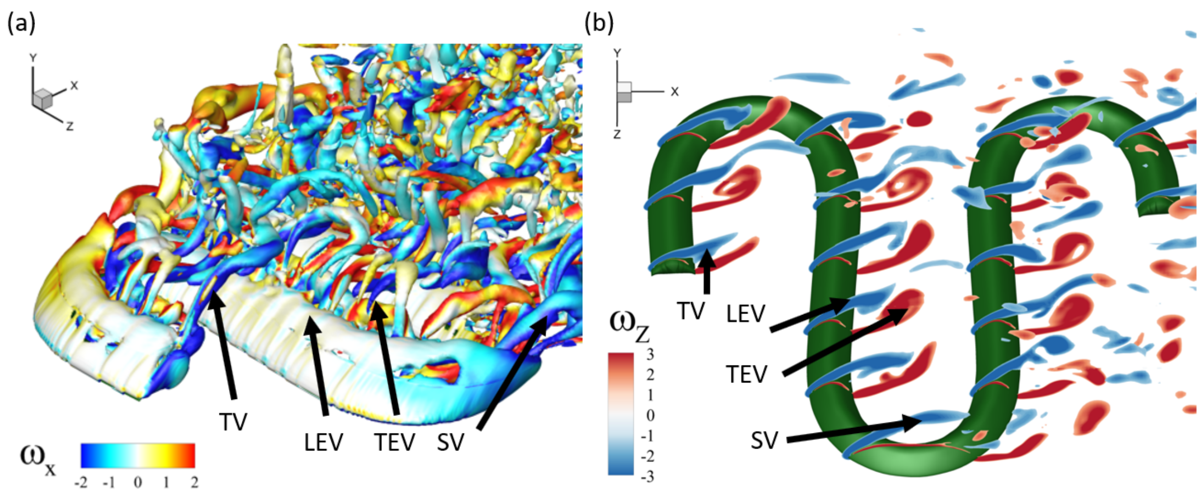

FIGURE 3.4: (a) Perspective view of wake structure of the baseline case at peak lift distribution. The iso-surfaces are plotted using Q-criterion with $Q = 200$ and flooded by X-vorticity ω_X; (b) Vortex structure near the snake body at peak lift distribution. Z-vorticity ω_Z is applied to visualize the vortices on six slices cutting through the body. ω_X and ω_Z are all normalized by U/c.

Areas of high pressure produce greater lift, depicted by deep red zones on the leading edge, whereas green zones, more prevalent at the head, tip, and turning sections of the body, suggest that tip vortices (TV) and side vortices (SV) have a lesser impact on lift generation.

3.1.4 Effect of Body Shapes

This section discusses the impact of varying body shapes on aerodynamic performance. Figure 3.6 presents the cycle-averaged lift coefficient results, highlighting that the body shape in Case 2 achieves the highest lift during gliding. To understand the influence of body shape, we calculate the curvature κ of the snake model's midline. Defining sections of the body with a curvature greater than 0.2 ($\kappa \geq 0.2$) as significantly curved, we observe a general trend where less curved bodies tend to generate higher lift. Detailed data is presented in Table 3.1.

Further validation of our hypothesis is provided in Figure 3.7, comparing Case 2, which yields

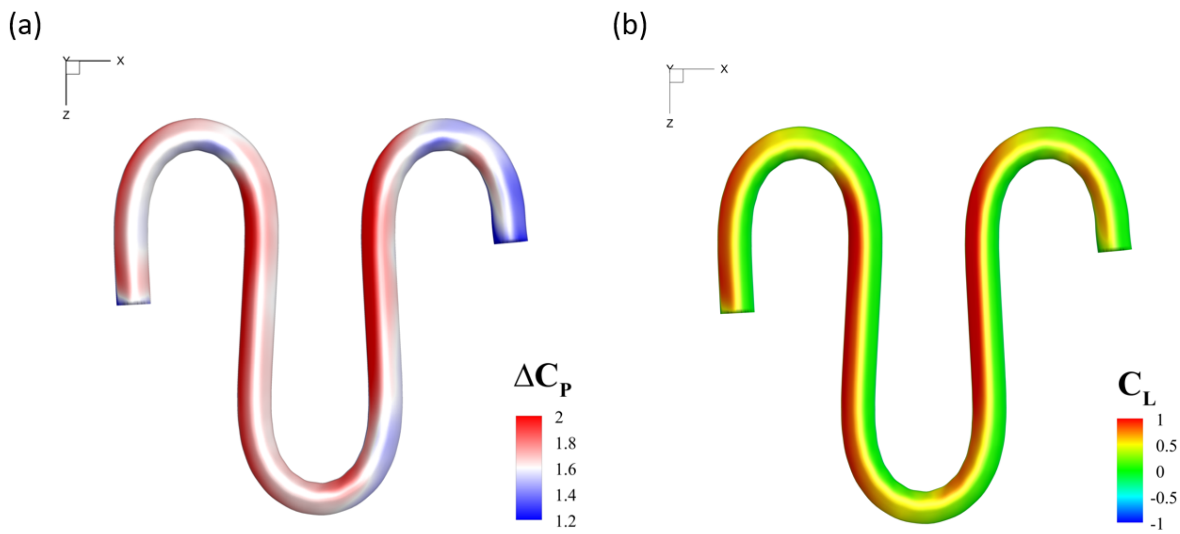

FIGURE 3.5: (a) Pressure difference (ΔC_P) between the dorsal and ventral surface.(b) Lift coefficient (C_L) distribution along the body.

maximum lift and has the least curved body (41.3%), against Case 3, which results in 2.8% less lift due to a longer curved body (45.7%) as the head undergoes a U-turn. To elucidate the differences in lift, we examine the wake structures for these two cases in Figures 3.7(a) and 3.7 (b). In Case 2, the extended straight body fosters a LEV tube on the dorsal surface, significantly enhancing lift generation. Case 3's body shape is unique as the head's turning motion allows the tip vortex (TV) to merge with the side edge vortex (SV), both of which contribute less to lift compared to the straight LEV. This hypothesis is further supported by the lift distribution contours in Figures 3.7(c) and 3.7(d), where the larger red regions in both cases indicate higher lift associated with steady LEV tubes along the straight body segments. The orientation of the head in Case 2, perpendicular to the incoming flow, contrasts with its parallel alignment in Case 3, causing the previously red region on the head to turn green, indicating a reduction in lift distribution.

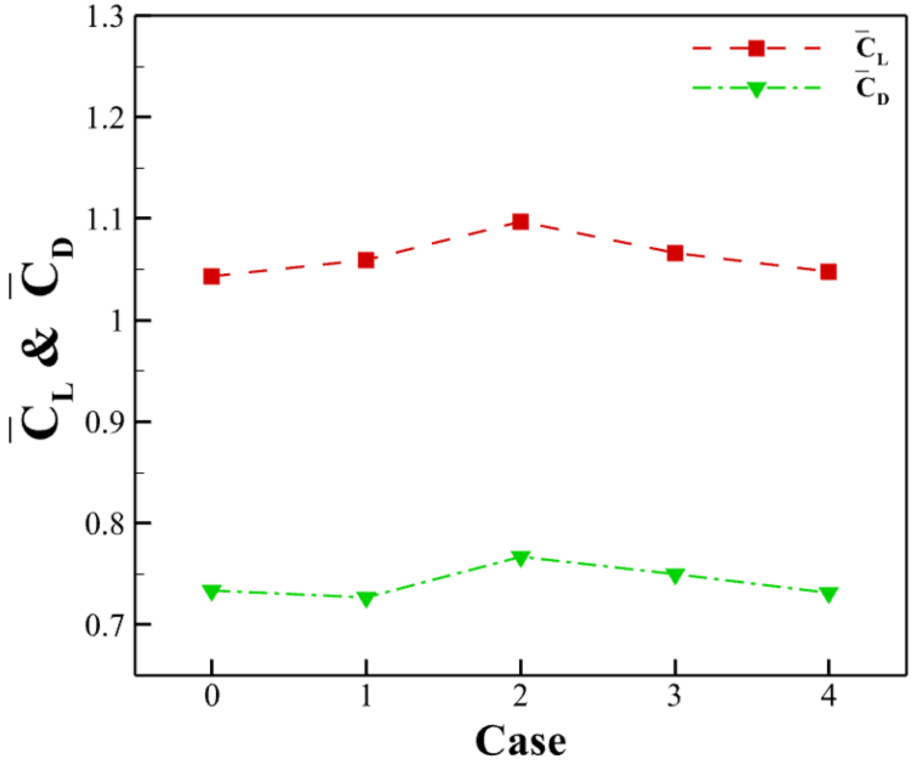

FIGURE 3.6: Time-averaged lift (C_L) and drag (C_D) coefficients of different cases.

Case	0	1	2	3	4
$\overline{C_L}$	1.0436	1.0588	1.0968	1.0657	1.0482
$\overline{C_D}$	0.7332	0.7267	0.7672	0.7500	0.7311
Curved Body Portion ($\kappa \geq 0.2$)	51.1%	45.7%	41.3%	45.7%	52.2%

TABLE 3.1: Aerodynamic performances and curved body portion for different shapes.

3.2 Aerodynamic performance and wake structures of the baseline moving case

Next, we will present the simulation result of the horizontal-undulating model. The baseline case is chosen at AOA=35°, Reynolds number Re=500 and $f_\theta = 1$. We will discuss its performance and wake structures. Also the comparison between the static models and the baseline case will be discussed. Finally, three parametric studies of the effects of AOA, the undulation

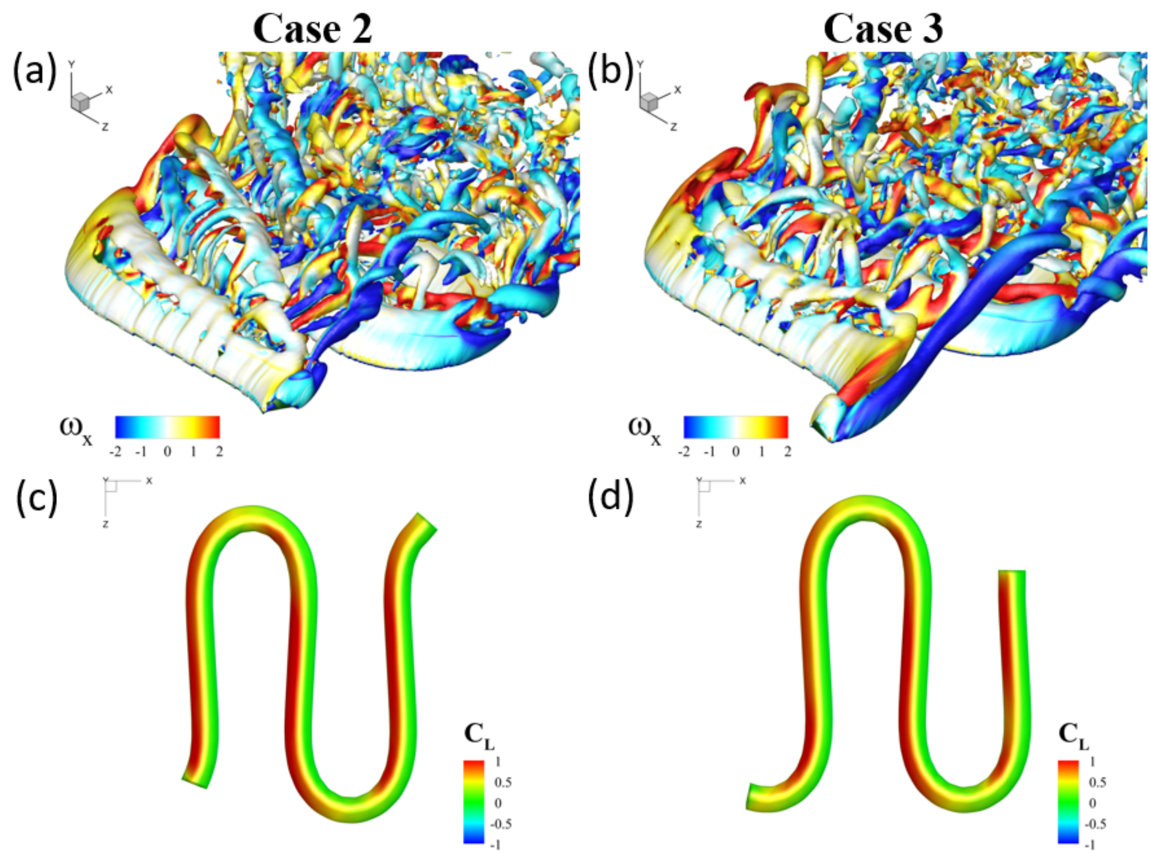

FIGURE 3.7: (a) and (b) show the perspective view of wake structure of Case 2 and 3 at peak lift timeframe; (c) and (d) show the lift coefficient (C_L) distribution along the body of the two cases, respectively.

frequency, and the Reynolds number will be presented in later sections.

To reach stable periodic states, at least four undulatory cycles are conducted in all simulations. Figure 3.8 (a) shows the instantaneous lift coefficient history of one undulating period. Given the mathematical model, it is known that the snake's horizontal undulation can be divided into 2 symmetric strokes. According to the equation of the kinematics, the snake head's position locates in the midplane at the beginning. Its motion can be divided into the first half stroke with the head pointing from right to left (R-L) and the second half pointing from left to right (L-R). Predictably, 2 repeating cycles will appear in the lift force history corresponding with R-L and

L-R strokes, so in later discussions, we will be mainly focusing on the first (R-L) stroke.

In the R-L stroke lift force history, it can be observed that there is one lower peak (ii), one higher (maximum) peak(iv), and a trough (iii). And the symmetric kinematics explains why the peaks share similar amplitude in the L-R stroke. The cycle averaged lift is computed to be (C_L) =0.919.

Figure 3.8(b) gives a detailed description of the vortex topology in the R-L stroke. The 3-D vortex structures are visualized by the iso-surface defined by Q-criterion with Q=120 showing the cyan iso-surface. In the flow equation, the velocity gradient $\nabla\vec{v}$ can be decomposed into two parts as follows:

$$\nabla\vec{v} = \frac{1}{2}\left(\nabla\vec{v} + (\nabla\vec{v})^T\right) + \frac{1}{2}\left(\nabla\vec{v} - (\nabla\vec{v})^T\right) = S + \Omega, \tag{3.1}$$

where S and Ω are the symmetric and antisymmetric part known as the vorticity tensor.Then the Q-criterion is directly derived based on the second invariant Q of the velocity gradient tensor given in the following expression:

$$Q = \frac{1}{2}\left(\|\Omega\|^2 - \|S\|^2\right), \tag{3.2}$$

where $Q > 0$ represents the existence of a vortex[69].From the perspective view of the wake structure, small vortices including the leading-edge vortices (LEVs) and trailing-edge vortices (TEVs) can be seen generating on the snake body surface, which will play the main role in lift generation. LEV is observed generating on the edge facing the incoming flow (known as leading-edge) and the TEV is generated on the other edge.

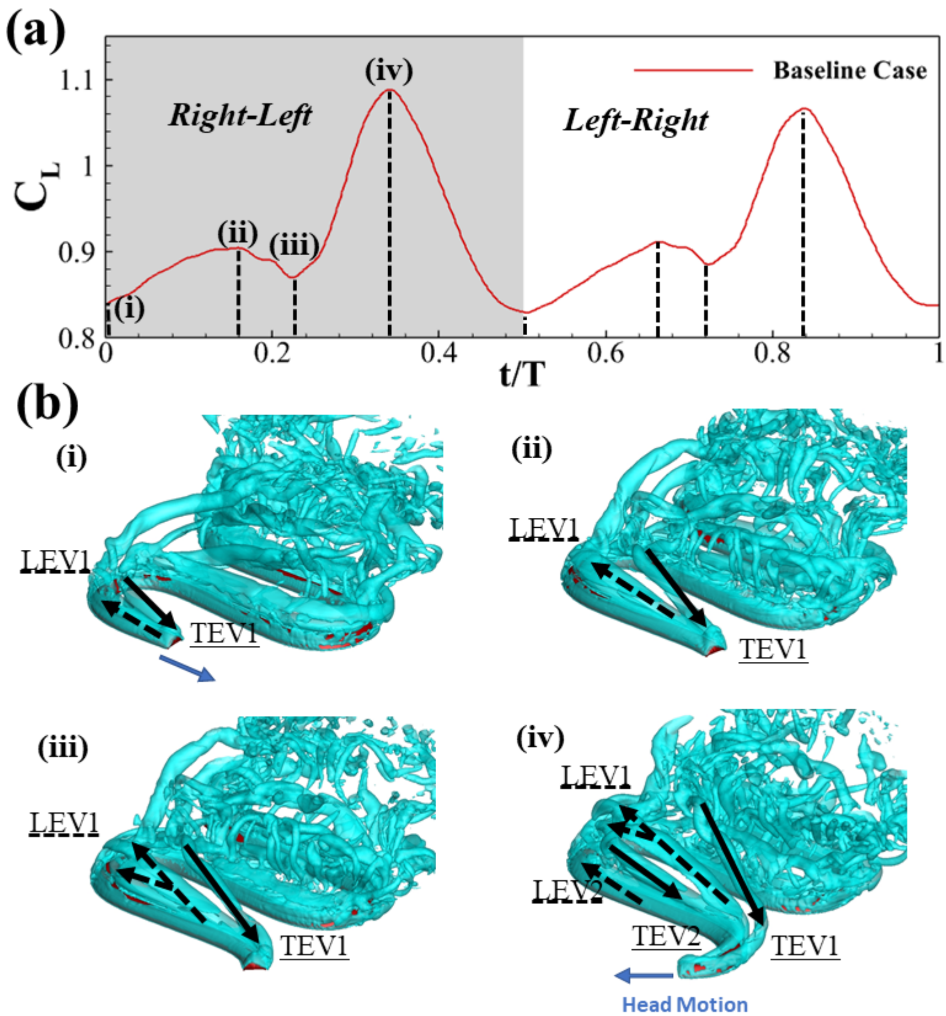

FIGURE 3.8: Flow information for the baseline case (AOA=35°, Re=500 and $f_\theta = 1$). (a) The instantaneous lift coefficient history. (b) Three-dimensional wake structures of flying snake model in the R-L stroke at (i) t/T=0.00, (ii) t/T=0.17, (iii) t/T=0.23 and (iv) t/T=0.34 respectively, from a perspective view. The iso-surface of the wake structures is visualized by Q-criterion with the value of Q=120. The solid arrow indicates the directions of trailing edge vortex tubes (TEV) and the dashed line arrow indicates the directions of leading-edge vortex tubes (LEV).The head turning motion in this stroke is indicated with blue arrow.

At t/T=0.00 (Figure 3.8-b (i)), the starting stage of the R-L stroke, the LEV1 and TEV1 can be identified clearly at the leading edge and the trailing edge of the snake body. The front part of the body elongates with the process of undulation, while the LEV1 is developed and attached to the body. With a longer LEV1 attached to the snake body, an increasing trend in the lift is shown from the start until t/T=0.17. The TEV1, on the other hand, shed off the trailing edge quickly. Either LEV1 and TEV1 forms a vortex tube as shown in Figure 3.8-b(ii), as evidence of the time evolution of vortex-shedding combined with snake body undulation. Similar 2D vortex-shedding process has been presented in the work done by Krishnan et al. [43]. In their flow-past-airfoil studies, it is predictable that an LEV will be generated, developed, separated, and shed off the dorsal surface of the foil. This process can be treated as a reduced-dimension model compared with the 3D flying snake gliding. In the 3D model, with the snake head undulating and moving in the direction perpendicular to the flow velocity, wherever it shows up, the LEV will start the generation process automatically. The head is still generating vortices while the following part of the straight snake body already starts experiencing vortex-shedding at the same time. Thus, a 3D oblique vortex tube is formed as the consequence of the head moving and the snake body afterward.

At t/T=0.23, as shown in Figure 3.8-b (iii), the part of LEV1 generated by the earlier head begins the process of separation and shedding off the body while the 2nd LEV (LEV2) is generated on the straight body at its early stage. A furcation showed in the LEV1 also indicates the gradual process of wake separation, which corresponds with the slight lift drop. TEV2 is also forming simultaneously on the trailing edge at the same time. The hint of TEV2 can be observed in Figure 3.8-b(iv). In Figure 3.8-b(iv), at t/T=0.34 where the highest lift shows up during the R-L stroke, the newly generated LEV2 is fully attached to the snake body and generates considerable lift. Detailed force distribution along the snake body will be presented in a later discussion. The turning motion velocity vector is parallel to the flow vector plane. Following the velocity direction, the edge vortices formed and attached on both sides of the head will also be dragged into the parallel direction to the incoming flow. From the 3D wake topology information in Figure 3.8-b (iv), a pair of spinning tubes can be observed and treated as an extension of TEV1 and LEV1.

After the lift reaches the peak at t/T=0.34, LEV2 will experience the same vortex-shedding process as LEV1 and the same lift drop occurs. At t/T=0.50, where the snake's undulation moves to the axial symmetrical position at the start of the first stroke, the lift falls back to another local trough. Then the second half-stroke (L-R) will start and repeat a similar process as described earlier. Predictably, a pair of similar LEV and TEV as LEV1 and TEV1 will appear at the axial symmetric position as well. Another feature worth noticing is that, although the leading and trailing edge flipped after the head made the U-turn and begin moving rightwards, topologically the newly generated LEV is linked to the previous TEV. and merged to a continuous vortex tube (same with LEV1 and TEV3). Still, we identify them by the generation position on the snake surface and thus named them separately.

The correlation between the formation of LEV2 and the lift enhancement is observed in the R-L stroke especially from t/T=0.23 to t/T=0.34 with an increase in the lift of 25.1% (instantaneous C_L increase from 0.870 to 1.088). To explore the cause of lift enhancement, detailed analyses on the vorticity of LEV were conducted at t/T=0.23 and t/T=0.34, as presented in Figure 3.9. Figure 3.9 (a) and (b) compare the spanwise vorticity contour on slices cutting through the snake's straight body between the two timeframes mentioned above. The LEV is shown in blue color contour and TEV in red, which is showing their direction as well. The slices 1-4 are located at Z = 3c, 1c, -1c, and -3c, based on the center of the mass coordinate system where the center of mass is located at the origin point. Transparent Q-iso-surfaces are also displayed along with the vorticity slice cut, to illustrate the significance of leading-edge vortices.

Figure 3.9 (c) and (d) are the corresponding 2D vortex contours on each slice at 2 different times. The LEV1 is shown in all slices colored in blue. From slice 1 to 4, a complete 2D vortex generating-shedding process is reproduced. In slice 1 the LEV1 is generating and closely attached to the snake body while the TEV1 is fully developed and about to shed off the trailing edge. All along to slice 4, a clear LEV1 shedding is observed and the new TEV2 is generated. In Figure 3.9 (d) slice1, after t=0.11T, the LEV1 attached to the body begins to shed off. This process is also observed in slice 2 and 3, while in slice 3 the LEV1 is completely shed off the body and a new LEV2 is generated on the surface body. In later sections, we will discuss more details about the LEV's role in lift maintenance.

The main theory of lift generation and maintenance is caused by the pressure difference on dorsal and ventral surfaces. Figure 3.9 (e) and (f) show the pressure iso-surface at the 2 timeframes. It’s easy to observe and define the dorsal surface as a low-pressure region (suction surface) and the ventral surface as a high-pressure region (pressure surface). The pressure difference contributes to both the lift and drag force on the snake body.

Figure 3.10 shows the lift distribution over the cycle along the body. More lift is generated on the anterior body compared with the lateral body. The overall trend of the lift distribution

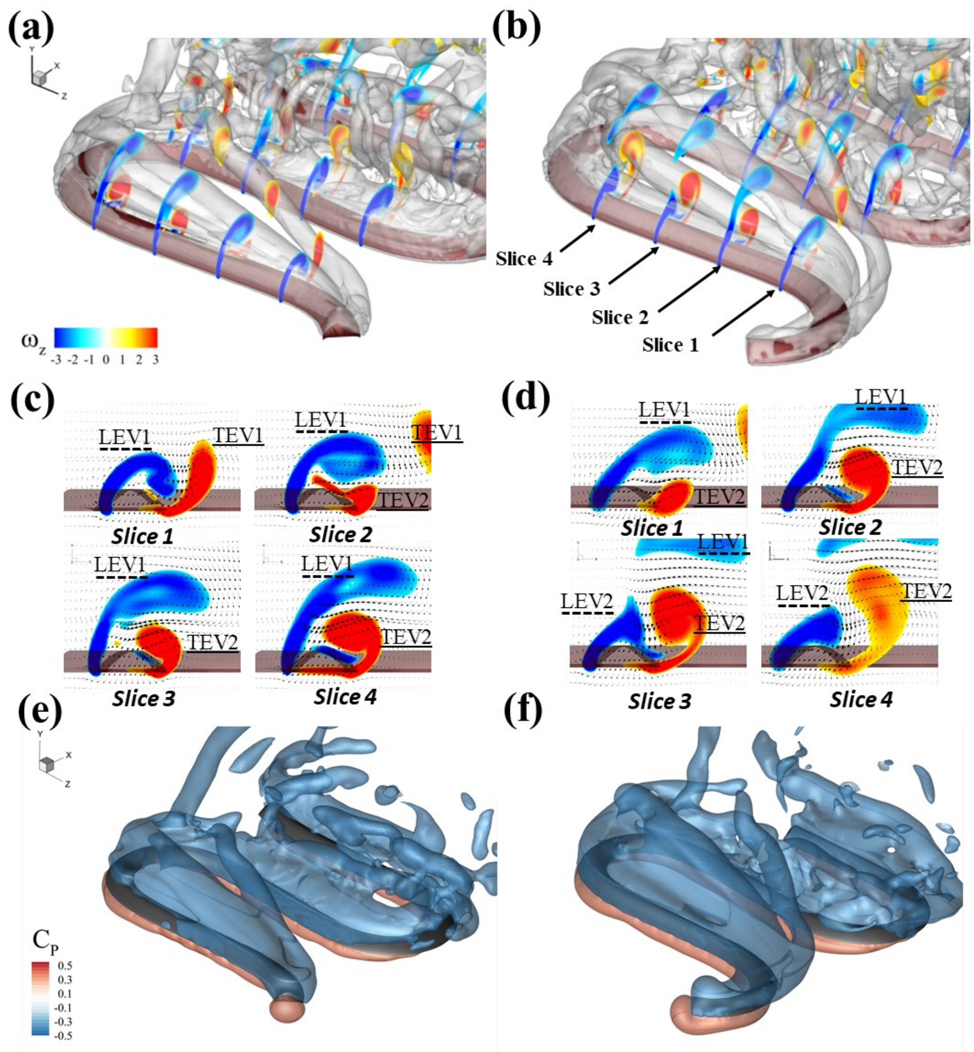

FIGURE 3.9: Comparison of instantaneous vortex structure at t/T=0.23 (lift trough) and t/T=0.34 (lift peak), (a) and (b), respectively. (c) and (d) show the 2D spanwise vorticity contour (showing LEV1, LEV2 and TEV1, TEV2) on the anterior snake body at the corresponding timeframes. The slice-cuts are located at z/c= -3, -1, 1, and 3. (e) and (f) show pressure coefficient iso-surface visualized by $C_P = -0.4(blue)$ and $C_P = 0.4(red)$ at the two timeframes, respectively.

is affected by the motion of horizontal undulation, showing a traveling wave passing down the body. One unique feature of the lift appears at t/T =0.34. Another local lift peak arises, generating extra lift which is also reflected in the lift force history in Figure 3.8 (a). This feature indicates that within the whole undulation motion, the vortex structure near the anterior body would be focused and analyzed in detail.

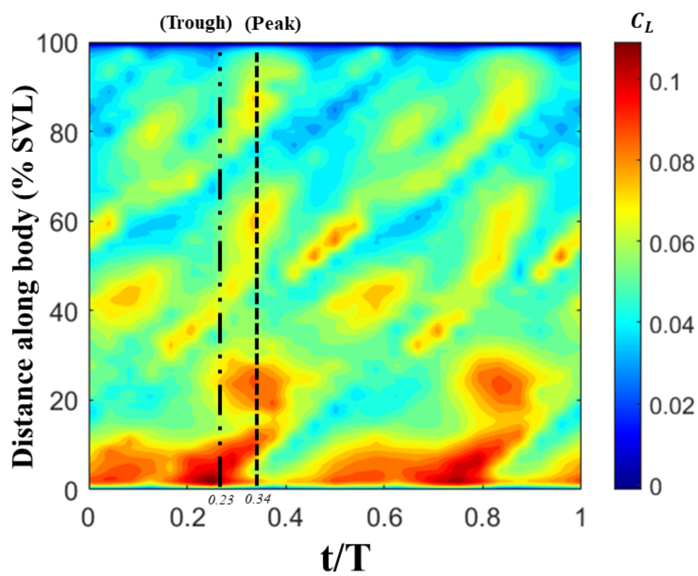

FIGURE 3.10: Lift distribution over the cycle along the body. Dash-dot-dot line and short dash line indicate the time with the trough(t/T=0.23) and peak(t/T=0.34) overall value, respectively.

In Figure 3.11, the two timeframes indicated with dashed lines are further investigated. Figure 3.11 (a) and (b) show the LEV on each slice cut on the anterior body at t/T=0.23(trough) and t/T=0.34(peak), respectively. The circulation peak corresponds with the higher lift generation. It's observed that the circulation at slice 1 appears to be one high peak, which both in t/T=0.23 and t/T=0.34 indicates the existence and attachment of LEV1 since it's closer to the head and the vortex hasn't been shed off. This observation can be proved with the calculation of Γ in Figure 3.11 (c). The decrease of circulation at slice 2 also indicates the development of LEV1 and possible vortex-shedding. The difference between lift-peak and lift-trough happens at slice 3 and 4, which can be reflected by local circulation. The newly generated LEV2 is responsible for the circulation increase which is not generated yet at t/T=0.23.

In order to give another picture to illustrate the lift generation, we focus more on the overall lift distribution on the snake body. Figure 3.11 (d) and (e) are the lift coefficient surface contour at trough and peak. The red region indicates the strong LEV generated on the dorsal surface of the body. It's easy to identify the LEV1 at t/T=0.23 with a red region near the head region. At t/T=0.34, both LEV1 and LEV2 can be observed near the anterior body. Another feature that needs attention is the lift-concentration region at the curved body. At the second and the third portion of curved body (the head region at the current timeframe is considered as the first turning segment), the LEVs are generated and maintained on the dorsal surface. This can be explained similarly as LEV1 that at the curved body, the LEV is forced to be maintained on the body surface longer due to the flow around it instead of naturally being shed off.

Figure 3.11 (f) shows the local lift distribution along the body to further illustrate the region of lift generation. At t/T=0.23, 3 major peaks can be identified at around s=0.05, 0.4 and 0.75. These correspond with the three red zones in Figure 3.11 (d). At t/T=0.34 when the maximum lift is generated, the fourth peak of lift shows up at around s=0.3, indicating the appearance of LEV2. The other three peaks maintain and shift to the location at s=0.15, 0.5, and 0.85. The generation LEV2 does a major contribution to lift increase.

A previous study done by Gong et al. [70] showed some preliminary understanding of static snake models. They have a similar wave shape as the dynamic models yet their motion is

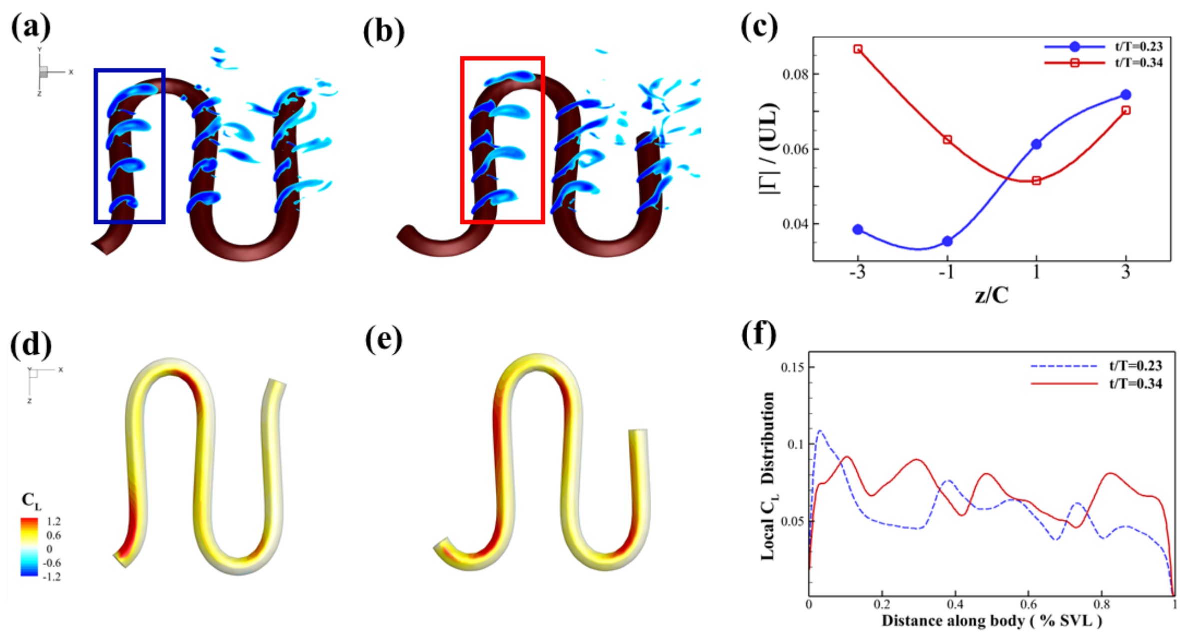

FIGURE 3.11: (a) and (b) are the perspective views of the snake with 2D span-wise LEV vortices on slice-cuts at t/T=0.23 (lift trough) and t/T=0.34 (lift peak), respectively; (c) Normalized circulation |Γ| of LEV at the anterior body on different slice-cuts at t/T=0.23 and 0.34. Γ is normalized by UL; (d) and (e) are the top view of the snake showing the lift coefficient surface contour at t/T=0.23 (lift trough) and t/T=0.34 (lift peak), respectively; (f) Local lift coefficient distribution along the body at t/T=0.23 and 0.34.

excluded so they keep steady at certain positions. Similar vortex structures were observed in steady models. The LEV is still playing the dominant role in lift generation. The static model with a maximum portion of the straight body will generate the longest LEV tubes, thus contributing to most lift generation. However, the conclusion is different when introducing the dynamic motion.

For comparison, we created two static models which are achieved by setting the undulation frequency $f_\theta = 0$. The different positions can also be reproduced by applying phase change $\phi_\theta = 0$. Figure 3.12 shows the flow feature of the static snake model. The static undulation position at t/T=0.00 and t/T =0.34 were chosen to conduct the simulation. Figure 3.12 (a) and

(b) give the vortex structure at the lift peak. From the vortex structure, we observe parallelly generated leading edge vortex tubes. This feature also corresponds with the lift distribution on the surface in Figure 3.12 (c) and (d). The lift on static cases is more equally distributed along the leading edge. At position t/T=0.34, another obvious feature is the tip vortex (TV) generated on the dorsal and ventral surface of the tail. Due to the shear layer of the tip vortices, position B has a lower cycle-averaged lift than position t/T=0.00. To further illustrate the difference between static and undulating models, Figure 3.12 (f) shows the cycle-average value contour of the lift coefficient along the snake body. The steep increase and decrease of the lift at 0% SVL (head) and 100% SVL (tail) are due to tip vortices. Static cases at t/T=0.00 and t/T=0.34 give a more equally distributed lift along the body, with several local troughs indicating the curved segments where the lift is less generated. The baseline undulating case shows a concentrated lift generation area at the anterior part of the snake where a peak of lift can be observed between 0 –20% SVL. According to the contour distribution, the undulation provides a more equally distributed lift compared with static cases, which have a significant lift decrease at the curved body. The concentrated force at the anterior body would provide a torque with respect to the body's center of mass that helps the head pitch. The lift concentration will be discussed in our study about the effect of AOA, Reynolds number and undulating frequencies and we will more focus on the anterior body of the snake.

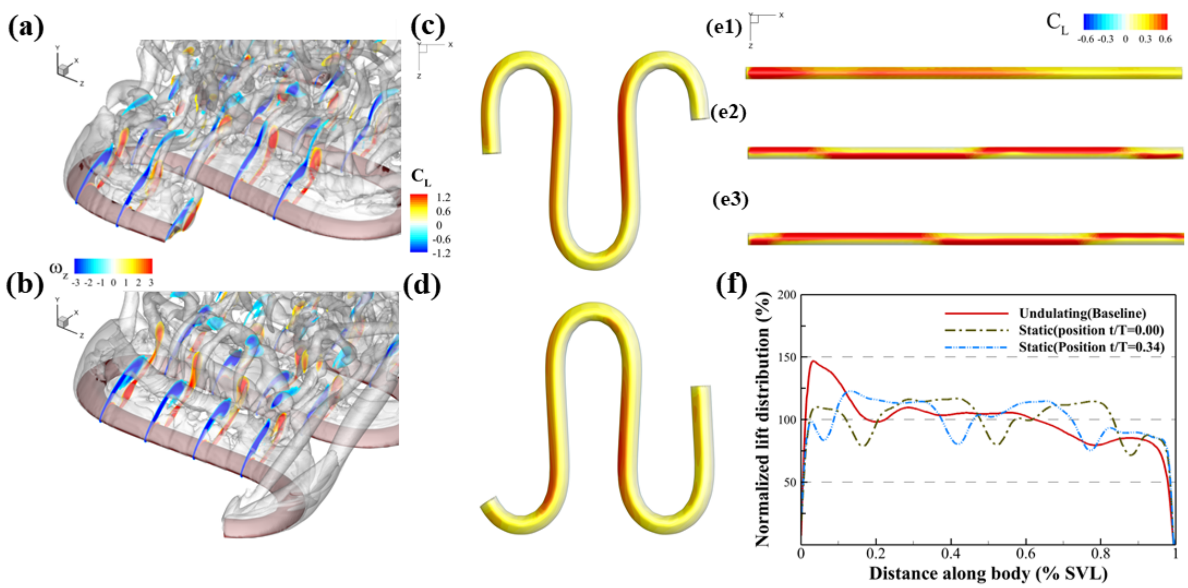

FIGURE 3.12: (a) and (b) show the vortex structure at static position A (same shape as t/T=0) and B (same shape as t/T=0.34) and the LEV and TEV on 2D slice cuts, respectively. (c) and (d) show the lift distribution contour on the contour when they are at peak lift production. The cycle-averaged lift distribution on the model dorsal surface is shown with the baseline case (e1), static position A (e2) and B (e3); (f) shows the corresponding normalized lift distributions along the body (from snout to vent, SVL).

3.3 Effects of the Angle of Attack

In this section, we would focus on the effects of the angle of attack (AOA) on the aerodynamic performance and wake structures of the flying snake. To better illustrate the effect on the aerodynamic force, Figure 3.13(a) shows the cycle-averaged values for different AOA including the lift and drag coefficients from 0° to 60° with an increment of 10° (2 more intersect points were added at 35° and 45° to capture the maximum lift). In the curve, there is an increase in the lift before AOA 45° and a decrease afterwards. The drag force curve appears to be a monotonic increasing trend within the current range. The result is partly consistent with the previous 2D studies [42], [43] about the lift and drag trend. The stall happens at a critical AOA and the flow separation begins. Further details will be discussed on why the lift peak is achieved at 45° with the value of C_L =0.964 instead of 35° as previously shown in Krishnan et al.'s work [43]. This AOA is also within the range of other gliding animals such as lizards which also applies average AOA at 40.4° ± 5.7° [71].

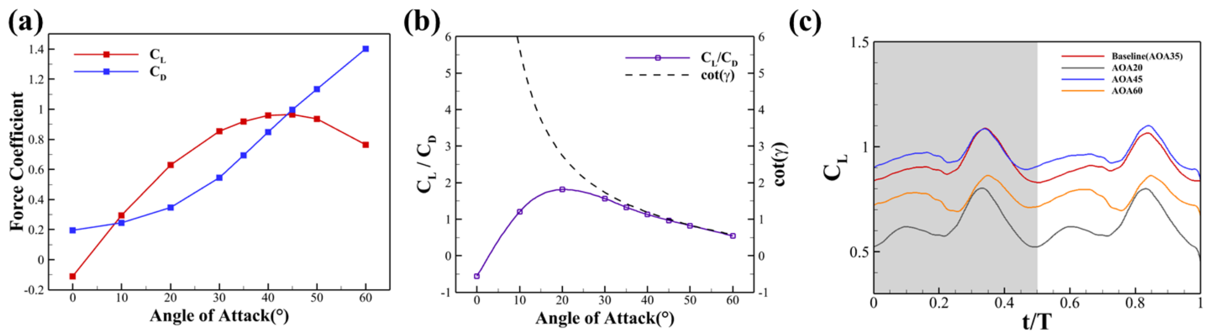

FIGURE 3.13: (a) Cycle-averaged lift and drag coefficients at various AOAs; (b) Lift-to-drag ratio and cot(γ) (glide angle function) (c)Instantaneous lift coefficient at AOA 20°, 35°, 45°, and 60°, respectively.

Figure 3.13(b) shows the lift-to-drag ratio $(C_L)/(C_D)$ at different AOAs. At 20° the lift-to-drag ratio reaches its peak. The black dashed line is the $cot(\gamma)$ function. According to the discussion by Socha [8], they used the minimum glide angle to compute the glide ratio for the trajectory, while the glide angle can be defined with [72]

$$L/D = cot(\gamma) \tag{3.3}$$

The equation shows that at the equilibrium gliding state, the glide ratio is equivalent to the lift-to-drag ratio, and also equal to the cotangent of the glide angle. In our current study, the lift-to-drag ratio curve correlates with the cotangent function perfectly at a relatively higher AOA (>30°). At lower AOA (<20°), the lift-to-drag ratio has a positive correlation with AOA while the glide angle does not. One possible explanation for this phenomenon is to treat the simulation as a quasi-equilibrium gliding status. Different AOAs correspond with a short period on the gliding trajectory. At higher AOAs, the force generated on the surface body would only be provided to balance the gravity. Yet at lower AOAs, less lift is provided compared with drag so that the resultant force will provide less force to balance gravity and a resistance force in the horizontal direction.

Figure 3.13 (c) is the instantaneous lift coefficient at AOA 20° (with maximum lift-to-drag ratio), 35° (the baseline case), 45° (with maximum cycle-average lift), and 60° (with minimum drag-lift ratio after stall) within 1 repeating undulation cycle. Similar to the baseline case, the lift coefficients reach the first trough at around t/T=0.20, and then begin to increase until the peak shows up at around t/T=0.34. The similar trend of the lift curve reveals the fact that lift generation has a strong relation with temporal undulation position and there exists a universal lift generation mechanism with horizontal undulation motion.

Figure 3.14 (a)-(c) shows the vortex structure, the lift coefficient contour on the dorsal surface, and pressure iso-surface around the body (light blue at C_P=-0.4 and light red at C_P=0.4) at AOA 20°, 45° and 60°, respectively. These snapshots are chosen at the highest instantaneous lift, similar to the way we analyze the baseline case. The universal lift and drag generation mechanism keeps the same. The high-pressure and low-pressure regions which can be identified with the pressure iso-surface plot provide the suction and lift force on the dorsal and ventral surface. The pressure difference would contribute to a total force, and could be projected on the lift(perpendicular to flow velocity) and drag (parallel to flow velocity) direction.

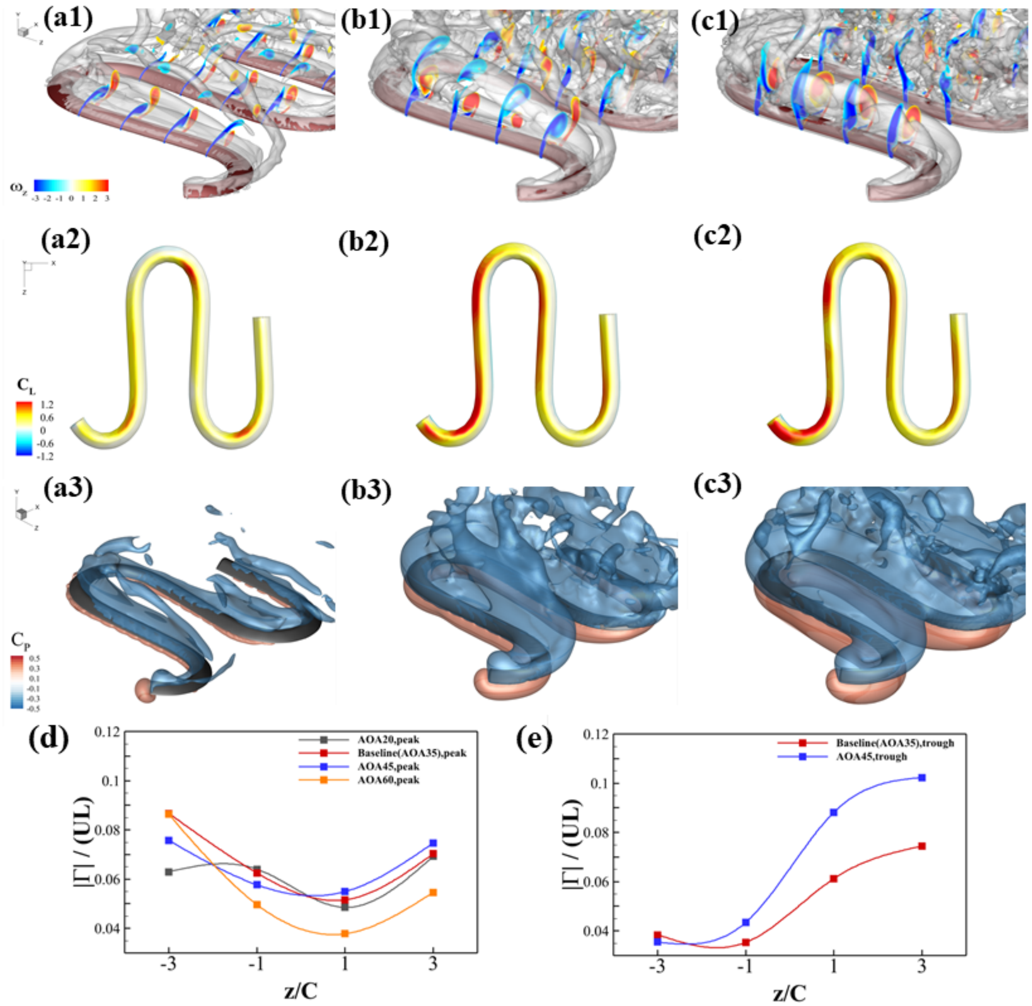

FIGURE 3.14: Comparison of flow structures at different AOAs (20°, 45°, and 60°), including vortex structure and 2D spanwise vortices on slice-cut [(a1)–(c1)], lift coefficient surface contour [(a2)–(c2)], and pressure iso-surface visualized by C_P = -0.4 (blue) and C_P = 0.4 (red) [(a3)–(c3); (d) normalized circulation of LEV at anterior snake body on different slice-cuts at t/T = 0.34 (peak lift) with AOA 20°, 35°, 45°, and 60°; (e) normalized circulation of LEV at anterior snake body on different slice-cuts at t/T= 0.23 (trough lift) with AOA 35° and 45°.

LEV formation plays an important role in lift production. Starting from a lower AOA(20°), LEV1's shear layer is closely attached to the anterior surface body. At the critical AOA (45°), the LEV1 and LEV2 can be clearly shown in the slices with 2 corresponding lift concentrations occurring on the surface. The LEVs are strong and attached to the leading edge which leads to high performance in lift generation. In comparison, at higher AOA (60°), due to the separation of LEV, the strength of LEV decreases, and lower lift can be generated. This also corresponds with the lift contour where the less red area can be observed on the anterior body

Figure 3.14 (d) shows the circulation of the LEV on the anterior snake body at AOA 20°, 35°(baseline case), 45°, and 60°. The circulation is normalized by UL. The universal troughs at z/c=1 are observed, indicating the transition region between LEV1 and LEV2, two relatively higher circulation sections at both ends. This proves that the 2 LEV vortex tube generation is not affected by the change of AOA. However, the circulation will be changed at different AOAs and its trend corresponds with the lift coefficient, increases at lower AOA, and begins to decrease after a critical point. Interestingly, the circulation at AOA 45° is slightly lower than that of AOA 35°. For the two chosen AOAs, the average circulation values of all 4 slices are $|\Gamma/UL|$ (AOA 35°)=0.06780 and $|\Gamma/UL|$ (AOA 45°)=0.06870. This result corresponds with the finding in the instantaneous peak lift coefficient. From Figure 3.13(c), it is found that C_{L-peak}(AOA 35°)=1.0881 while C_{L-peak} (AOA 45°)=1.0854. AOA 45° outreaches the cycle averaged lift coefficient due to a higher trough lift. In Figure 3.14(e) the normalized circulation is specifically calculated at AOA 35° and 45° at their first lift trough, which is around t/T=0.23. There is no surprise that despite the similar mechanism of a single LEV1 generating lift while LEV2 is not formed yet at this time frame, a significant increase in circulation on each slice can

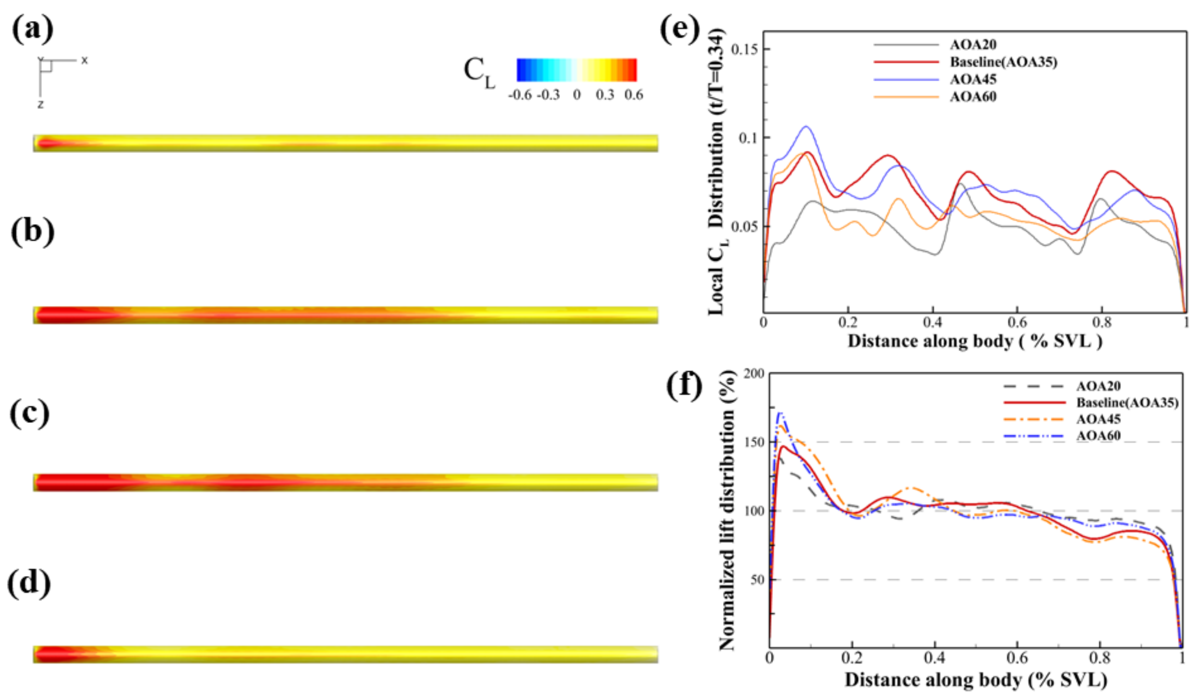

FIGURE 3.15: (a)-(d) cycle-average C_L contour on the straight body's surface at AOA 20°, 35°, 45°, and 60°, respectively; (e) C_L distribution along the body at t/T=0.34, at four different AOAs, respectively. (f) Normalized cycle-averaged chord C_L distribution along the body at different AOAs.

be observed comparing AOA 45° with AOA 35°.

Figure 3.15 (a)-(d) shows the cycle-average lift coefficient contour along the body at AOA = 20°, 35°, 45°, and 60°. The concentration of lift coefficient at the anterior snake body can be easily observed at different AOAs. Furthermore, the increase and decrease of the red area correspond with the trend of the lift coefficient. The location of strong LEV generation can be further illustrated in Figure 3.15 (e). At peak lift moment, the variation of AOA does not significantly affect the mechanism of LEV1 and LEV2 development on the anterior body. The turning body sections, which correspond with s/SVL = 0.5~0.6 and 0.8~0.9, also show evidence of local lift peak which indicates the turning to be the main lift generation area. Figure 3.15 (f) shows the normalized lift distribution, which is defined as the ratio of the local lift coefficient and the overall averaged lift coefficient $(C_L/\overline{C_L})$ along the body, all along the body. There is a peak lift distribution observed at the head of the snake body, and the peak value increases with the increase of AOA. This phenomenon can be interpreted as the consequence of the LEV constantly produced at the head of the body.

3.4 Effects of undulation frequency

In this section, we examine the effect of undulation frequency. According to previous experiments, snake undulation has a specific range of frequency f_θ from 1Hz to 2Hz in nature [30]. In the simulation, we will use the similar concept of reduced frequency (f, also referred as frequency in the following discussion) as study of spanwise oscillating gliding plate [73], which in our study is normalized with the body length L and flow speed U,

$$f = f_\theta L/U \tag{3.4}$$

Figure 3.16 (a) shows the cycle-averaged values including the lift and drag coefficients for different f. The overall trend is observed as a monotonically increase in drag coefficient and a monotonically decrease in lift coefficient. The lift-to-drag ratio result is presented in Figure 3.16(b). The overall trend of the ratio is to decrease with the increase in frequency. Within the natural frequency range, the overall aerodynamic performance decreases when the undulation gets more intense.

Figure 3.16(c) is the instantaneous lift coefficient corresponding to undulating frequencies

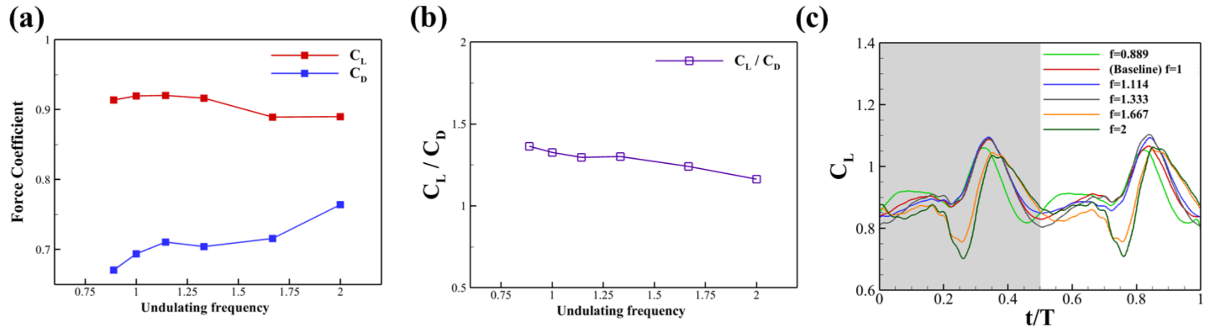

FIGURE 3.16: (a) Cycle-averaged $\overline{C_L}$ and $\overline{C_D}$, at different undulating reduced frequencies. (f=0.889, 1, 1.143, 1.333,1.667 and 2, corresponding with simulation period of T=9/8, 1, 7/8, 3/4, 2/3 and 1/2); (b) Lift-to-drag ratio at different undulating frequencies; (c) Instantaneous force history during a repeating undulating cycle at corresponding frequencies.

within a repeating undulation cycle. Trough and peak happen at similar times indicating the similar lift generation mechanism due to the undulating phase and is rarely affected by frequency change. Yet at higher frequencies (f =1.667 and 2), the trough is significantly lower than that of lower frequencies, which leads to a drop in the overall lift coefficient. It is noticeable that the L-R and R-L stroke peak values are slightly different and similar phenomenon is also observed in the effect of AOA study. The difference between two strokes is less than 1% is for most cases. For some cases with highly unstable flow separation, the two strokes may experience LEV and TEV shedding at different time scales, which will cause asymmetric force production.

The first row in Figure 3.17 ((a1) - (d1)) show the vortex structure at the frequency of 1.143, 1.333, 1.667, and 2. The general trend is that the frequency increase leads to the instability of the vortex structure. The snake undulation provides a wave propagating backward on the body. With a higher undulation frequency, the body possesses a faster motion both in X (incoming flow) and Z (transverse flow) directions. This leads to a larger transverse speed and a relatively small local incoming flow speed. The increase in speed leads to several vortex features. From the 2D Z-vorticity (ω_Z) contour slice-cuts we can tell that higher frequency corresponds with a larger local angle of attack. At lower frequencies (f=1.143 and 1.333), the local AOA is smaller so that the LEV1 is more stable and more attached to the surface. While at higher frequencies, the LEV1 is nearly perpendicular to the chord-wise direction which indicates that it separates from the body at an earlier stage. Another feature is that at f=1.143, LEV2 is still able to be observed at z/c=-3, yet when the frequency increases, LEV2 is no longer seen on the anterior body. This phenomenon can also be explained by the undulating motion. According to the vortex time-evolution process described in the baseline case, there is less time left for the vortex shedding and regeneration process when the transverse flow speed is larger. A similar effect also happens when the local incoming flow speed is lower so that the LEV generation process is slower. The third feature is the unsteadiness of the whole vortex tube. On the outer surface of each turning position, there appears a spinning vortex tube linking TEV which is caused by the turning and attachment of the body. At higher frequencies with higher local transverse flow speeds, the spinning vortex tubes tend to detach from the outer surface due to larger centrifugal force, which will lead to a decrease in lift generation in related regions. Finally, the whole vortex structure tends to break down and develop smaller structures due to the unsteadiness of the flow.

The second row in Figure 3.17 ((a2) - (d2)) present the lift coefficient contour on the dorsal surface of the snake body which corresponds with the aforementioned lift concentration feature. At the region around z/c =-3, a shallow red region is observed at z/c =-3 (slice 4). At higher frequencies, there are no significantly seeable red regions at slice 4, which indicates that LEV2

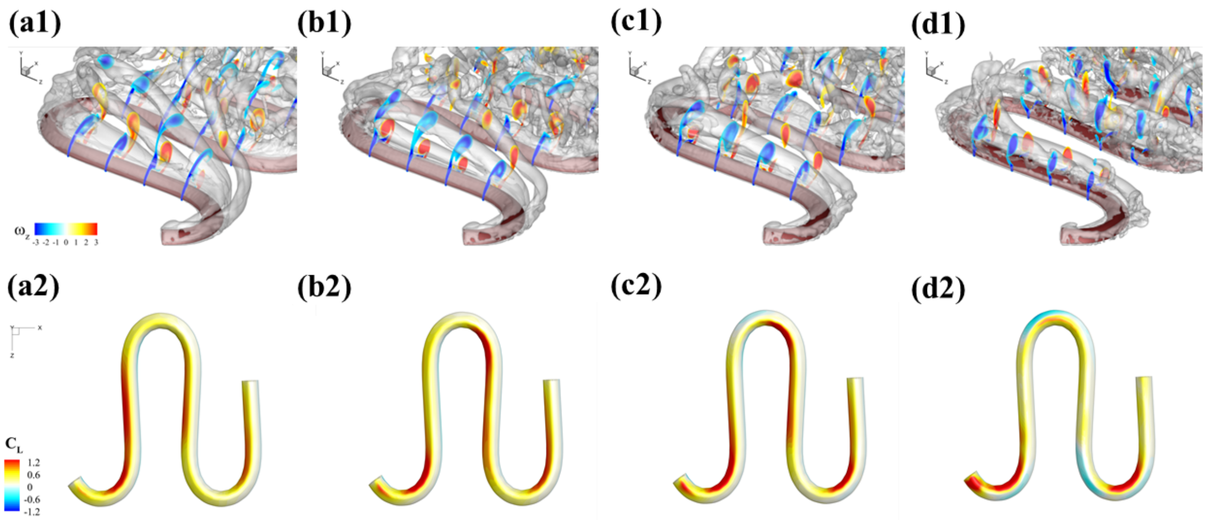

FIGURE 3.17: Comparison of flow structures at t/T=0.34 with different undulating frequencies f= 0.889 (a1), 1.143 (b1), 1.333 (c1) and 2 (d1). C_L contour on the surface of the snake model body at four frequencies are shown respectively in (a2), (b2), (c2) and (d2).

is not generated at the corresponding region. Another significant difference that can be observed is the blue region on the dorsal surface. The Blue region provides a negative lift that appears at the outer surface of the turning body. This result provides support for the detachment of spinning vortex tubes.

Figure 3.18 (a) shows the normalized circulation of LEV at the anterior snake body on different slice cuts at t/T=0.34 (peak lift) with various frequencies. The development of LEV2 can be clearly observed when the frequency changes from 0.889 to 1.142. At higher frequencies, the peak vanishes due to the instability and insufficient time for LEV2 generation. Yet from Figure 12 (a) the peak lift coefficient (at around t/T=0.34), the maximum is (C_{L-peak}) (f=1.143)=1.095 and the minimum is (C_{L-peak}) (f=2.000)=1.025. Although the LEV2 is not observable in high-frequency undulation, the peak lift decreases only by 6%. The reason why the snake can maintain a high lift will be discussed with further information in Figure 14 (b)

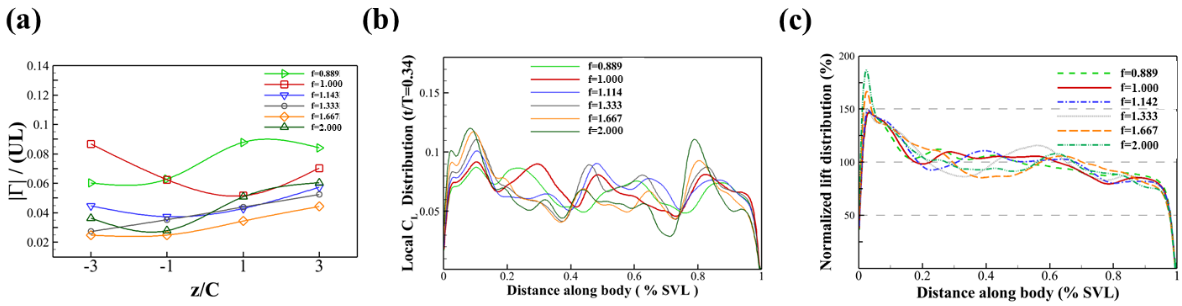

FIGURE 3.18: (a) Normalized circulation of LEV at anterior snake body on different slice-cuts at t/T=0.34 (peak lift) with various frequencies. (b) C_L distribution along the body at t/T=0.34, with five frequencies, respectively. (c)-(f) cycle-average C_L contour on the straight body surface at four frequencies respectively; (c) Normalized cycle-averaged C_L distribution along the body at different frequencies.

and (c).

Figure 3.18 (b) shows the lift distribution along the body at t/T=0.34(peak lift), with different frequencies. It's still easy to observe that at the portion of the curved body, which corresponds with s/SVL = 0.5~0.6 and 0.8~0.9, there are still local (C_L) peaks. And the local peak value is higher at a higher frequency, which would compensate for the missing LEV2 to some extent. This phenomenon can be explained by the fact that higher local speed during turning motion will help the spinning vortex tubes get attached to the inner surface tighter, providing higher lift in the local region.

Another feature noticeable is the concentration of lift on the head region. Figure 3.18 (c) shows the cycle-averaged lift along the body with normalized value. With the increase of frequency, a higher peak of lift can be seen at the head region at s/SVL=0.05~0.1. This phenomenon may indicate that higher undulation frequency generates higher torque on the anterior body which may help the snake pitch and increase its maneuverability. Further study needs to be conducted before concluding.

3.5 Effect of Reynolds Number

This section mainly focuses on the simulation results for different Reynolds numbers. Reynolds number indicates the viscous force effect of flow. Previous studies have been conducted to illustrate the effect of the Reynolds number on 2D snake-shaped airfoils [43], 3D revolving wings [68], or hummingbird [51]. The general conclusion is that a higher Reynolds number leads to a more complicated vortex structure but stronger vortices. Figure 3.19 (a) shows the vortex structure at Re=1000 with iso-surface value Q=200. As expected, the LEV1 and LEV2 identified in the baseline case (Re=500) are also observed on the anterior snake body. As the Reynolds number increase, the vortex becomes stronger indicated by a thicker iso-surface. The instability of the vortex also increases with the Reynolds number increase. Compared with the smooth and steady LEVs at Re=500 and Re=1000 the vortices developed smaller and more complex structures. The vortex tubes appeared to be broken down and unsteady and tended to interact with each other.

Figure 3.19 (b) shows the effect of the Reynolds number on the lift coefficient. It can be seen that all force history lines followed a similar pattern. Considering the symmetric motion of the snake body, we observe the first half cycle as a featured period. Similar to the baseline case, the lift coefficient trough and peak appear synchronously, indicating once more that the lift generation mechanism is only related to the undulation position and is not significantly affected by the Reynolds number. However, it is seen that as the Reynolds number increase, the aerodynamic performance improves by generating more lift. The cycle-averaged lift values

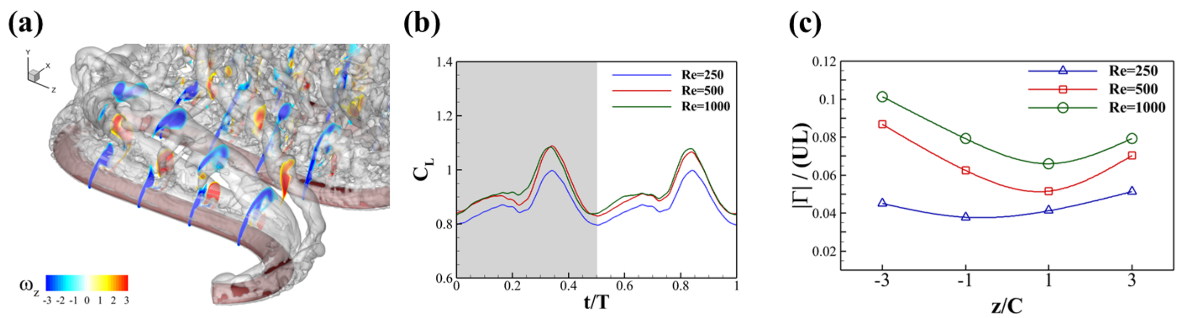

FIGURE 3.19: (a) Vortex structure and 2D spanwise LEV and TEV vortices on slice-cut at Re=1000. (b) Instantaneous force history curve during a repeating undulating cycle at corresponding Reynolds number (Re=250, 500, and 1000). (c). Normalized circulation of LEV at anterior snake body on different slice-cuts at t/T=0.34 (peak lift) at corresponding Reynolds number.

are $(\overline{C}_L)$=0.8719 at Re=250 and $(\overline{C}_L)$=0.9242 at Re=1000. This also corresponds with previous findings on the strengthening of vortices.

Figure 3.19 (c) further illustrates this finding by showing several slice cuts of the LEVs and their normalized circulation on the anterior body. The overall trend of circulation is increasing with the Reynolds number. 2 peaks of circulation at both ends indicate the coherence of LEV1 and LEV2 identified in the baseline case. The generation of LEV2 is not strongly affected by Reynolds numbers despite the fact that at lower Reynolds numbers LEV2 is weaker than that in higher Reynolds numbers (Re=500,1000).

Furthermore, the Reynolds number effect is reflected on the components of viscous force and pressure force in lift and drag. The following Table 3.2 shows that with the increase of Reynolds number, the viscous force contributes less in the lift generation, which is consistent to our knowledge in Reynolds number study.

Re	250	500	1000
$C_{Lpressure}/C_L(\%)$	98.96	99.57	99.81
$C_{Lviscous}/C_L(\%)$	1.04	0.43	0.19

TABLE 3.2: Percentage of pressure force and viscous force in lift generation for different Reynolds number.

3.6 Discussion:The comparison between 2D and 3D models

Based on our study, we have expanded our study based on the 2D cross-sectional shape to the 3D steady horizontal shape, then further with the horizontal undulation motion. For comparison, we evaluate the force coefficients in different conditions in Table3.3. According to the data, the 3D steady formation will reduce the lift production by about 40% compared with the 2D cross-sectional shape model, and the horizontal undulation will further more reduce the lift production by 16.4%. This phenomenon is predictable due to the finite shape of the model and the tip and side vortices (TV and SV) cannot maintain as high lift as the LEV. And for future flying snake robot design, this data can be applied as a guidance to evaluate the force production and gliding performance. In the following chapters, we will compare the aerodynamic performances with more complicated undulation motion then discover the compensation in controlling with such motion.

Case	$\bar{C_L}$	$\bar{C_D}$	L/D
2D cross-sectional shape	1.8355	1.1353	1.6167
3D static model: Case 2	1.0968	0.7672	1.4296
3D horizontal undulating baseline case	0.9170	0.6894	1.3301

TABLE 3.3: Cycle average lift coefficient and drag coefficient at 2D, 3D static, and 3D horizontal moving.

3.7 Conclusions

In this chapter, we numerically investigate the 3D flying-snake-inspired horizontal undulating locomotion during aerial gliding. The geometry of the snake model is reconstructed based on the realistic cross-sectional shape of a snake body, and the motion of the undulation based on the mathematical equation is applied to the model. The main focus of this paper is to examine the force generation mechanism with such motion and the three-dimensional vortex dynamics. Various parameters that would lead to the change of lift force generation on the body have been studied, including the angle of attack (AOA), undulation frequency, and the Reynolds number (Re).

The undulation motion is symmetric based on the prescribed equation, which brings a symmetric lift coefficient history. Thus, the L-R and R-L strokes can be treated equally. On each stroke, the lift contour map showed evidence that the high lift region passes both downwards the body and along with time. This time-evolution process of lift generation is formed due to the introduction of horizontal undulation. The high lift areas are mostly located at the curved portion of the body, which is different from the previous finding that without any motion, the lift generates more on straight parts of the static models. This lift distribution may indicate the fact that undulation improves the rolling stability of the flying snake while gliding by providing torque on lateral sides.

The horizontal undulation creates a series of major vortex structures, including Leading Edge Vortex (LEV) and Trailing Edge Vortex (TEV) on the snake model during the gliding. In each stroke, there is a prominent peak and trough which is universally observed no matter how the flow parameters vary. Detailed vortex dynamics analysis reveals that the formation and development of the LEV on the dorsal surface of the snake body plays an important role in producing lift. Another noticeable feature is that at $t/T = 0.34$, the lift generation over the body reaches its peak. This is caused by the LEV2 generated at the anterior body, raising the instantaneous lift by 30%.

Further analysis with respect to different AOAs shows that the overall cycle-averaged lift reaches its peak value at 45°, which possesses a similar pattern as the previous 2D study with a 10° peak shift. The cycle-averaged lift coefficient at 45° AOA is 4.8% higher than at 35°. The increase of stall AOA (delayed stall) is caused by the 3D body effect and the presence of spanwise flow. The strength and the stability of LEV changing with AOA are the key reasons to explain the change in force production. Furthermore, the coincidence between lift-to-drag ratio and cotangent AOA at higher degrees ($> 30°$) shows that equilibrium status can be more easily reached since the resultant force is used to balance the gravity (vertical to snake plane). Similarly, the increase of LEV strength in the Reynolds number effect can also explain the overall lift generation increases with the Re.

The effect of undulation frequency is reflected in changing the local body speed, which will affect the vortex formation near the snake body. The overall cycle-averaged lift generation reaches the peak at $f = 1.143$. At higher frequencies, LEV2 is more difficult to generate on the anterior body. However, the lift loss due to the insufficiently developed LEV2 at higher frequencies will be partly compensated by the lift concentration on the curved portion body. Thus, the average lift C_L at $f = 2.000$ is reduced by only 3.35% compared with C_L at $f = 1.143$. Another feature noticeable is that there is more lift concentrated on the head at a higher frequency, which might indicate the snake's ability to generate higher pitching torque. These findings are expected to extend the understanding of horizontally undulating motion in flying snake aerial gliding and to provide some fundamental knowledge for the optimal design of gliding snake robots.

4 Effect of vertical bending undulation

In this section, the simulation results for the vertical-undulating model are presented. The main purpose of this study is to thoroughly explore the effects of vertical bending on the gliding aerodynamics displayed in the aerial undulation of flying snakes. Furthermore, to understand the flow mechanisms of lift production and gliding efficiency. The wake structure and flow around the snake are visualized with a direct-numerical simulation (DNS) computational fluid dynamics (CFD) solver. An in-depth exploration is undertaken to evaluate the varying effectiveness achieved through different vertical bending methods, including the vertical wave undulation and the dorsal-ventral bending. In Section 4.1, we will examine the aerodynamic performance of the baseline case, along with the vortex structures that lead to the change in performance. In Section 4.2, we will compare different vertical wave undulation amplitudes. In Section 4.3, we will conduct a parametric study to investigate the effects of dorsal-ventral bending with varying amplitudes.And the conclusions are summarized in Section 4.4.

4.1 Baseline case

Figure 4.1 (a) plots the instantaneous force coefficients of the baseline case from one steady undulating cycle. Clear symmetry in force productions can be observed as the vertical undulation motion is included, which is similar to our previous work on the pure horizontal motion [10]. From figure 4.1 (a), a peak lift production can be found at $t/T = 0.41$ in its right-to-left (R–L) stroke, rising from a global trough at $t/T = 0.21$. The drag generation shares a similar trend as lift production, despite that its trough and peak time around $0.02T$ ahead of the lift. In addition, it is worth mentioning that the change in drag production over a cycle is lower than that in lift production, implying the undulatory motion relates closely to the lift production.

The instantaneous 3D wake structures of the flying snake in the R–L motion are visualized through the iso-surface of Q-criterion [74]. Figure 4.1 (b) – (e) plot these flow features at different time instants at $t/T = 0.0, 0.21$ (global trough lift production), 0.41 (global peak lift production) and 0.50 to show the vortex development corresponding to the lift generation. The process will be repeated for the second half of the cycle since the motion is symmetric.

From figure 4.1 (b), a pair of vortex tubes of LEV and TEV (denoted as LEV_1 and TEV_1) have been generated near the leading edge and the trailing edge of the anterior body at the early stage of vortex generation at $t/T = 0.0$. It can be observed that the LEV is of higher strength than the TEV, such that the lift production is higher than the drag generation as shown in figure 5 (a). The LEV is shown to be attached to the snake's head as it crosses through the incoming flow, and it is shed as it proceeds further into the motion cycle. Figure 4.1 (c) shows the near-body vortex dynamics at $t/T = 0.21$, where a LEV detachment can be observed, while the head portion generates a lower strength LEV compared to the previous time instant at $t/T = 0.0$. The lowered LEV formation suggests a lower lift production at the time instant, which corresponds to the lift trough shown in figure 4.1 (a). As mentioned previously, the lift peaks at $t/T = 0.41$ rising from the lift curve trough, and the corresponding vortex topology is shown in figure 4.1

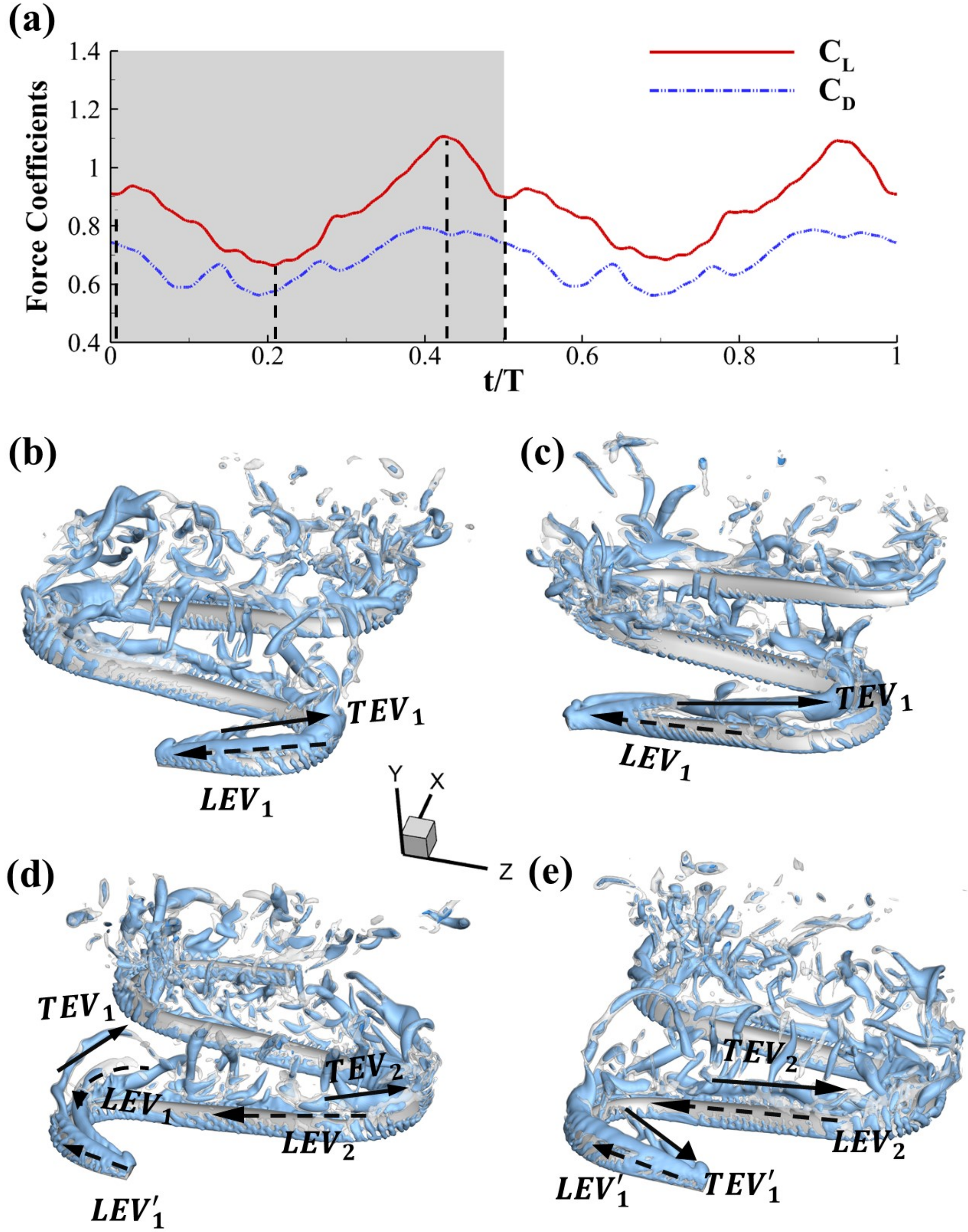

FIGURE 4.1: (a) The instantaneous force coefficients as a function of time in one undulatory cycle. The right-to-left (R–L) motion is shown in grey. 3D wake structures of the flying snake model in the R–L stroke at (b) $t/T = 0.00$, (c) $t/T = 0.21$, (d) $t/T = 0.41$, and (e) $t/T = 0.50$ are presented in perspective view, respectively. The wake structures are visualized by Q-criterion at a value Q = 800 (in transparent white) and at 1200 (in blue). The solid arrow indicates the directions of trailing-edge vortex tubes (TEV), and the dashed line arrow indicates the directions of leading-edge vortex tubes (LEV).

(d). The previous pair of LEV and TEV is now denoted as LEV_2 and TEV_2, and they begin to form and gradually increase until they reach their peak value, as shown in Figure 5(d). Then the pair of vortex tubes begin to shed from the anterior body which is located at the symmetric position as the initial time. At $t/T = 0.50$ as shown in Figure 4.1 (e), the newly formed vortex tube pair is denoted as LEV_1' and TEV_1'.

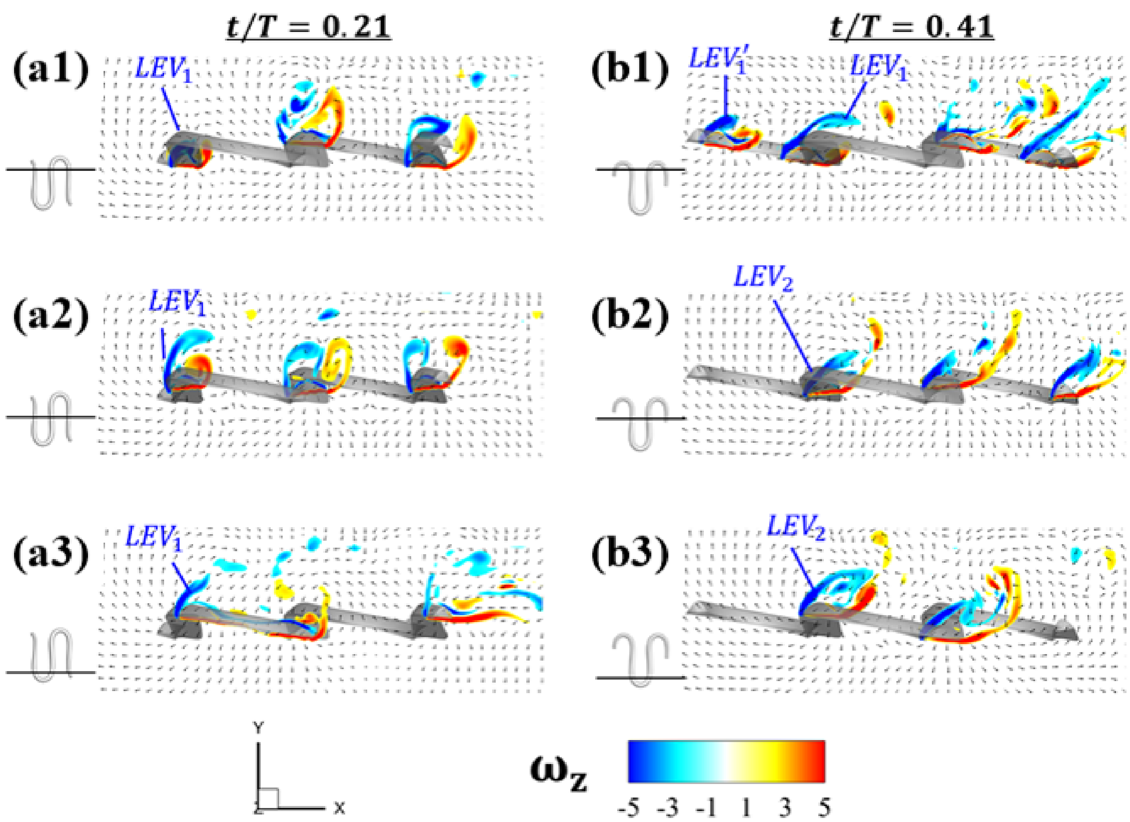

FIGURE 4.2: (a) The instantaneous lift coefficient history during one undulatory cycle. The same figure is referenced twice for emphasis. (b) and (c) represent the vortex structure at $t/T = 0.21$ and $t/T = 0.41$, respectively. (1) – (3) corresponds to the XOY plane slice cut at $z/c = -3$, 0, and 3, respectively. The spanwise vorticity contour is presented with the legend listed below.

To capture the vortex formation in detail, the slice-cuts of the vorticity contours located at the XOY planes (whose location is $z/c = -3$, 0, and $+3$, respectively, with $z/c = 0$ meaning the slice-cut is located at the center of mass in the Z direction) were presented in Figure 4.2. The locations where the slices were made are indicated in the schematics to the left of each slice-cut. The trough and peak lift production timeframes have been chosen ($t/T = 0.21$ and 0.41) for comparison. At $t/T = 0.21$, which corresponds with Figure 4.2 (a1) to (a3), LEV_1 can be identified. The slice at $z/c = -3$ (Figure 6(a1)) shows a small LEV_1, whereas the slice-cut at $z/c = 0$ shows a developed LEV_1 at the straight part of the body. The slice-cut at $z/c = +3$ shows a strong LEV_1 formation at the U-turn of the body, while the drag-producing TEV has low strength. At a later time instant, $t/T = 0.41$, the head has made the U-turn and formed a new leading-edge vortex noted as LEV'_1 in Figure 4.2 (b1). Meanwhile, LEV_1 has been developed yet still remains attached to the surface. While at the slice-cut at $z/c = 3$ (Figure 4.2 (b3)), the new LEV has been formed, which is noted as LEV_2. The attachment of LEVs throughout the body sections among all slice-cuts results in higher lift production at this time instant.

The overall vortex generation shares a similar pattern as in previous work done by Gong et al. [10]. However, due to the existence of vertical wave undulation, there is still some slight difference in the vortex formation process caused by the kinematics change. Comparing with pure horizontal undulation, the introduction of vertical wave undulation changes the local pitch angle. The straight body makes the cross-section pitch forward and leads to a smaller effective angle of attack (eAOA). The reduction of eAOA weakens the LEV vortex formation and reduces the lift production.

4.2 Effect of the vertical wave undulation

In this section, we will discuss how the amplitude of vertical wave undulation affects the aerodynamic performance and vortex structures of flying snakes during gliding.

4.2.1 Aerodynamic performance

In Figure 4.3, the cycle-averaged aerodynamic performances are presented as a function of the vertical wave undulation amplitude ψ_m. Figure 4.3(a) gives the general trend of cycle-average force performance change, including lift and drag coefficient $\bar{C_L}$ and $\bar{C_D}$. It was found that the lift performance reaches a peak at $\psi_m = 2.5°$ and the $\bar{C_L}$ is 11.3% compared with our baseline case ($\psi_m = 10°$). Even compared with the pure horizontal case ($\psi_m = 0°$), the optimal $\bar{C_L}$ case ($\psi_m = 2.5°$) is also 1.5% higher. The general trend of $\bar{C_L}$ after $\psi_m = 2.5°$ is decreasing with the increase of amplitudes. Meanwhile, $\bar{C_D}$ reaches the peak value at $\psi_m = 2.5°$ and shares the same changing trend as $\bar{C_L}$.

Figure 4.3(a) also shows the change in cycle-averaged power consumption. From the results, it is shown that the C_{PW} shows the same trend as the C_L. It reaches a peak when it increases to $\psi_m = 2.5°$, which is 0.7% higher than the pure horizontal case ($\psi_m = 0°$) and 8.7% higher than the baseline case ($\psi_m = 10°$). The general trend is synchronized with the lift coefficient and can be explained with the force production. When experiencing larger force on the body, to maintain the same undulatory locomotion, the snake tends to consume more energy during gliding.

Figure 4.3(b) shows efficiency ratios including the lift-to-drag ratio L/D, lift-power ratio C_L/C_{PW} and drag-power ratio C_D/C_{PW} which is defined as in chapter 2.5. It was found that the lift performance reaches a peak at $\psi_m = 2.5°$ and the maximum L/D shows up at $\psi_m = 5°$. Compared with our baseline case $\psi_m = 10°$, the C_L increases 11.3% at peak value and L/D increases 4.3%. However, compared with the pure horizontal case ($\psi_m = 0°$), a small ψ_m will slightly

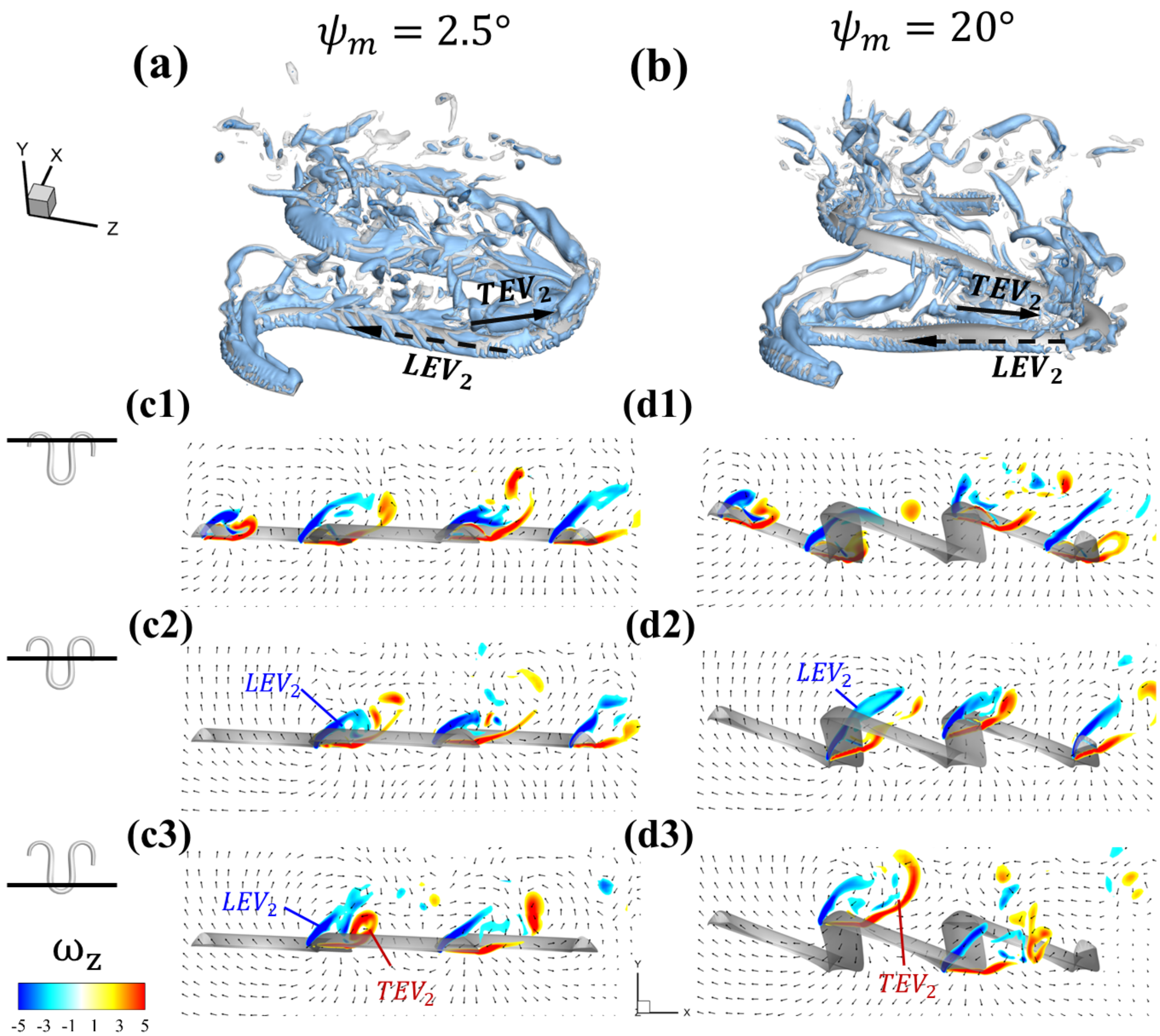

FIGURE 4.3: Cycle-averaged aerodynamic performance of the snake model with different vertical wave undulation amplitudes (ψ_m). (a) Lift, drag, and power coefficients; (b) Lift-to-drag ratio, lift-power ratio, and drag-power ratio.

increase the performance by 1.5% for C_L and 4.8% for L/D. When ψ_m increases beyond 5°, the trend of the performance decreases at higher amplitudes. From the figure, it is observed that C_L/C_{PW} has the same trend as L/D. It reaches peak value at $\psi_m = 5°$, which is 1.2% higher than the pure horizontal case ($\psi_m = 0°$) and 2.8% higher than the baseline case ($\psi_m = 10°$). On the contrary, C_D/C_{PW} follows the reverse trend as C_L/C_{PW}. It reaches its minimum value at $\psi_m = 5°$, which is 3.4% lower than the pure horizontal case ($\psi_m = 0°$) and 1.4% lower than the baseline case ($\psi_m = 10°$). However, when it passes 10°, the C_D/C_{PW} keeps descending. In general, smaller vertical wave undulation amplitudes (2.5° to 5°) increase the cycle-averaged aerodynamic performance, while at large amplitudes ($> 10°$) will decrease the performance.

In Figure 4.4(a), the lift coefficient history of one steady undulating period with different ψ_m is shown. Despite the similarity of force production trend, the significant difference occurs at $t/T = 0.41$ when lift reaches peak value. We subtracted the trough (at $t/T = 0.21$) and the peak (at $t/T = 0.41$) value of lift production in Table 4.1. For comparison, the $C_L(t/T = 0.41)$ value of $\psi_m = 2.5°$ is 15.8% higher than that of $\psi_m = 10°$ and 51.1% higher than that of $\psi_m = 20°$. On the contrary, the trough value of $C_L(t/T = 0.21)$ of $\psi_m = 2.5°$ is only 17.3% and 24.1% higher than that of $\psi_m = 10°$ and 20°. The dramatic difference in the peak value indicates that the vortex structures near the snake body will be the most different at $t/T = 0.41$, which will be chosen as the key frame in our later discussion.

ψ_m (°)	C_L Trough ($t/T = 0.21$)	Peak ($t/T = 0.41$)
2.5	0.8035	1.2771
10	0.6851	1.1028
20	0.6477	0.8452

TABLE 4.1: Instantaneous lift coefficient at peak and trough value for different vertical wave undulation amplitudes at 2.5°, 10°, and 20°.

In Figure 4.4 (b) and (c), the instantaneous drag and power coefficients are presented. With the same trend as lift, they also show maximum difference at $t/T = 0.41$. More detailed explanations for this phenomenon are provided in the following sections, and the vortex dynamics are interpreted in an effort to understand the mechanism for the performance difference.

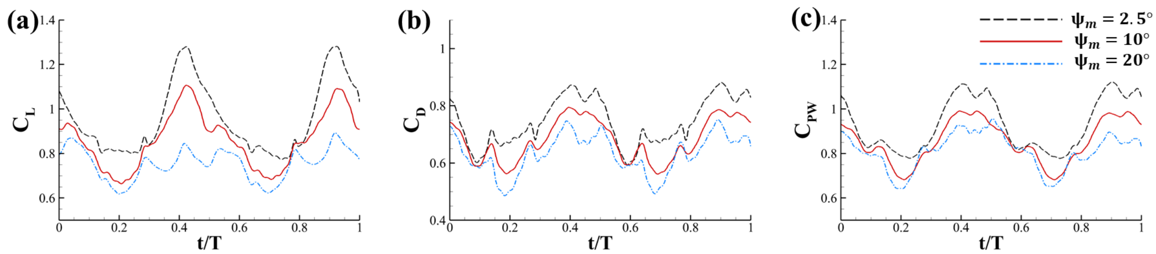

FIGURE 4.4: Instantaneous aerodynamic performance of the snake model with different vertical wave undulation amplitudes ψ_m at 2.5°, 10°, and 20° over one undulatory cycle. (a) Lift coefficients; (b) Drag coefficients; (c) Power coefficient.

4.2.2 Surface Pressure and Force Distribution

Figure 4.5 (a) shows the local lift distribution along the body at the key frame ($t/T = 0.41$) to analyze the high and low force regions on the body. From the curve, we observe that the 10% to 25%, 45% to 60%, and 80% to 100% portions along the body tend to provide a similar amount of lift for different ψ_m. The significant difference occurs between the 25% to 45% and 60% to 80% regions where the local peak value has been reduced by 200% ($C_{L_{\text{local}}}(\psi_m = 2.5°) = 0.06$ vs $C_{L_{\text{local}}}(\psi_m = 20°) = 0.02$). This indicates a large portion of lift loss in these two regions.

Correspondingly, in Figure 4.5 (b) – (d), the contours of pressure coefficient difference ΔC_P between the top and bottom surfaces are presented for different ψ_m. It's observed that the lift loss region is located in the straight portion of the body. The red zone of the lift generation becomes shallower as the ψ_m increases, while the force production near the curved portion of the body remains high. This lift loss contributes to the decrease of the lift coefficient for the overall performance, and the fact that the force difference occurs on the straight portion of the body may indicate that they share the same mechanism in vortex generation.

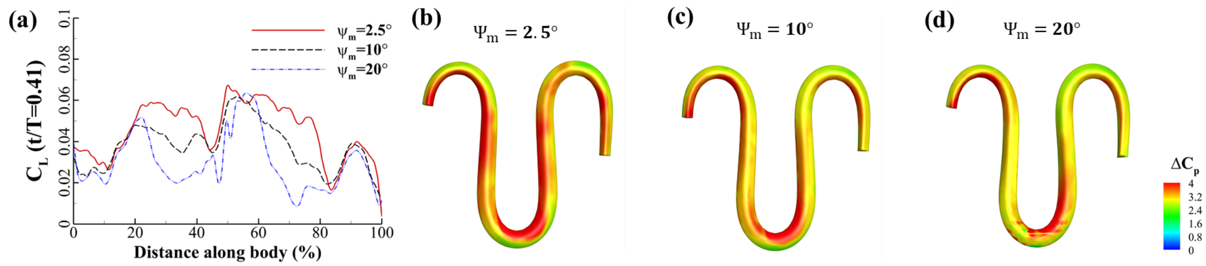

FIGURE 4.5: (a) Lift distribution along the body at $t/T = 0.41$ at different vertical wave undulation amplitudes ψ_m at 2.5°, 10° and 20°.; (b) – (d) ΔC_P contour on the surface of the snake model body at the different amplitudes, respectively.

It is worthy to note that the way a snake distributes its lift along the body may suggest a possible strategy for controlling its movements while gliding. Although undulating in a way that causes large vertical waves may result in a loss of lift and reduced efficiency, it has been observed in nature that undulatory motion can involve large vertical deformations. From the contours of the pressure force, it can be predicted that at higher ψ_m, more force will be concentrated on the lateral sides of the body, particularly in the case of a curved body, to create a larger force arm. This may be a way to balance the rolling force moment and stabilize the snake's posture while it is gliding through the air.

4.2.3 Vortex Dynamics and Flow Analysis

In this subsection, we will go into a detailed analysis of the effect of vertical wave undulation amplitudes. According to the previous discussion, we picked the key timeframe at $t/T = 0.41$ for detailed analysis to reveal the flow physics and flow change process for two different ψ_m.

Figure 4.6 shows the instantaneous vortex structure at $t/T = 0.41$ with different ψ_m of 2.5° and 20°, as well as the 2D span-wise vorticity at the slice-cuts located at the XOY planes (whose location is $z/c = -3$, 0, and $+3$, respectively). The vortex structure shows the same pattern as in Figure 4.1. From the perspective view of the wake structure in Figure 4.5 (a) and (b), vortices including leading-edge vortices (LEVs) and trailing-edge vortices (TEVs) can be seen generating on the snake body surface. The peak lift generation corresponds to the timeframe when the longest LEV tube is formed and attached to the leading edge of the snake body. This feature holds true when ψ_m increases.

Figures 4.6 (c1), (d1), and (c3), (d3) show the slice-cuts near the lateral edge of the body, which cut near the curved portion of the body. From Figure 8 we already know that the force maintains high in these regions. The 2D span-wise vorticity contour shows that the LEV_2 generated keeps attached to the leading edge of the body. The TEV_2 forms a pair on the trailing edge of the body and it brings a high-pressure region to the ventral surface of the body. The midplane slice-cut has been presented in Figure 4.6 (c2) and (d2). Due to the large amplitude vertical undulation, the cross-section of the snake experiences a large local pitch angle forward. Based on the previous study by Gong et al. [10], at smaller angles ($< 45°$), the lift production will decrease when the angle of attack (AOA) reduces. Here in the mid-part of the body, where the snake has a small curvature and straight body, the reduction of local AOA causes the weaker vortex formation. In Figure 4.6 (c2) LEV_2 remains attached to the body, while in Figure 4.6 (d2) LEV_2 has been shed off the leading edge. To sum up, the vortex formation is highly related to the effective angle of attack (eAOA), thus significantly impacting the lift generation in the near area. For $\psi_m = 2.5°$, the eAOA near the straight portion of the body is the optimal and brings maximum lift production. The lateral sides of the body are less affected by the local eAOA due to the body turning; the snake tends to keep the local pitch minimized to maintain a smooth transition.

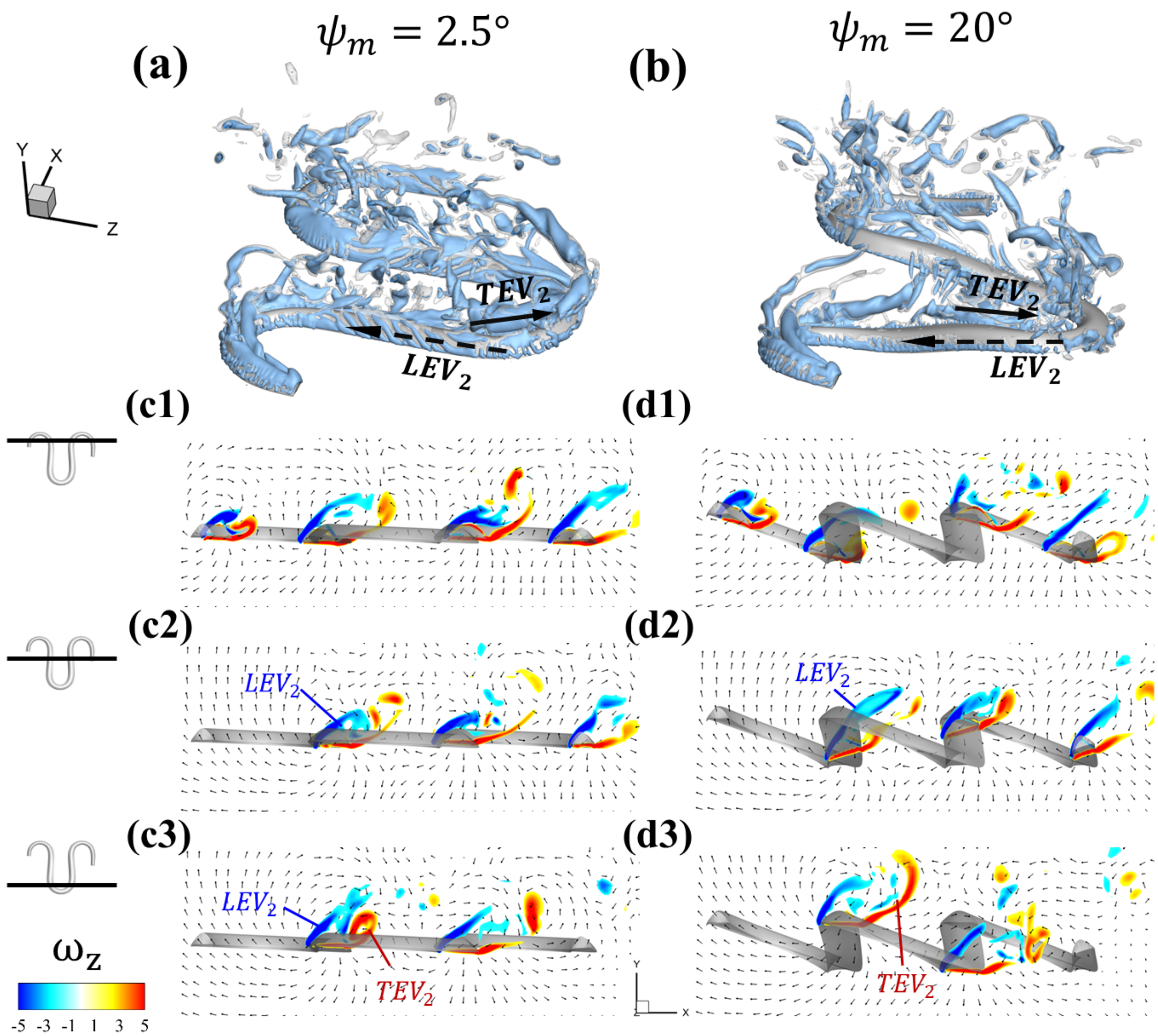

FIGURE 4.6: Comparison of instantaneous vortex structure at $t/T = 0.41$ with different bending amplitudes ψ_m of 2.5° and 20° for (a), (b) respectively. (c1)–(c3), (d1)–(d3) show the 2D spanwise vorticity contour (showing LEV1, LEV2, and TEV1, TEV2) on the anterior snake body at the corresponding time-frame. The XOY slice-cuts are located at $z/c = -3$, 0, 3 respectively.

To further illustrate the link between the vortex formation and the force production, we presented the slice-cuts of pressure contour at the XOY planes (at locations $z/c = -3$, 0, and $+3$, respectively) in Figure 11. The pressure coefficient shown in the figures is defined as:

$$C_p = \frac{P - P_\infty}{0.5\rho U_\infty^2} \tag{4.1}$$

where P is the local pressure, P_∞ is the freestream pressure, ρ is the air density, and U_∞ is the freestream velocity.

For Figure 4.7, in all the (1) and (3) positions, which are located near the lateral edge of the body, the high-pressure zones (red) are preserved beneath the ventral surface of the snake while the low-pressure zones (blue) remain attached to the dorsal surface. This can be observed throughout the increment of ψ_m (Figure 4.7 (a-c)). However, in Figure 4.7 (a2), (b2), and (c2), the blue zones faint when ψ_m increases and the effective angle of attack (eAOA) decreases. A similar trend happens to the red zones. Compared to the enhanced high-pressure zone beneath the snake body at a low bending angle of $\psi_m = 2.5°$, the higher bending angles result in a scattered high-pressure region and therefore weak lift force. To sum up, the vortex formation is highly affected in the mid-plane of the body, and the LEV and TEV are weakened. Since the difference between the high- and low-pressure regions forms a pressure gradient on the body, it contributes to lift and drag as different components. When the pressure difference decreases with the increase of ψ_m, the lift production will drop.

4.3 Effect of the dorsal-ventral bending

Flying snakes apply vertical bending to adjust their gliding motion. Other than changing the maximum vertical bending amplitude, they may also apply dorsal-ventral bending motion as

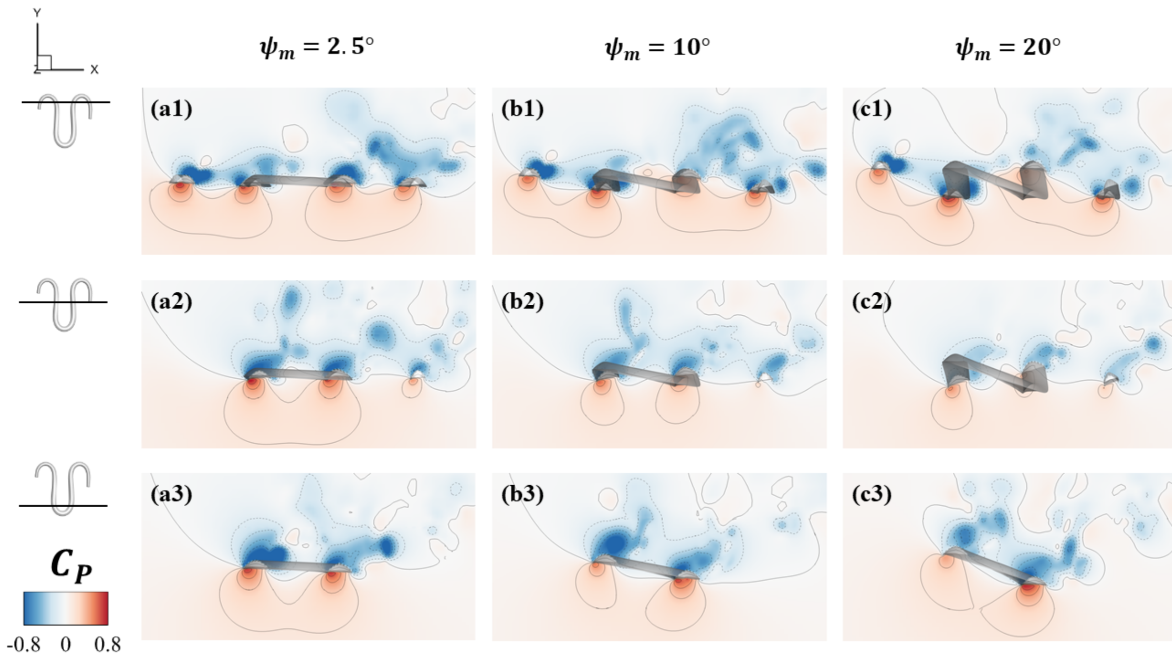

FIGURE 4.7: Comparison of instantaneous pressure contour at $t/T = 0.41$ with different vertical wave undulation amplitudes ψ_m of 2.5°, 10°, and 20° for (a), (b), and (c) respectively. (1), (2), and (3) represent the position of the XOY slice-cuts' location at $z/c = -3$, 0, 3.

an alternative way to achieve vertical deformation. Without a sinusoidal wave, this motion describes the vertical bending gradually from the head to the tail in a linear transition. This motion is often observed as the snake tends to maintain its head steady while its tail bends upwards or curls downwards. As described in equation (2), ψ_{DV} is the dorsal-ventral bending amplitude that we adopt to investigate the effect. $\psi_{DV} > 0°$ means tail down and $\psi_{DV} < 0°$ means tail up.

4.3.1 Aerodynamic performance

Figure 4.8 presents the change in cycle-averaged aerodynamic performances with dorsal-ventral bending amplitude ψ_{DV}. In Figure 4.8 (a) and (c), the lift, drag, and power coefficients follow a monotonically increasing trend within the range of ±5°. At $\psi_{DV} = 5°$, the lift production

C_L increases up to 1.02, equivalent to a 17.3% enhancement compared with the baseline case ($\psi_{DV} = 0°$). This value is larger than the optimal case when we modify the vertical wave undulation amplitude ψ_m. That means, with the tail bending downward, the snake tends to generate higher lift in a more efficient way. From the previous pressure contour, it can be predicted that a larger pressure difference will be imposed on the snake body, which generates higher lift. And to counter the lift, the snake will consume more power to maintain the undulatory motion. Further evidence will be provided in following sections.

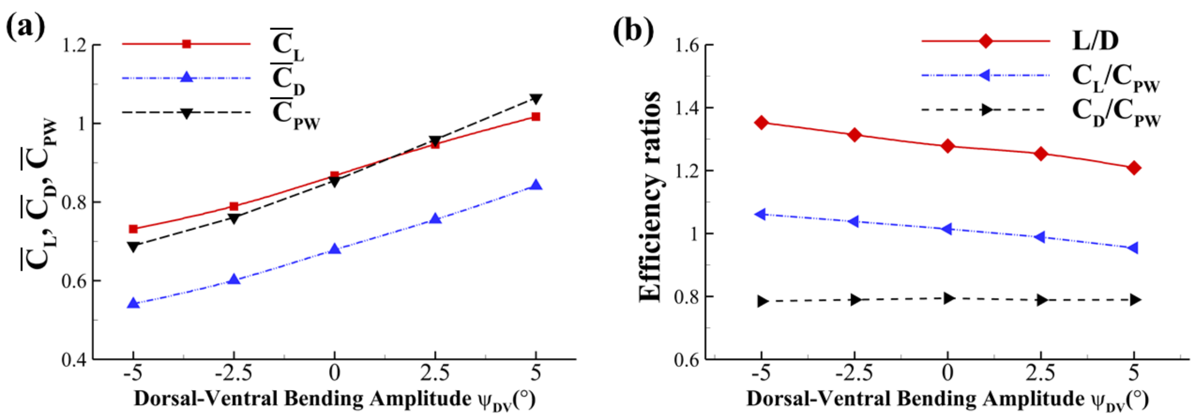

FIGURE 4.8: Cycle-averaged aerodynamic performance of the snake model with different dorsal-ventral bending amplitudes (ψ_{DV}). (a) Lift, drag, and power coefficients; (b) Lift-to-drag ratio, lift-power ratio, and drag-power ratio.

Figure 4.8 (b) and (d) describe the L/D and C_L/C_{PW} as monotonically decreasing with the increase of d_ψ. C_D/C_{PW} is less affected, and the variance among different data is less than 1.0%. This indicates that the tail-up motion is a more efficient posture during gliding, both experiencing smaller drag and consuming less power. At $\psi_{DV} = -5°$, $L/D = 1.35$ and it is 5.8% higher than the baseline case. C_L/C_{PW} also shows a 4.5% enhancement when we decrease ψ_{DV}. However, the lift production will reduce by 15.6% at the same time due to less overall force production.

Figure 4.9 shows the instantaneous aerodynamic performance during one cycle for different dorsal-ventral bending amplitudes. Unlike the change with ψ_m where significant difference only appears at some time periods, the increase/decrease of the performance scales at all time. That may indicate there exist a different mechanism that leads to the vortex formation change to the whole body, not restricted to a certain part.

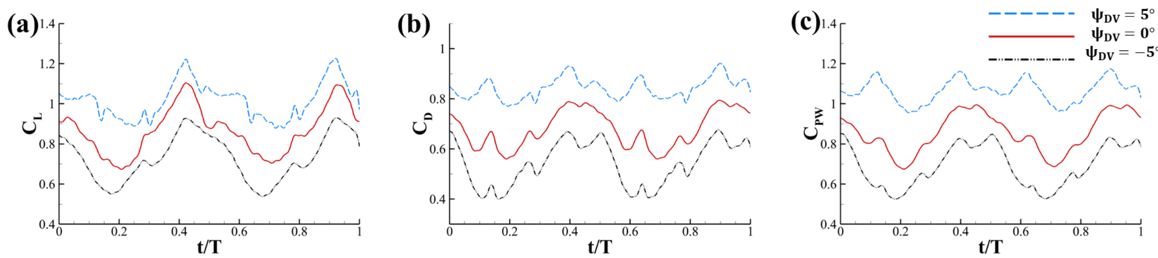

FIGURE 4.9: Instantaneous aerodynamic performance of the snake model with different dorsal-ventral bending amplitudes ψ_{DV} at 5°, 0° (baseline), and −5° over one undulatory cycle. (a) Lift coefficients; (b) Drag coefficients; (c) Power coefficient.

4.3.2 Vortex Dynamics and Flow Analysis

For the same key frame at $t/T = 0.41$, Figure 4.10 shows the instantaneous vortex structure and the 2D span-wise vorticity at the slice-cuts located at the XOY planes (same as in 3.2), with dorsal-ventral bending amplitudes of −5° and 5°. The general vortex structures appear to be similar to the baseline case in Figure 4.1. There is a difference in the distance between the vortex tubes and the snake surface due to the ascending or descending slope as shown in Figure 4.10. Figure 4.10(a) shows the vortex structure for the tail-up case, and Figure 4.10(b) shows that for the tail-down case. For the tail-up case, the LEV and TEV tubes appear to be closer to the surface of the body, which will result in a stronger effect on the body force. On the other hand, the tail-down case shows a more complex vortex structure, which may connect to the enhanced aerodynamic performance.

The spanwise vorticity contours provide a close-up view of the vortex formation. In Figures 4.10(c1)-(c3), the LEV and TEV shed off from the anterior body edges advect downstream. While it forms a pair for vortices shed after the anterior body as shown in 2D formation, which is similar to the wake after a bluffed body, the posterior body is located in the upstream flow. The cross-section interacts with the vortex pairs and affects the formation of the vortex. This body-wake interaction has been reported in 2D tandem flying snake cross-section interaction by Jafari et al. In Figures 4.10(d1) – (d3), considering the advection direction of the vortex street, the distance between the two wakes keeps far away from each other so that there will be less interaction between the body and the wake. Such wake-body interaction has been reported in many other researches. By shifting the distances between the body and the wake, the vortex breakdown switches from above the dorsal surface to the leading edge. As a result, the LEV and TEV distort and merge with the shear layer on the ventral surface.

To illustrate the body-wake interaction, we computed cycle-averaged local U velocity ($\bar{U} - U_\infty$) and pressure coefficient and presented the contours of the midplane slice-cut in Figure 4.11 for different ψ_{DV}. The blue color is defined as negative U velocity which represents a reversed flow after the wake. In the downstream wake, similar to the von-Karman vortex street, due to flow separation and interaction, the flow speed is usually smaller than the incoming flow. In Figure 4.11 (a1), the two wakes merge at $\psi_{DV} = -5°$. The posterior body is affected more than the anterior body due to the merge of LEV and the counteraction of TEV. From Figure 4.11 (b1), it is also clearly observed that there is only one high-pressure region below the anterior body. The high-pressure zone vanishes, and the low-pressure zone merges together yet with a fainted color as well. As previously analyzed, the decrease in pressure difference brings less lift component,

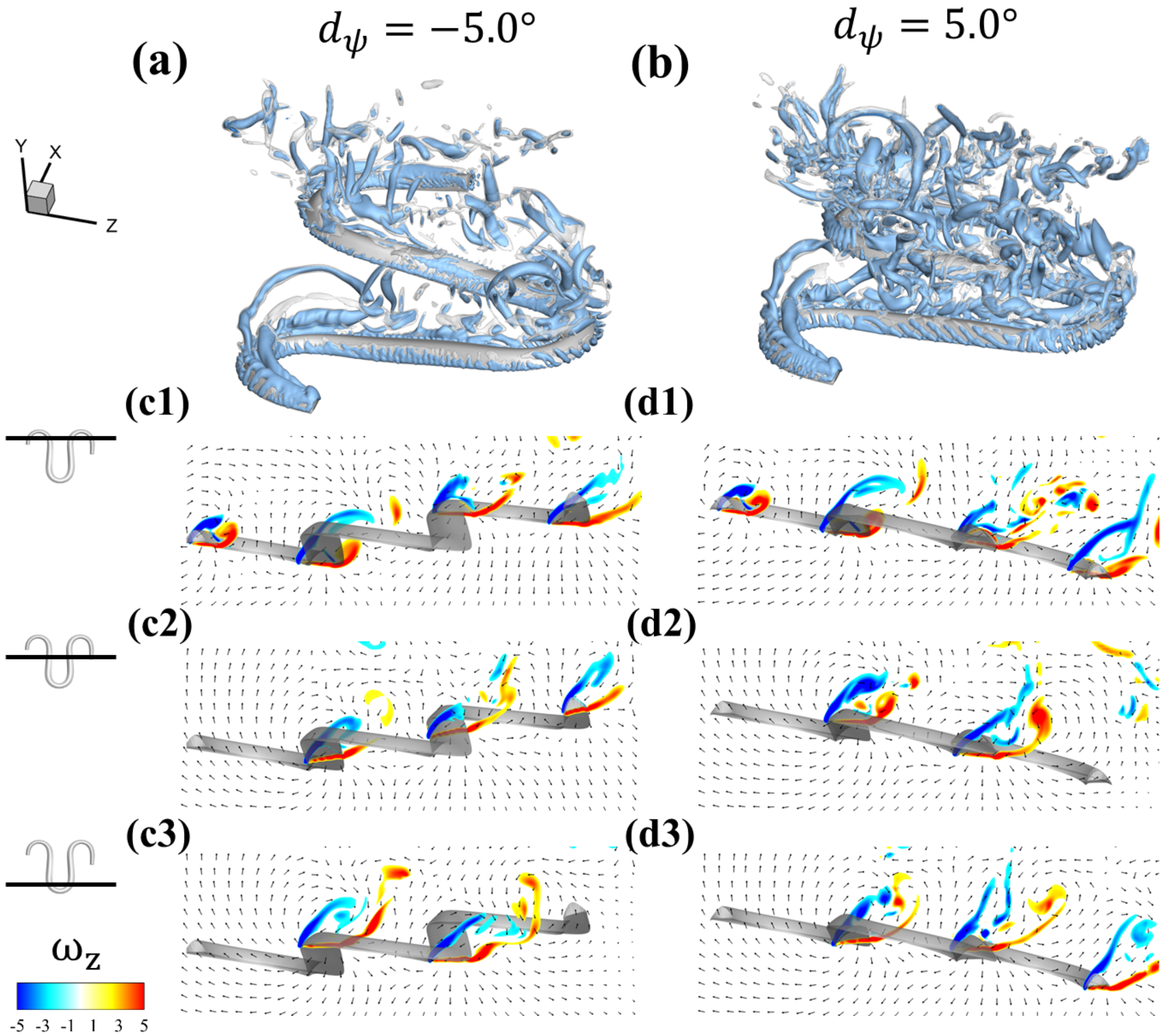

FIGURE 4.10: Comparison of instantaneous vortex structure at $t/T = 0.41$ with different bending amplitudes ψ_{DV} of $-5°$ and $5°$ for (a), (b) respectively. (c1)–(c3), (d1)–(d3) show the 2D spanwise vorticity contour (showing LEV1, LEV2, and TEV1, TEV2) on the anterior snake body at the corresponding time-frame. The XOY slice-cuts are located at $z/c = -3$, 0, 3 respectively.

especially for the posterior body. However, the force component parallel to the flow direction will decrease simultaneously, which represents smaller drag production on the body, leading to higher efficiency during gliding.

At $\psi_{DV} = +5°$, on the other hand, the distance between the wakes drift apart due to the dorsal-ventral bending downwards in Figure 4.11 (a3). Compared with the baseline ($\psi_{DV} = 0°$) and tail-up ($\psi_{DV} = -5°$) cases, the low-pressure regions enlarge and emerge together in Figure 4.11 (b3). The high-pressure regions below the anterior and posterior body also enhance and expand to the tail part of the body. A high-pressure difference brings higher lift generation to the overall body, which agrees with the increasing trend presented in Figure 12(a). At the same time, the drag force increases, which reduces the efficiency during gliding while consuming more energy during undulatory motion.

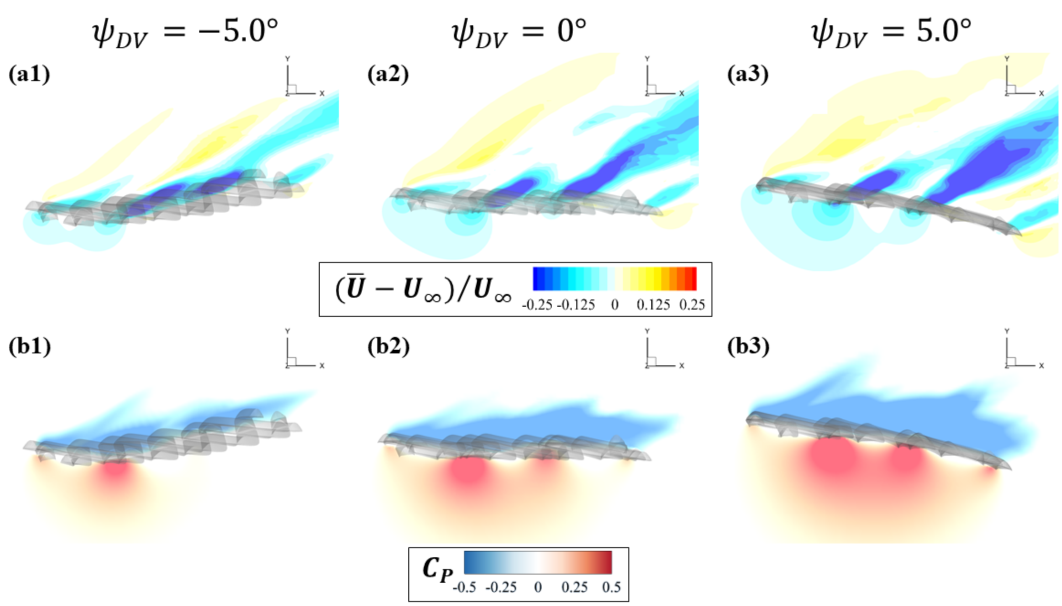

FIGURE 4.11: Comparison of cycle averaged (a) local U velocity pressure contour and (b) pressure contour with different dorsal-ventral bending amplitudes ψ_{DV} of (1) $-5°$, (2) $0°$, and (3) $5°$. The position of the XOY slice-cuts is at $z/c = 0$.

To further prove the body-wake interaction and the force generation, we presented the pressure coefficients contour on different slice-cuts in Figure 4.12 to validate its commonality over the body. The key frame is still chosen at $t/T = 0.41$. For $\psi_{DV} = -5°$, it has been clearly observed in Figure 4.12 (a1) and (a2) that the anterior body of the snake possesses a weaker high-pressure region and low-pressure region near the ventral and dorsal surface. However, due to the local vertical bending and the shape of the snake, in the slice-cut of Figure 4.12 (a3), the two cross-sections are relatively close so that the posterior body is no longer placed in the wake of the upstream flow. Therefore, the high-pressure zone still exists. For $\psi_{DV} = +5°$, the position of the bodies is aligned in the descending slope, thus minimizing the interaction between the wake and the bodies. The high-pressure regions near the ventral surface of the bodies are enhanced, leading to larger lift production.

In this section, the simulation results for the undulating model with static motion, pure horizontal undulation as well as vertical undulation combined at different rolling angles are presented. In previous studies, one important aerodynamic feature of the flying snake is the rolling stability. In Yeaton et al.'s[30], it was mentioned that the snake undulation enhances its rotational stability thereby increasing glide performance. In their simplified simulation, for short glides with launch heights of 10 m, 94% of glides with undulation were stable, whereas only 50% of glides without undulation were stable. Among the observed body shapes, all glides with undulation were stable, whereas only 35% of glides without undulation were stable.

However, they didn't extend this study with the aircraft dynamic study of the flying snake. With the CFD simulation, We will examine the rolling moments of the different cases, along with the vortex structures that lead to the change in performance. We will also evaluate how the

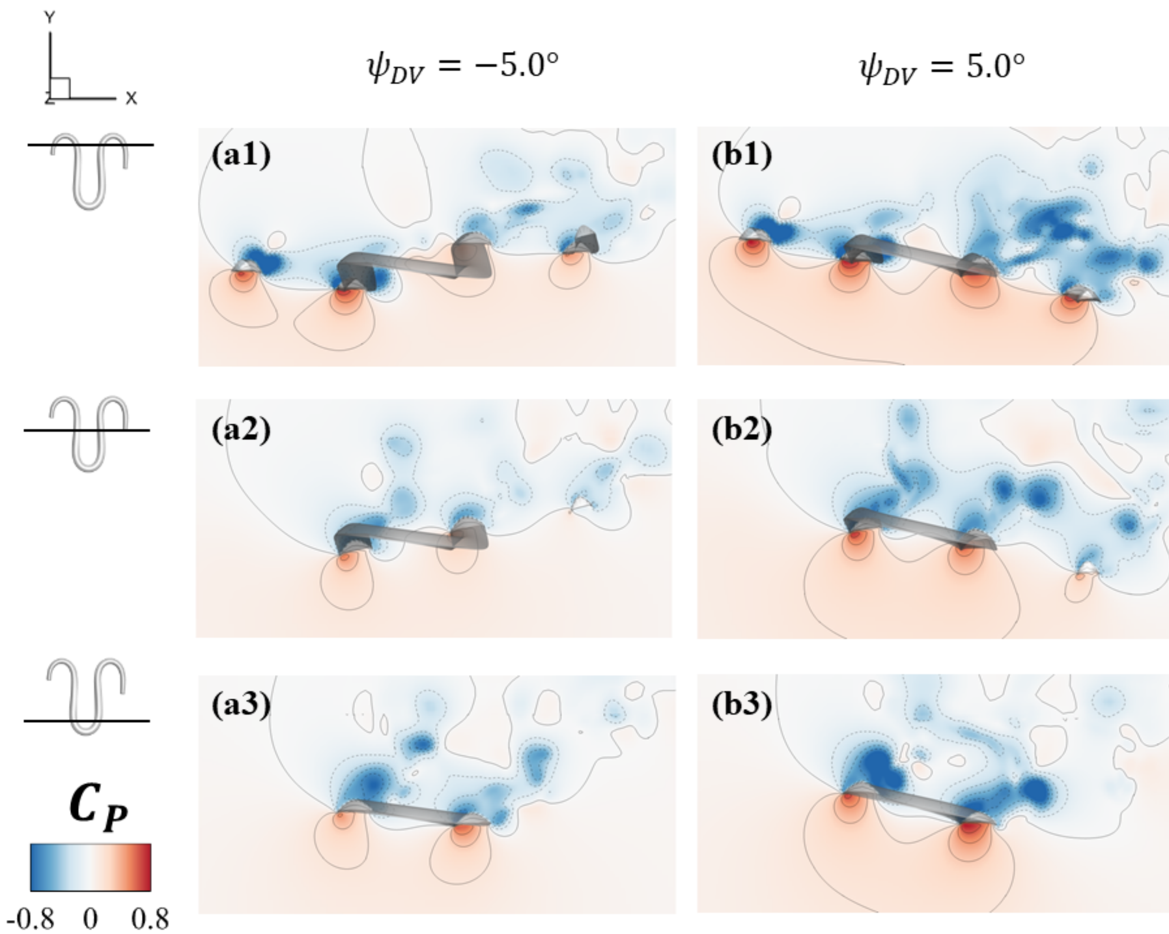

FIGURE 4.12: Comparison of instantaneous pressure contour at $t/T = 0.41$ with different bending amplitudes ψ_{DV} of $-5°$, and $5°$ for (a) and (b), respectively. (1), (2), and (3) represent the position of the XOY slice-cuts' location at $z/c = -3$, 0, $+3$.

horizontal undulation and the vertical wave undulation affects the stability of the flying snake.

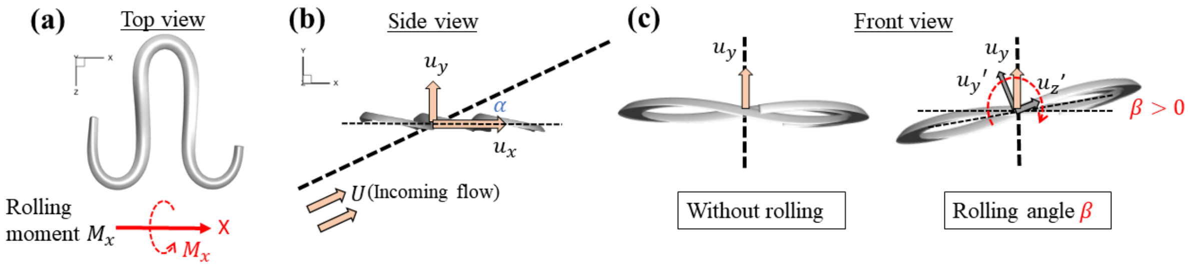

FIGURE 4.13: Schematic of the rolling motion of the gliding snake in (a)top view, (b)side view and (c)front view.

4.4 Rolling motion of the flying snake

4.4.1 The definition of rolling moment and rolling stability

The definition of rolling in flying snake gliding is applied from the aircraft flight[75]. Figure 4.13 shows the schematic of the snake gliding definition with the three-axis views. Figure 4.13 (a) illustrates the rolling motion of the gliding snake model which is rotating along the X axis.

$$T_x = \frac{\sum_N f_x l_x}{\frac{1}{2}\rho U_\infty^2 c^2} \tag{4.2}$$

The rolling moment is then defined as M_X in equation 4.2. In Figure 4.13 (b), while the snake is gliding, the model is travelling in the negative X direction and falling down in the negative Y direction. Therefore the relative speed U is decomposed into X and Y component U_x and U_y with the angle of attack (AOA) α.

In the context of aerodynamics, static stability in an aircraft is a measure of its ability to restore equilibrium after a minor perturbation, whereas dynamic stability refers to the motions an aircraft goes through as it returns to its original state of equilibrium following a disturbance [76], [77]. Specifically, longitudinal static stability, which ensures the aircraft returns to its initial angle of attack after being disturbed, is characterized by a negative derivative of the pitching moment coefficient with respect to the angle of attack. This is mathematically represented as

$$\frac{dM_Z}{d\alpha} < 0 \tag{4.3}$$

For subsonic aircraft, this relationship is often directly related to the derivative of the pitching moment coefficient with respect to the lift coefficient due to the linear relationship between angle of attack and lift coefficient governed by the lift curve slope. It can be expressed as

$$\frac{dM_Z}{dC_L} < 0 \tag{4.4}$$

Analogously, the criterion for rolling static stability, which determines the aircraft's natural tendency to level out from a rolling motion, is given by the following condition where C_l is the rolling moment coefficient and β is the rolling angle:

$$\frac{dM_X}{d\beta} > 0 \tag{4.5}$$

In the previous study, we investigated the effect of angle of attack α , which can be treated as a basic discussion about the longitudinal control.In this chapter, we will focus on the rolling stability as the extended dimension of the flying snake's gliding control. Now the flying snake with steady gliding will experience a span-wise flow U_z in the XOY plane and the rolling moment (M_X).

In the aircraft stability theory, positive static stability in an aircraft, especially concerning rolling stability, is characterized by the aircraft's natural realignment to its original trimmed attitude following an leftward or rightward rolling caused by external perturbations. Similarly, neutral static stability is observed in aircraft that do not exhibit a significant intrinsic tendency to revert to their initial trimmed state after experiencing a disturbance in their longitudinal configuration while the negative static stability is indicative of an aircraft's propensity to diverge further from its initial state when subject to disturbances, exacerbating rather than dampening the deviation from its trimmed neutral position.

4.4.2 Rolling performance of steady snake

Aerodynamic performance

In Figure 4.14, the force history over one steady undulating cycle is depicted for the updated case with a slight rolling angle introduced. The aerodynamic analysis of the flying snake-like model with imposed rolling reveals insights similar to the horizontal study, exhibiting two distinctive peaks in lift production during each undulating cycle. With a positive rolling angle, the lift production in the left-to-right (L-R) stroke manifests a smaller peak, while the right-to-left (R-L) stroke shows a larger one. In the case of drag coefficients, a consistent trend is observed, with an increased drag coefficient notably at $\gamma = -5°$. The rolling moment coefficient is characterized by two symmetric peaks of opposite signs, corresponding to each stroke. At a non-dimensional time $t/T = 0.05$, a smaller peak is observed to the left, and at $t/T = 0.44$, a larger peak to the right is evident, elucidating the dynamic rolling behavior of the model during aerial undulation.

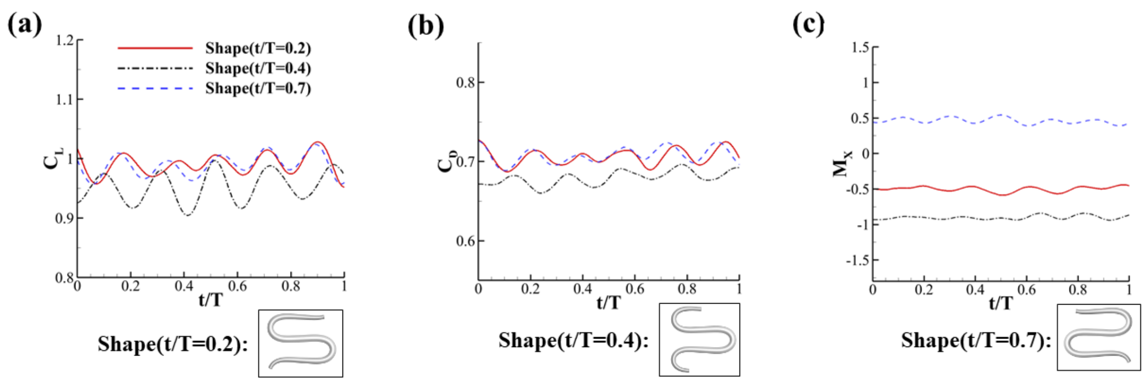

FIGURE 4.14: The instantaneous force coefficients for different static shapes (shape at t/T=0.2, 0.4 and 0.7) in one time unit. (a) Lift Coefficient. (b) Drag Coefficient (c) Rolling Moment Coefficient.

The cycle-averaged aerodynamic performance is presented in table 4.14.In the given data, the lift coefficient C_L remains relatively stable across varying yaw angles β, with a change rate of less than 0.3%, indicating a strong resistance to yaw-induced variations. The drag coefficient C_D, however, exhibits a slight increase, leading to a decrease in the lift-to-drag ratio L/D. Notably, the rolling moment coefficient M_x hovers around zero but reveals an increasing trend, suggesting a growing influence of yaw on the rolling stability as the yaw angle intensifies.

Vortex dynamics and related pressure

Figure 4.15 consists of three subfigures, (a) through (c), which compare different static shapes at nondimensional times $t/T = 0.2$, 0.4, and 0.7. The shapes at $t/T = 0.2$ and $t/T = 0.7$ are symmetric, leading to similar vortex formations. A comparative analysis of the peak and trough moment formation times reveals that the Leading Edge Vortex (LEV) detaches, producing less lift. This in turn contributes to a reduced rolling moment across the configurations. The superior intensity of LEV_1 over TEV_1 is evident, contributing to a higher lift than drag, as indicated in Fig.4.15(a1). This leading-edge vortex remains adhered to the snake's frontal region during its passage through the oncoming flow before eventually being shed as the cycle progresses. At trough time, depicted in Figure.4.15(a2), the dynamics of vortices close to the body reveal a detachment of the LEV, while the head generates a weaker LEV in comparison to the one at Figure.4.15(a1).

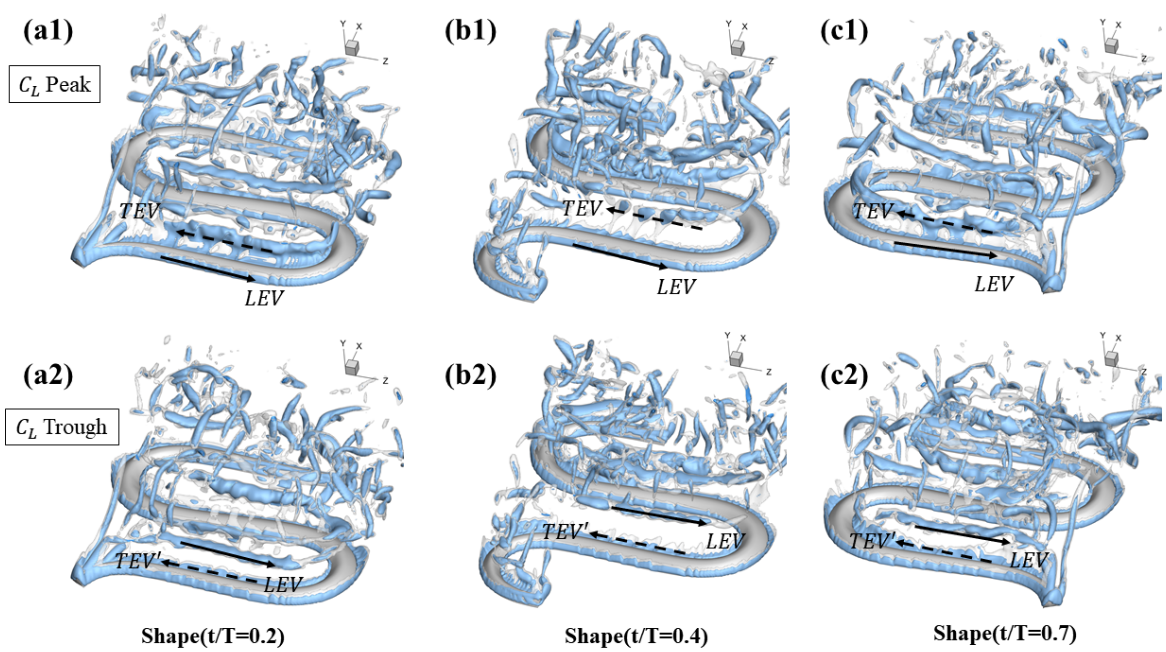

FIGURE 4.15: The vortex dynamics for (a) peak and (b) trough lift for different static shapes. The shapes are at (1) t/T=0.2, (2) t/T=0.4 and (3) t/T=0.7 .

Figure 4.16 presents three subfigures, (a) through (c), comparing the pressure contours of different static shapes at nondimensional times $t/T = 0.2$, 0.4, and 0.7, at corresponding slices. These pressure differences across the shapes significantly contribute to the rolling moment. Notably, the shape at $t/T = 0.4$ depicted in subfigure (b) demonstrates a more positive rolling moment relative to the other shapes. Accordingly, we compare the vortex formation based on this pressure contour.Figure4.17 includes two subfigures, (a) and (b), which compare the spanwise velocity and vortex structure at shapes corresponding to nondimensional times $t/T = 0.2$ and $t/T = 0.4$. The rolling angle associated with these shapes induces a larger spanwise flow and results in a stronger vortex, highlighting the dynamic changes in flow behavior due to alterations in the wing shape.

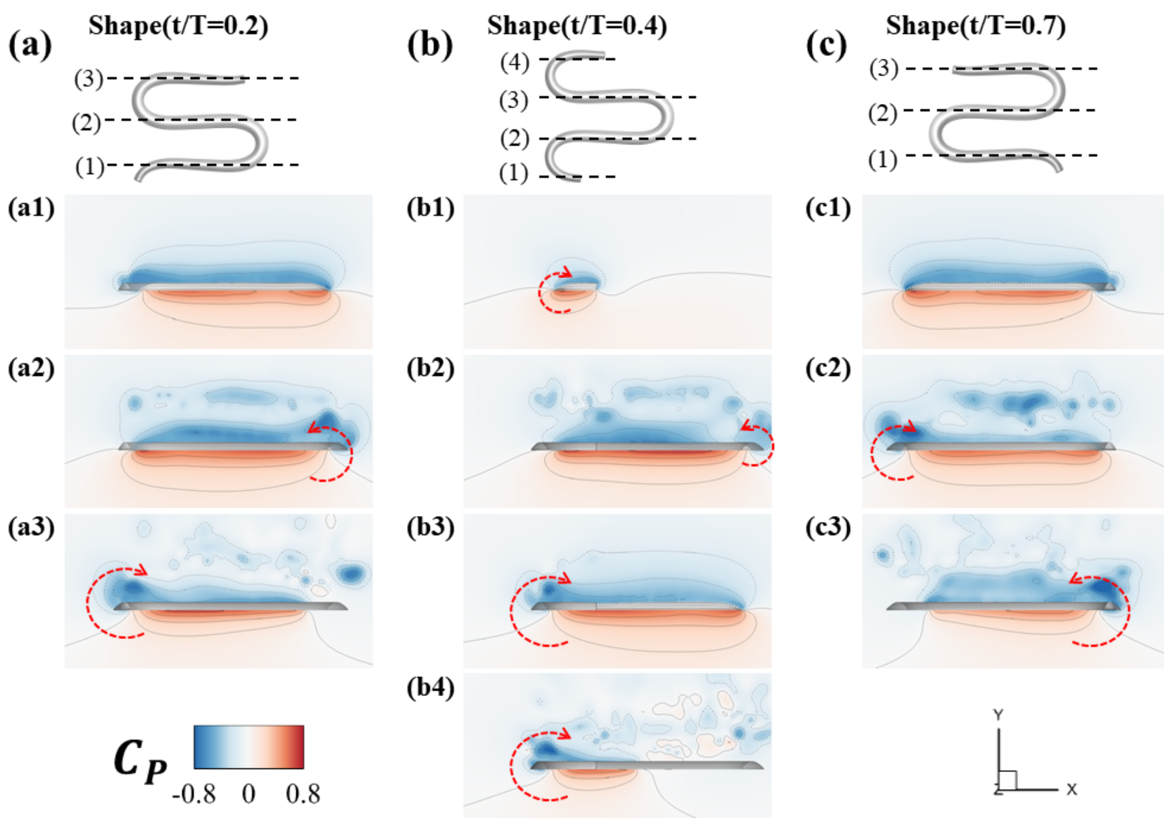

FIGURE 4.16: The pressure contour at different XOY planes for different static shapes. The shapes are at (a1) ~(a3) t/T=0.2, (b1) ~(b3) t/T=0.4 and (c1) ~(c4) t/T=0.7. The red dashed arrow indicates the local moment.

This vortex generation process bears resemblance to the patterns observed in previous research in chapter 3. Nonetheless, the introduction of vertical wave undulation introduces minor variances in the vortex development due to kinematic alterations. In contrast to purely horizontal undulation, vertical wave undulation modifies the local pitch angle, causing the body's cross-section to pitch forward and resulting in a diminished effective angle of attack (eAOA). This decrease in eAOA leads to weakened LEV vortex formation and diminished lift production.

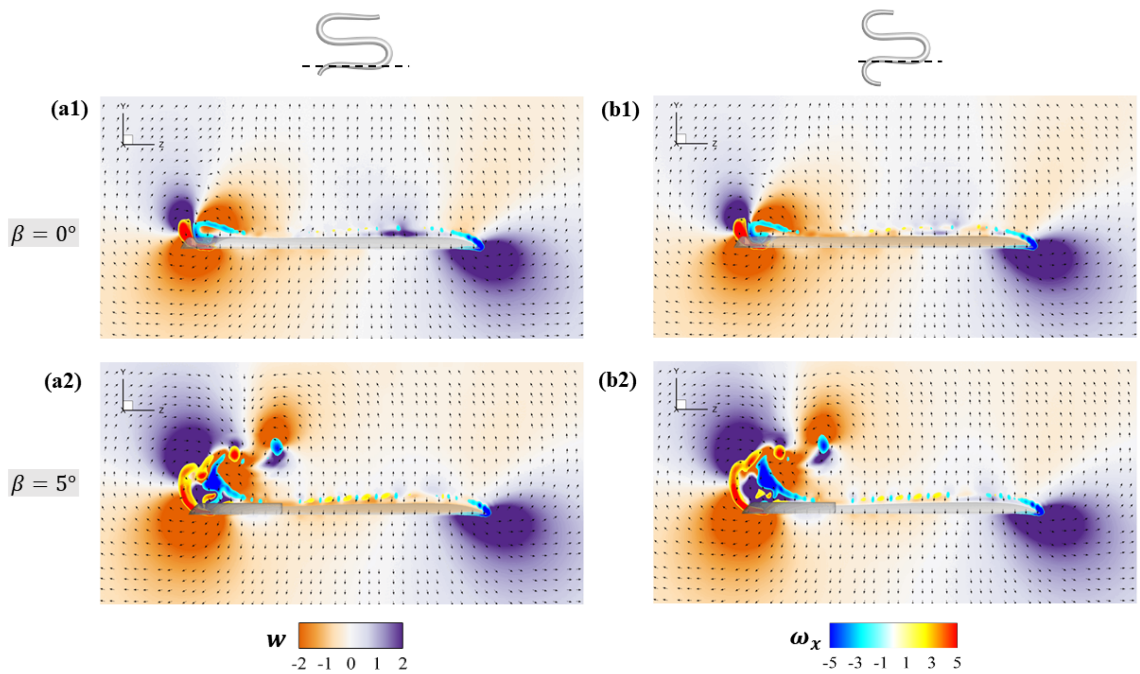

FIGURE 4.17: The instantaneous XOY plane vorticity ω_z and spanwise flow w (in Z direction) contour as in shape at (a)t/T=0.2, (b)t/T=0.4. Two different rolling angles (1)$\beta = 0°$ and (2)$\beta = 5°$is presented.

4.4.3 Effect of horizontal undulation in rolling

Aerodynamic performance

In Figure 4.18, the force history over one steady undulating cycle is depicted for the updated case with a slight rolling angle introduced. The aerodynamic analysis of the flying snake-like model with imposed rolling reveals insights similar to the horizontal study, exhibiting two distinctive peaks in lift production during each undulating cycle. With a positive rolling angle, the lift production in the left-to-right (L-R) stroke manifests a smaller peak, while the right-to-left (R-L) stroke shows a larger one. In the case of drag coefficients, a consistent trend is observed, with an increased drag coefficient notably at $\gamma = -5°$. The rolling moment coefficient is characterized by two symmetric peaks of opposite signs, corresponding to each stroke. At a non-dimensional time $t/T = 0.05$, a smaller peak is observed to the left, and at $t/T = 0.44$, a larger peak to the right is evident, elucidating the dynamic rolling behavior of the model during aerial undulation.

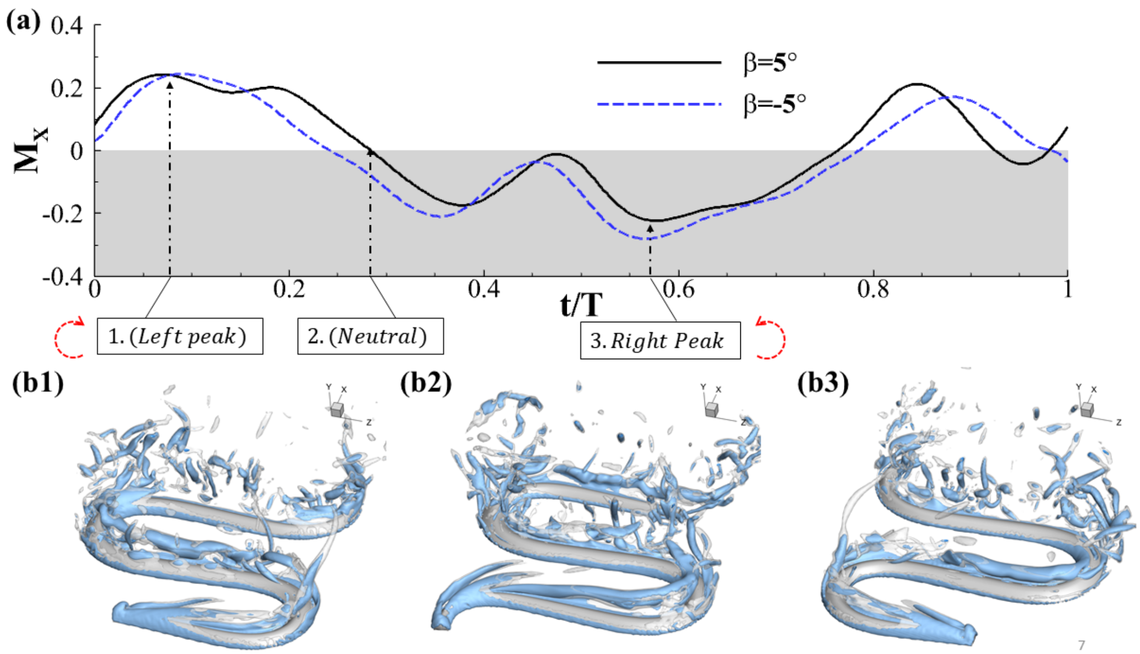

FIGURE 4.18: (a) Instantaneous rolling moment history in one cycle for horizontal undulation motion with two rolling angles. (b1)~(b3) vortex topology at left moment peak, neutral position and right peak for $\beta = 5°$ case.

β	-5°	-2.5°	0°	2.5°	5°
C_L	0.8644	0.8664	0.8643	0.8649	0.8668
C_D	0.6782	0.6807	0.6798	0.6800	0.6908
L/D	1.2746	1.2728	1.2714	1.2719	1.2548
$-M_x$	-0.0350	-0.0150	0.0123	0.0369	0.0855

TABLE 4.2: Aerodynamic Coefficients and Moment Results for Different Rolling Angles

The cycle-averaged aerodynamic performance is presented in table 4.2.In the given data, the lift coefficient C_L remains relatively stable across varying yaw angles β, with a change rate of less than 0.3%, indicating a strong resistance to yaw-induced variations. The drag coefficient C_D, however, exhibits a slight increase, leading to a decrease in the lift-to-drag ratio L/D. Notably, the rolling moment coefficient M_x hovers around zero but reveals an increasing trend, suggesting a growing influence of yaw on the rolling stability as the yaw angle intensifies.

Vortex dynamics and pressure contour

In Figure 4.19, the pressure contours are displayed for distinct time frames, highlighting the rolling moment induced by pressure differences across the snake's body. The red arrows in the figures signify the direction and magnitude of the rolling moments, which result from the combined effect of forces and their respective arms. Figures 4.19(a1) to 4.17(a3) illustrate a trend of rolling moments towards the left, as indicated by the arrows, suggesting a predisposition of the body to roll in that direction due to the prevailing pressure differentials. Conversely, Figures 4.19(b1) to 4.19(b3) depict a state of balanced moments where the rolling tendency is

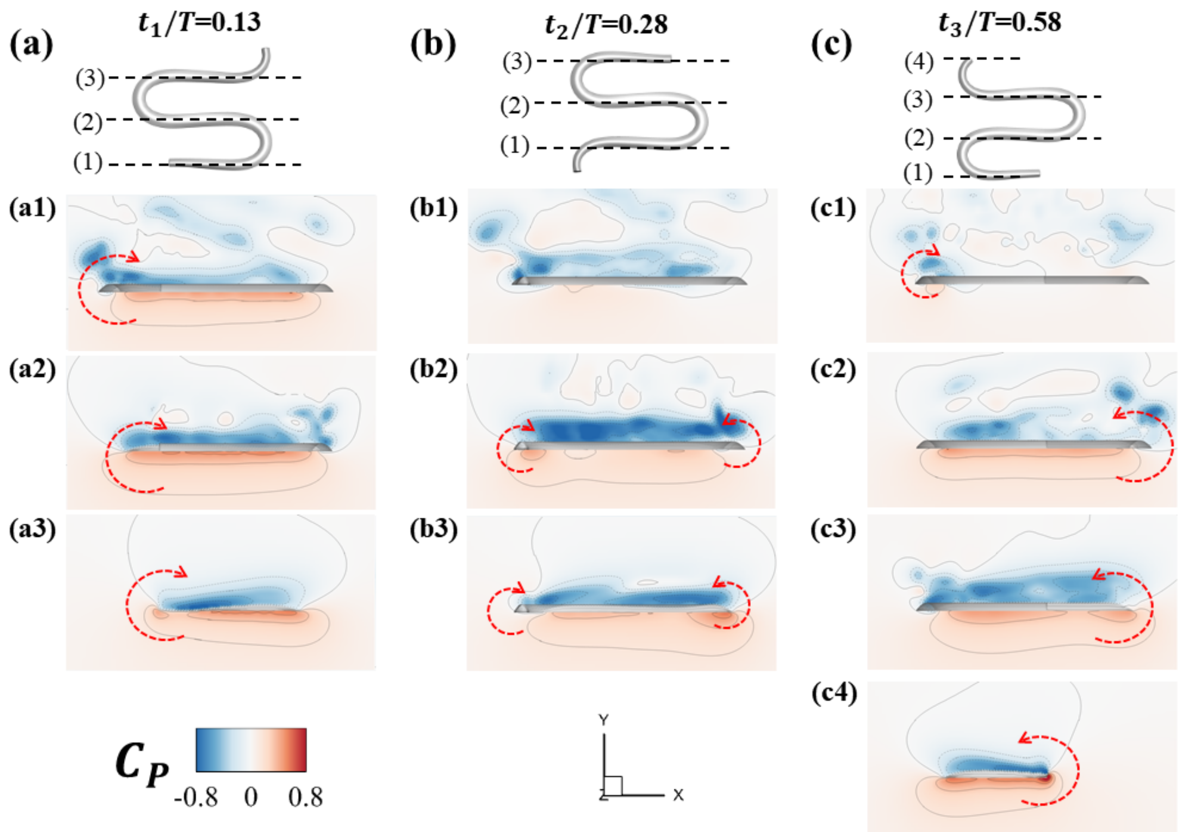

FIGURE 4.19: The pressure contour on different XOY planes for the horizontal undulating model at different time frames (a1) ~(a3) t_1/T = 0.13, (b1) ~(b3) t_2/T = 0.28 and (c1) ~(c3) t_3/T = 0.58. The red dashed arrow indicates the local moment.

neutralized, as shown by the arrows pointing in a balanced manner. Lastly, Figures 4.19(c1) to 4.19(c4) demonstrate a trend of rolling moments veering to the right, further emphasized by the direction of the arrows, indicating a shift in pressure distribution that predisposes the body to roll rightwards.

In Figure 4.20, the detailed depiction of vortex structures and span-wise flow across different time frames highlights the intricate flow dynamics surrounding the snake model during its undulatory motion. The presence of strong vortex attachment on the sides of the snake body is meticulously outlined within dashed boxes, underscoring the significant role of these vortical structures in generating aerodynamic forces. Specifically, Figures 4.20(a1) through 4.20(a3)

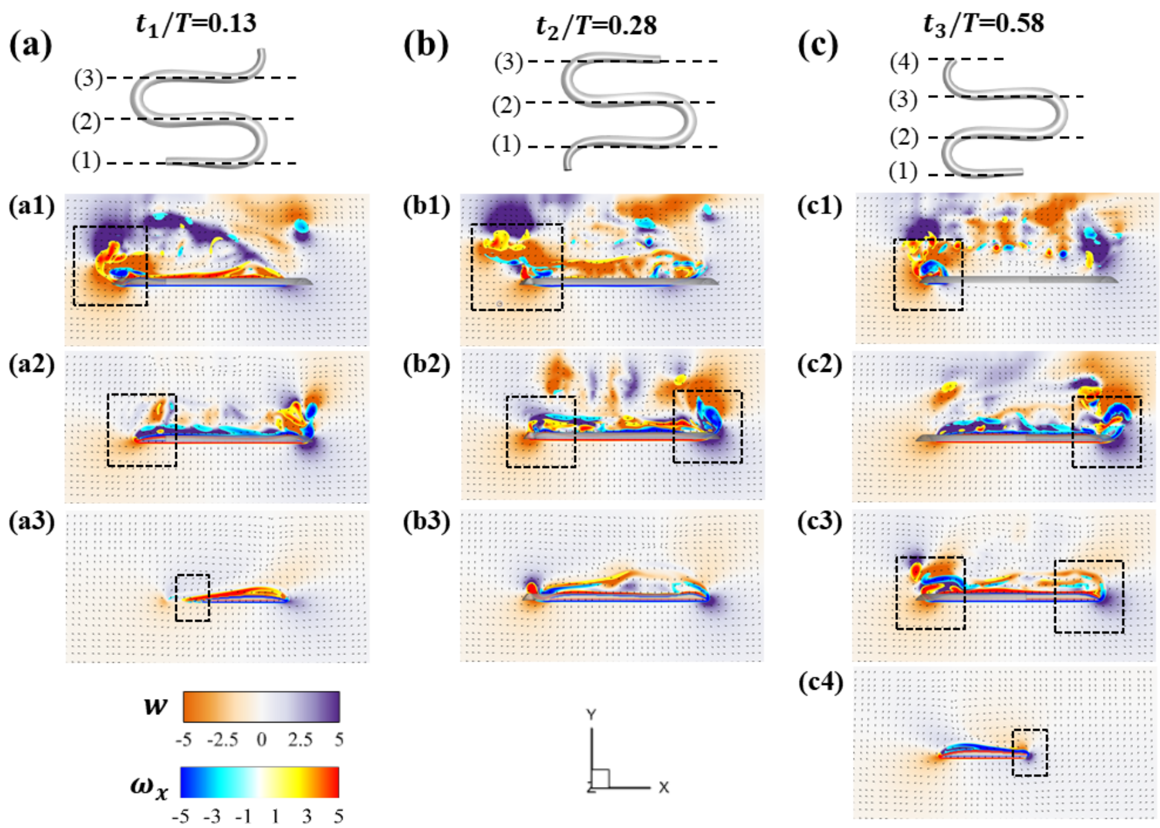

FIGURE 4.20: The instantaneous Z vorticity ω_z and spanwise flow w (in Z direction) contour n different XOY planes for the horizontal undulating model at different time frames (a1)~(a3) t_1/T=0.13, (b1)~(b3) t_2/T=0.28 and (c1)~(c4) t_3/T=0.58.

reveal a pronounced pressure differential on the left side, attributed to the robust attachment of vortices, which effectively contribute to the generation of a rolling moment in that direction.

Contrastingly, Figures 4.20(b1) through 4.20(b3) present a scenario of equilibrium where the moments are balanced, indicated by the directional arrows within the figures. This balance is a testament to the dynamic adjustment capabilities of the snake model, facilitating a momentary stability in its rolling motion. Progressing further, Figures 4.20(c1) through 4.20(c4) illustrate a shift in the pressure differential towards the right, again due to the strong attachment of vortices on the corresponding side. This attachment not only underscores the adaptability of the snake model in responding to rolling perturbations but also highlights the pivotal role of span-wise flow in reinforcing the interaction between the vortices and the snake body, thereby steering the model back towards a neutral alignment. The intricate interplay between the vortex dynamics and the span-wise flow elucidated in these figures provides a deeper understanding of the aerodynamic mechanisms at play, contributing to the overall stability and control of the snake model in aerial undulation.

This vortex generation process bears resemblance to the patterns observed in Gong et al.'s [10] previous research. Nonetheless, the introduction of vertical wave undulation introduces minor variances in the vortex development due to kinematic alterations. In contrast to purely horizontal undulation, vertical wave undulation modifies the local pitch angle, causing the body's cross-section to pitch forward and resulting in a diminished effective angle of attack (eAOA). This decrease in eAOA leads to weakened LEV vortex formation and diminished lift production.

4.4.4 Effect of Vertical wave undulation in rolling

In this section, we will discuss how the vertical wave undulation affects the rolling performance and vortex structures of flying snakes during gliding.

Rolling performance

In Figure 4.21, the impact of varying vertical wave amplitudes on the aerodynamics of the model at a rolling angle of $\beta = 5°$ is illustrated. Analogous to the trends observed for the lift and drag coefficients ($\bar{C_L}$ and $\bar{C_D}$) in the absence of rolling, a peak in performance is reached at a minimal amplitude of 5°, followed by a subsequent decline. Remarkably, the rolling moment exhibits a similar pattern, achieving its maximum at an amplitude of 5°. This phenomenon suggests that at an amplitude of 5°, the snake model exhibits a pronounced response to perturbations, tending to revert to a neutral stance and thereby demonstrating enhanced static stability.

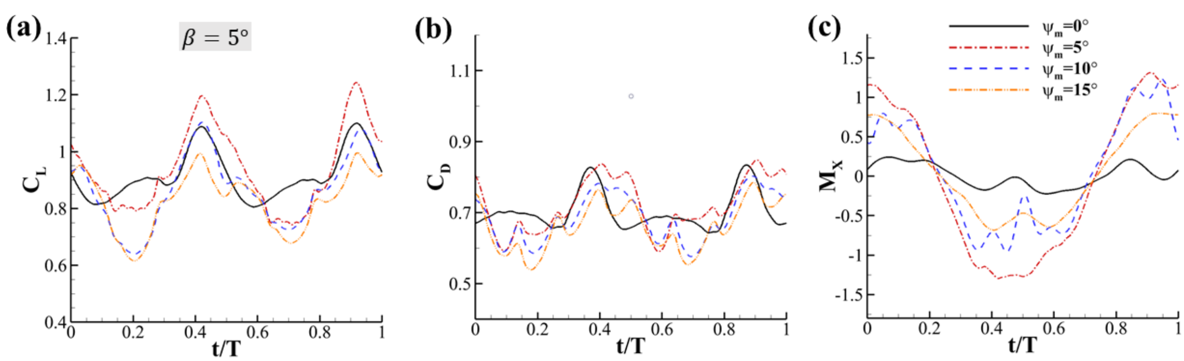

FIGURE 4.21: The instantaneous force coefficients for different vertical wave undulation amplitude ψ_m. (a) Lift Coefficient. (b) Drag Coefficient (c) Rolling Moment Coefficient.

In Figure 4.22, the impact of the rolling angle on the aerodynamic performance of the snake model at a vertical wave amplitude of $\psi_m = 10$ degrees is meticulously examined, highlighting the model's response to slight disturbances during gliding. The analysis further elucidates the

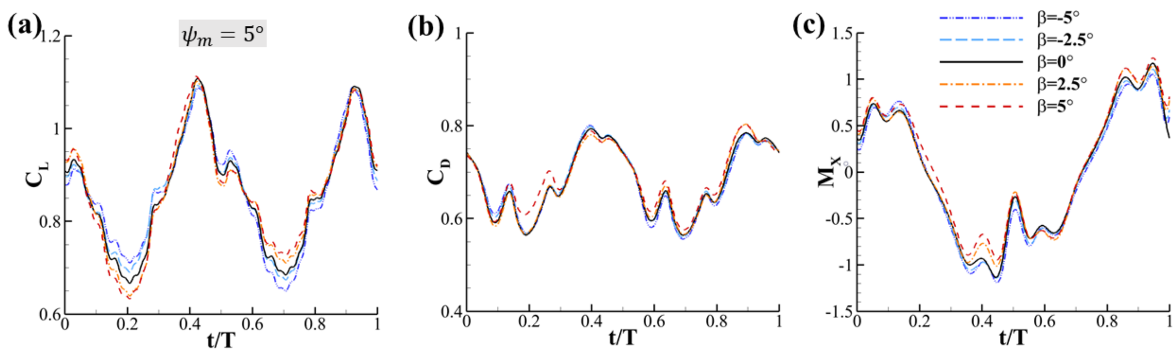

FIGURE 4.22: The instantaneous force coefficients for different rolling angles β at $\psi_m = 10°$. (a) Lift Coefficient. (b) Drag Coefficient (c) Rolling Moment Coefficient.

minimal variation in the lift and drag coefficients, with the average discrepancy being under 0.5% for C_L and 1.5% for C_D. Although a notable peak deviation of 5% is observed, this discrepancy is effectively neutralized by the counteracting peak, thereby exerting a negligible influence on the overall average values.

The rolling moment, however, exhibits a significant alteration at the peak times, markedly affecting the average rolling moment experienced by the model. This pronounced change underscores the critical role of the rolling moment in the dynamic stability of the gliding snake model, especially in response to small perturbations. The detailed insights gleaned from Figure 4.22 shed light on the delicate balance between maintaining aerodynamic efficiency and ensuring rolling stability, pivotal for the nuanced control and maneuverability of the snake model in aerial undulation.

Rolling stability

According to previous discussion,the rolling stability can be measured as the derivative of the rolling moment towards the small perturbation. We summarized the averaged rolling moments and calculated the linear regression slope for different vertical wave undulation amplitudes in Figure 4.23

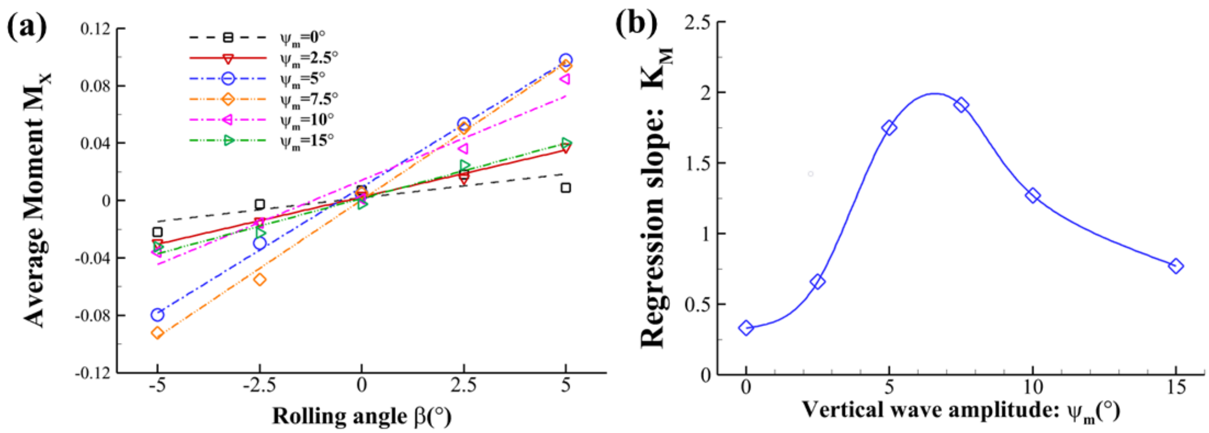

FIGURE 4.23: (a)The average moment for different vertical wave undulation amplitudes ψ_m at small rolling angles. (b) The regression slope κ for different vertical wave undulation amplitude ψ_m.

In Figure 4.23(a), the depiction of the average rolling moment in relation to varying vertical wave undulation amplitudes ψ_m at minimal rolling angles is presented, while Figure 4.23(b) showcases the variation of the regression slope κ with the amplitude ψ_m. It's observed that the rolling moment adheres to a linear trend, maintaining a position around the zero point with a positive inclination. This suggests that small adjustments in the rolling angle induce proportional changes in the rolling moment, indicative of a systematic response of the flying snake model to minor perturbations.

In Figure 4.23(b), it is shown that as the amplitude ψ_m escalates, a corresponding increase in the regression slope κ is noted, peaking at $\psi_m = 7.5°$ before exhibiting a decline. This peak signifies the amplitude at which the response of the flying snake model to rolling angles is most pronounced, implying a heightened state of stability. Beyond this optimal amplitude, the effectiveness in counteracting rolling deviations diminishes. The magnitude of the regression slope

κ serves as an indicator of the system's stability; the larger the slope, the stronger the system's propensity to revert to its initial orientation upon being disturbed. This dynamic underscores the critical role of vertical wave undulation in enhancing the aerodynamic stability of flying snake models, particularly in mitigating rolling instabilities.

Vortex Dynamics

In this subsection, we will go into a detailed analysis of the effect of vertical wave undulation amplitudes to the vortex dynamics. According to the previous discussion, we picked the key timeframe at $t/T = 0.41$ for detailed analysis to reveal the flow physics and flow change process for two different ψ_m.

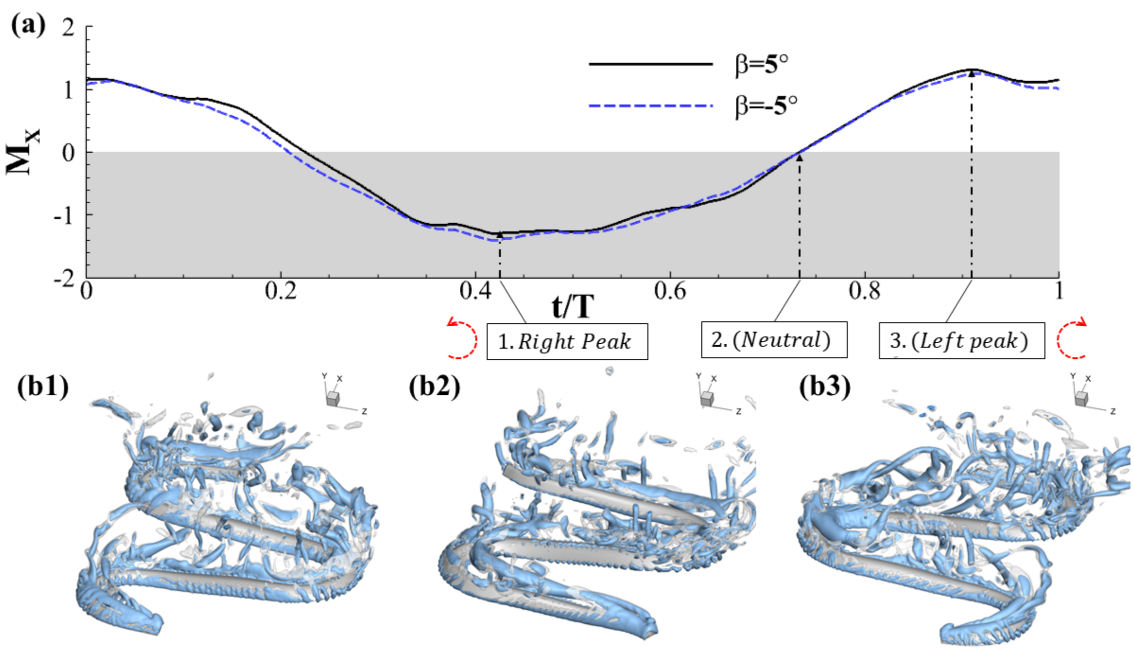

FIGURE 4.24: (a) Instantaneous rolling moment history in one cycle for the undulation motion with vertical wave amplitude $\psi_m = 10°$ with two rolling angles. (b) vortex topology at right moment peak ((1) t_1/T = 0.45), neutral position ((2) t_2/T = 0.73) and left peak ((3) t_3/T = 0.91)for $\beta = 5°$ case.

Figure 4.24 presents the force coefficients throughout a single cycle of steady undulation for a scenario where a nominal rolling angle has been incorporated. This analysis, akin to observations from horizontal undulations, showcases two prominent peaks in lift generation per undulation cycle. Introducing a positive rolling angle yields a diminished peak in lift during the left-to-right (L-R) transition, in contrast to a heightened peak during the right-to-left (R-L) transition. The drag coefficient exhibits a similar pattern, with a notable increase specifically at $\gamma = -5°$. The coefficients of rolling moment feature a pair of symmetric peaks with opposing signs, each aligned with a respective stroke. A minor peak to the left is noticeable at $t/T = 0.05$, while a more pronounced peak to the right becomes apparent at $t/T = 0.44$, highlighting the model's nuanced rolling dynamics amidst aerial undulations.

Pressure contour and span-wise flow

In Figure 4.25, distinct snapshots of pressure distribution across the snake model are showcased, revealing the origins of rolling moments due to asymmetric pressure across the body. Illustrated by red arrows, these moments are a product of force and leverage, with Figures 4.25(a1) to 4.25(a3) depicting a leftward bias in rolling moment, as indicated by the arrow directions, hinting at a pressure-induced tendency for the model to roll left. In contrast, Figures 4.25(b1) to 4.25(b3) represent a state of equilibrium with moments counteracting each other, leading to a balanced rolling orientation as depicted by the balanced arrow orientations. Figures 4.25(c1) to 4.25(c4), however, illustrate a rightward rolling moment, with arrows pointing right, suggesting a shift in pressure dynamics that inclines the body towards a rightward roll.

Figure 4.26 delves into the vortex dynamics and lateral flow at various intervals, highlighting the

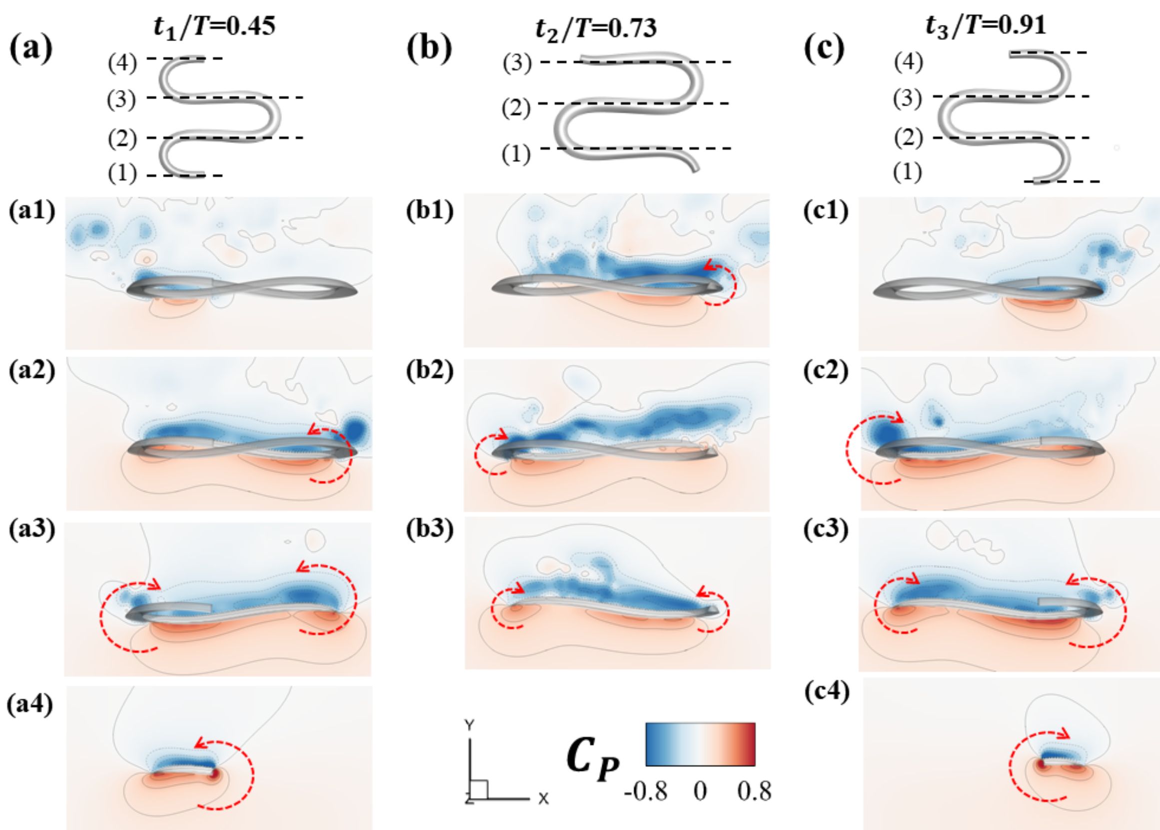

FIGURE 4.25: The pressure contour on different XOY planes for the horizontal undulating model at different time frames (a1)~(a4) t_1/T=0.45, (b1)~(b3) t_2/T=0.73 and (c1)~(c4) t_3/T=0.91. The red dashed arrow indicates the local moment.

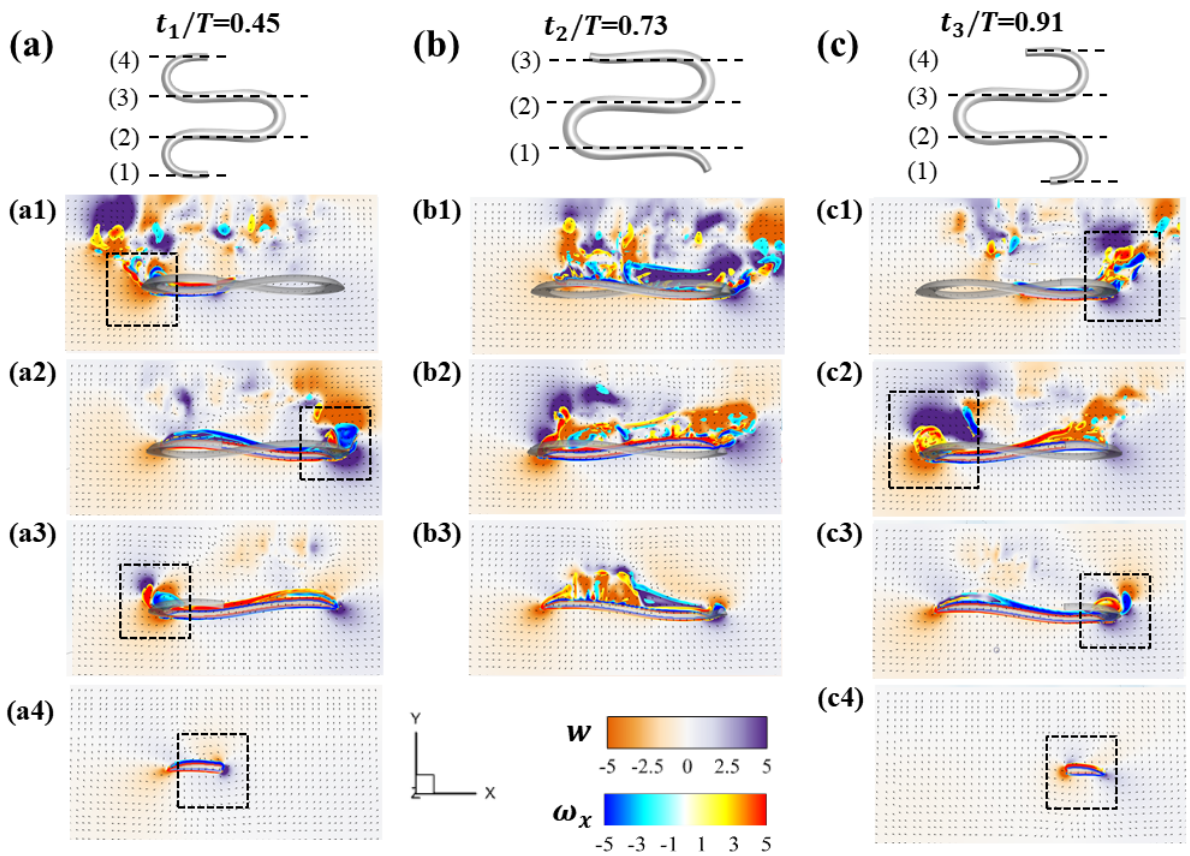

FIGURE 4.26: The instantaneous Z vorticity ω_z and spanwise flow w (in Z direction) contour n different XOY planes for the horizontal undulating model at different time frames (a1)~(a4) t_1/T=0.45, (b1)~(b3) t_2/T=0.73 and (c1)~(c4) t_3/T=0.91.

nuanced flow interactions that the snake model undergoes during undulation. The presence of prominently attached vortices on the body's flanks, marked by dashed outlines, plays a crucial role in influencing aerodynamic forces. In particular, Figures 4.26(a1) to 4.26(a3) display a leftward pressure disparity, attributed to the strong vortex attachment, which induces a rolling moment to the left.

Conversely, Figures 4.26(b1) to 4.26(b3) showcase a harmonious balance where the moments neutralize, showcasing the model's adeptness in maintaining a stable roll orientation momentarily. Advancing to Figures 4.26(c1) to 4.26(c4), a noticeable pressure shift to the right is observed, propelled by the dominant vortex attachment on that side. This not only exemplifies the model's responsive adjustment to rolling disturbances but also underscores the critical influence of lateral flow in enhancing vortex-body interactions, guiding the model towards a balanced stance. The detailed exposition of vortex dynamics intertwined with lateral flow in these figures sheds light on the underlying aerodynamic principles that bolster the stability and maneuverability of the snake model amidst aerial undulation.

4.5 Conclusions

In this study, we numerically investigated a flying snake's 3D vertical bending locomotion during aerial gliding. The geometry of the snake model was reconstructed based on the realistic cross-sectional shape of a snake body, and the motion of the undulation was based on its kinematics, with a mathematical equation applied to the model. The main focus of this work was to examine the aerodynamic performance improvement mechanism with such motion and the three-dimensional vortex dynamics. Various parameters that could lead to changes in performance on the body were studied, including the vertical wave undulation amplitude ψ_m and dorsal-ventral bending amplitude ψ_{DV}.

The flow structures and vortex dynamics in this case are found to be similar to those of horizontal undulation. The formation of oblique LEV and TEV vortex tubes has been observed, and it was found that the production of lift is closely related to the formation of LEV. The maximum lift is generated when two LEVs are formed on the straight part of the body before the first one is shed off.

Results show that the vertical wave undulation amplitude enhances aerodynamic performance as it increases at a small amplitude, while it lessens the performance as it further increases. For a small increment compared with pure horizontal undulation, the force production increases and reaches a peak at $\psi_m = 2.5°$, while the L/D and C_L/C_{PW} reach a peak at $\psi_m = 5°$. When ψ_m further increases, both the lift production and the efficiency decrease. The local effective angle of attack (eAOA) is decreased by the vertical wave undulation, especially for the straight portion of the body, which leads to the loss of lift production.

Dorsal-ventral bending (ψ_{DV}) as one of the important vertical motions contributes to the aerodynamic performance through a different mechanism. Increasing ψ_{DV} causes the tail to curl downward and separates the distances between the bodies in the vertical direction of the flow. When drifted apart, the interaction between the bodies weakens. With less effect on the posterior body, the lift generation will improve significantly, at the cost of increasing power consumption and reducing gliding efficiency. Conversely, decreasing ψ_{DV} bends the snake tail up and the aerodynamic performance develops in the opposite direction. The wake-body interaction increases, and the LEV and TEV formed on the posterior body merge with the upstream flow, thus decreasing the lift production. With less drag, the gliding efficiency increases. The flying snake may apply different dorsal-ventral bending directions to adjust its gliding strategy to gain more lift for deceleration or to achieve more efficient gliding. Further studies regarding dynamically changing snake's horizontal or vertical undulatory locomotion are expected to extend the knowledge of the aerodynamic performance enhancement mechanism in understanding snake gliding behavior and to provide inspiration for the design of gliding snake aircraft robots.

The snake's ability to maintain stability and control during gliding, despite the absence of wings or other conventional flight appendages, is a testament to the complex interplay between its body morphology, undulatory motion, and the surrounding fluid dynamics. This study delves into the effects of undulation motion on the rolling stability of the flying snake, shedding light on the underlying aerodynamic principles that facilitate such a unique mode of locomotion.

In steady snake flight, vortex structures are generated along the body in a pattern consistent with the frequency of vortex shedding, resulting in a settled force distribution influenced by the body's shape. This leads to a constant rolling moment during gliding, causing the snake to deviate from its intended flight path due to the uneven distribution of aerodynamic moments. The inherent instability in the steady gliding of a flying snake highlights the crucial role of vortex symmetry in determining its rolling stability.

The introduction of horizontal undulation into the snake's flight kinematics significantly alters its rolling stability. This periodic motion balances the dynamic moments over a flight cycle, enhancing the snake's resistance to rolling deviations. The attachment of vortices along the body's sides, particularly during positive rolling angles, generates larger moment arms that produce stronger counteracting moments, suggesting that horizontal undulation is essential for stabilizing the snake against minor perturbations.

Vertical wave undulation introduces an additional layer of complexity to the snake's rolling stability. The stronger attachment of vortices due to vertical undulation is closely linked to force production, leading to increased stability at moderate amplitudes. However, beyond a certain threshold, the stability benefits of vertical undulation diminish, highlighting the intricate balance between undulation amplitude and its impact on rolling stability. This study underscores the sophisticated aerodynamic mechanisms employed by flying snakes to maintain control during aerial undulation, offering valuable insights for the development of bio-inspired robotic systems.

5 The intra-body interactions between snake body segments

In this chapter, we would focus the study on the intra-body interactions between snake body segments. Due to the limitation of the simulation resolution, the unsteady undulation motion and the complicated flow near the posterior body, it would be difficult to identify the vortices and measure the force with respect to a specified region. As an alternative, we apply the two-foil system model in two-dimensional space to analyze the flow near the body. Moreover, using the simplified model enables us to add dynamic motion to the posterior body which has been observed in real snake gliding. This makes our study a more canonical problem and brings more fundamental understanding to the two-foil system in application and design.

5.1 Problem statement

The tandem foil system was inspired from the horizontal and vertical undulation motion in 3D flying snake model. According to the observation, the snake undulation can be decomposed into the horizontal undulation and vertical bending motion[30] and the motion can be controlled by a pair of parameters. In the observation, the vertical distances between the body segments can be 3 to 4 chord lengths and the vertical distances between the segments can be -2 to 2 chord lengths. Further more, by increasing the horizontal bending amplitude ϕ_θ or wave number ν, the horizontal gaps may be increased. By increasing the vertical undulation wave amplitude ψ_m or the dorsal-ventral bending amplitude ψ_{DV}, the vertical distances may be increased (see more details in methodology chapter).

In the present research, all snake airfoils share the same shape as the 2D cross-section studies in [32], [42] with normalized chord length c = 1. The setup of the cases is presented in Figure 5.1. The two snake airfoils are placed in the in-line configuration facing the horizontal flow from the left. The angle of attack(AOA) is then pitched up to simulate the condition of gliding. Holden *et al.* [42] and Krishnan *et al.* 's work [43] validated that for this 2D snake airfoil, the lift generation reaches the maximum at AOA=35°. In the current study, we set the two airfoils' AOA to be 35° for all static cases. The snake airfoil downstream has relative positions. From Jafari *et al.*'s definition[32], we define the horizontal distance between the centers of the airfoil as Δx (defined as gap distance) and Δy as the vertical distance (defined as stagger distance).

For a starting case, we study the parametric pair (Δx, Δy) with the range of $3c \leq \Delta x \leq 4c$ and $-2c \leq \Delta y \leq 2c$. Positive Δy is observed near the body's head portion (see 1.2 (b)) which was not covered in the previous study. Furthermore, pitching is applied to the downstream airfoil for the dynamic motion study. The equation to describe the pitching is:

$$\alpha = \alpha_0 + \alpha_m sin(2\pi f t + \phi_\alpha) \tag{5.1}$$

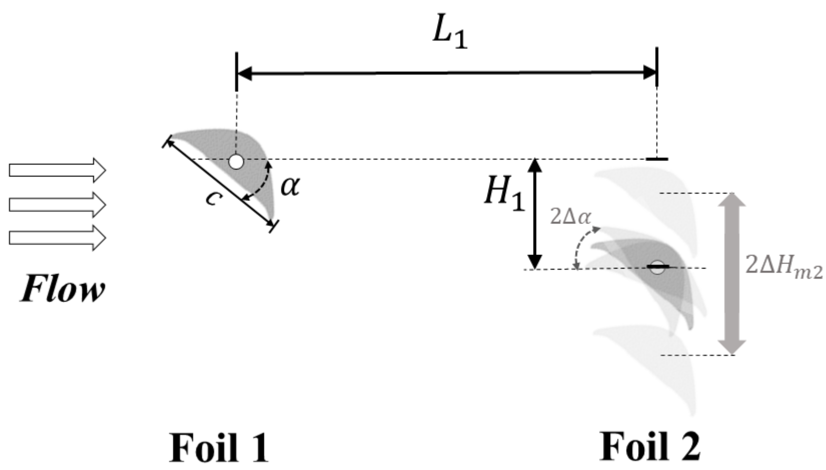

FIGURE 5.1: Schematic of two-foil system with pitching and heaving motion applied to the anterior body.

where α_0 is the AOA = 35° in the current study. α_m and f represent the pitching amplitude and frequency. ϕ_α is the pitching motion phase.

The snake airfoil downstream has relative positions. From Jafari et al.'s definition, we define the horizontal distance between the centers of the airfoil as L (defined as gap distance) and H as the vertical distance (defined as stagger distance). Similarly, heaving is applied to the downstream airfoil for the dynamic motion study. The equation to describe the heaving is:

$$H = H_0 + \Delta H_m \sin(2\pi f t + \phi_h) \tag{5.2}$$

where H_0 is the initial vertical distance between the foils, ΔH_m and f represent the heaving amplitude and frequency, ϕ_h is the heaving motion phase.

5.2 Solitary foil: aerodynamic performance and wake dynamics

Our current study presents the aerodynamic performance of a solitary flying snake airfoil at different AOAs at Re=1000. (Shown in Figure 5.2.) This simulation is comparable with the 2D simulation done by Krishnan *et al.* [43] and validated the accuracy of our solver. The AOA ranges from 10° to 45° with an increment of 5°. The lift coefficient (C_L) increases vastly before 30° and reaches a peak value of 1.998 at 35°, which is the AOA we choose for further tandem foil study. Stall happens right after this critical AOA, where the C_L decreases. On the other hand, the drag coefficient (C_D) almost increases linearly with AOA as well as a higher increase after AOA=35°. The lift-to-drag ratio L/D also follows the convex trend and reaches a maximum at AOA=30° with the value of L/D=1.674.

The vorticity contour of the maximum lift case is presented in Figure 5.2 (c). The case (AOA=35°) has a wake with classic von-Kármán vortex street. The red (positive) and blue (negative) regions represent a series of vortex pairs behind the trailing edge of the snake airfoil. In Figure 5.2 (d), the average wake is presented with the stream-wise velocity field. The wake's downward deviation shows the direction of wake propagation and the blue region represents the reverse flow, which will influence the downstream airfoil's aerodynamic performance.

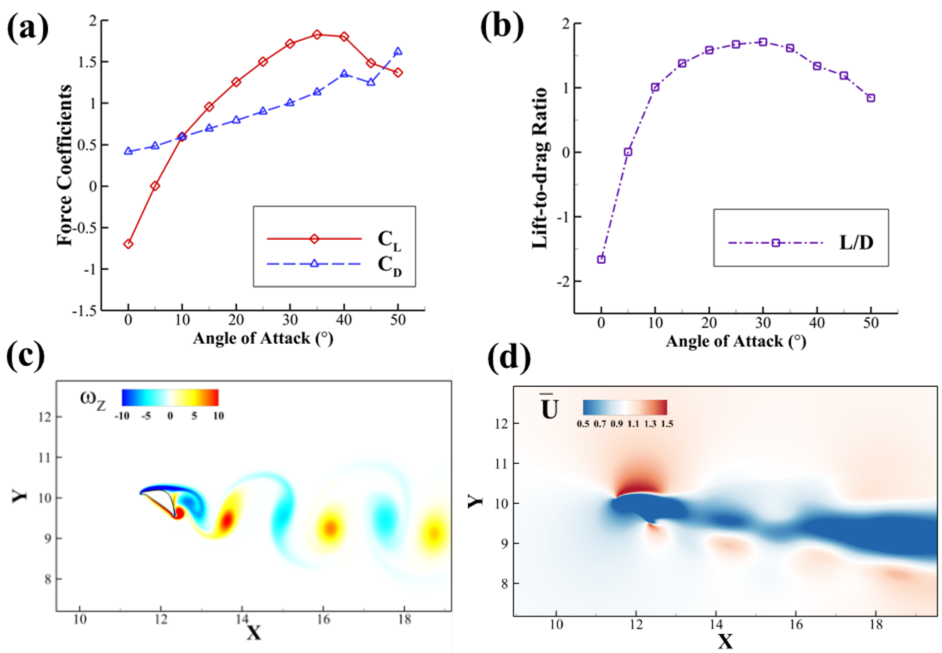

FIGURE 5.2: (a) Time-averaged lift coefficient $\overline{C_L}$, drag coefficient $\overline{C_D}$ different AOAs, with Re=1000 (b) lift-to-drag ratio L/D of a single flying snake airfoil at different AOAs. (c) Vorticity contour for case AOA=35°, Re=1000 at peak lift production; (b)Time-averaged stream-wise velocity field for the same case.

5.3 Two tandem foil system: aerodynamic performance and wake dynamics

In this section, two flying snake airfoils are placed in tandem configuration. We investigate the aerodynamic performance and vortex structures based on different stream-wise and vertical distances between the foils. We start with the Reynolds number 1000 and AOA=35°.

5.3.1 Aerodynamic performance

The aerodynamic performances of the two foils are presented in Figure 5.3. The intermediate white region of the colormap is set to be the average value of solitary foil ($\overline{C_L}$ = 1.9502, $\overline{L/D}$ = 1.5800). The hot region (red and yellow) represents performance enhancement, while the cold region (cyan and blue) represents performance reduction. From Figure 5.3 (a1)~(a3), it is shown that the interaction between the two foils reduces lift production in most cases. The lift production of upstream foil will be increased when the downstream foil is in the lower vertical position ($C_{L\_upstream}[\Delta x$ = 4.00c, Δy = -2.00c] = 2.2453), while the lift production of downstream foil will be increased when itself is in upper vertical position($C_{L_downstream}[\Delta x$ = 4.00c, Δy = 2.00c] = 2.3542). Figure 5.3 (a2) shows that the low lift production region for downstream foil is located at the downstream wake from upstream foil, between the range of $-1c \leq \Delta y \leq 0.5c$. However, in Figure 5.3 (b2), it is shown that the high L/D region for downstream is also located in upstream foil's downstream, yet with a smaller range of $-1c \leq \Delta y \leq -0.25c$. This trend is also affecting the average system performance. We calculate the system-average with the following:

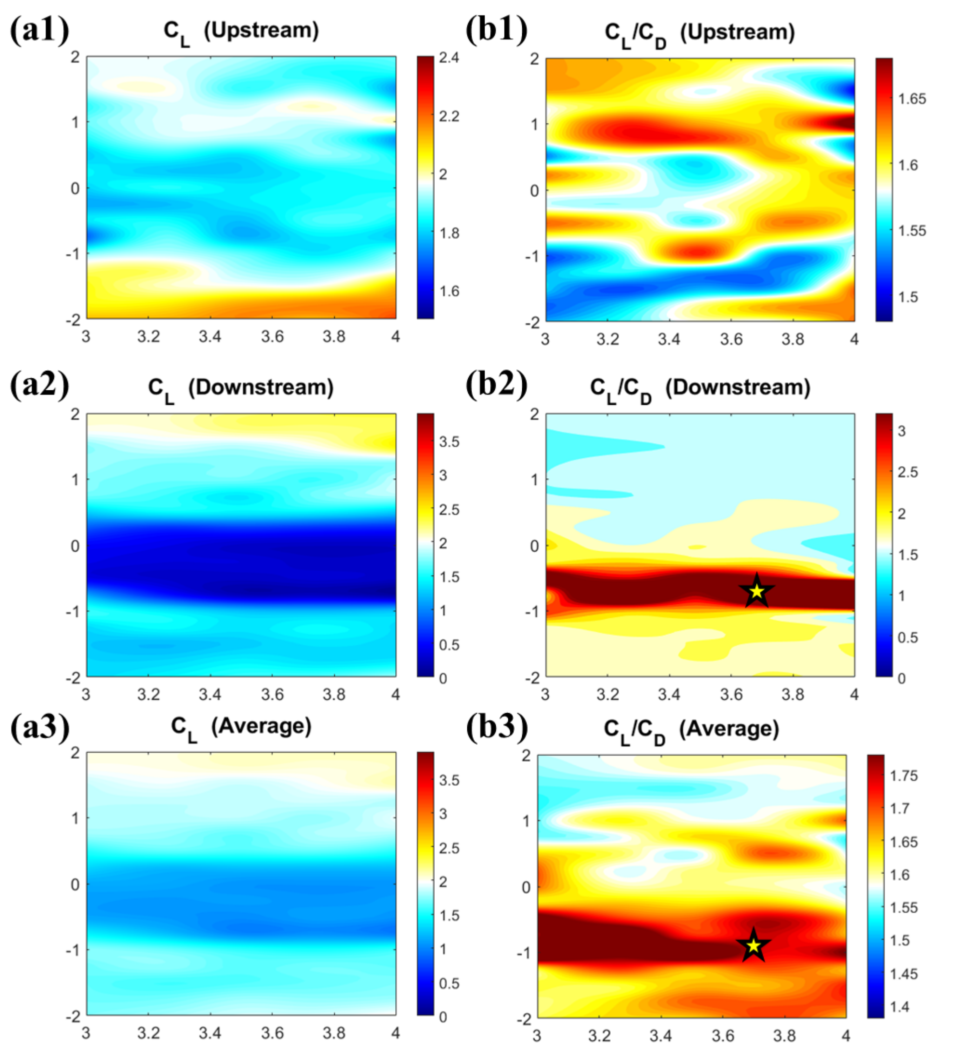

FIGURE 5.3: Aerodynamic performance of two tandem flying snake airfoils at Re = 1000. (a1 $\sim$ a3): Time-averaged lift coefficients for upstream foil, downstream foil, and system average; (b1 $\sim$ b3): Lift-to-drag ratio for upstream foil, downstream foil, and system average.

$$C_{L\_avg} = \frac{C_{L\_upstream} + C_{L\_downstream}}{2} \tag{5.3}$$

$$L/D_{avg} = \frac{C_{L\_avg}}{C_{D\_avg}} \tag{5.4}$$

Since the L/D performance is higher in downstream foil, the overall performance increases for the system average. A high L/D region shown in Figure 5.3 (b3) appears in a similar region as the downstream foil. Compared with solitary foil, downstream foil in the system trades its lift for the enhancement of L/D, which is affected by the downstream wake of upstream foil.

Numerous animals which fly or glide adjust the lift-to-drag ratio in order to enhance efficiency or to make maneuvers. The ancient feathered dinosaur *(Microraptor)* may have laid its legs flat to achieve a better L/D ratio, for a longer horizontal gliding capability[78]. Flying fish through experiments and reported that the flying fish expanded their pelvic fins and flew close to the surface of the sea to decrease the drag force and elevate the L/D [79]. Ornithologists have determined that birds are able to adjust their wing camber and aspect ratio through the practice of functional morphology, leading to a greater L/D [80]. The lift-to-drag ratio can be adversely influenced by factors such as alteration in the wing transmissivity and aeroelasticity, which influence the production of lift and drag [81], or the moulting of feathers which lowers the L/D ratio to 7 from 10.5 when the feathers are full [82]. Some birds are able to modify their lift-to-drag ratios with each wingbeat, allowing them to utilize aerodynamic force vectoring and maneuver up to an angle of approximately 100° relative to the horizontal plane[83]. In the current, we may explore different parameters and find the effects on the L/D performance.

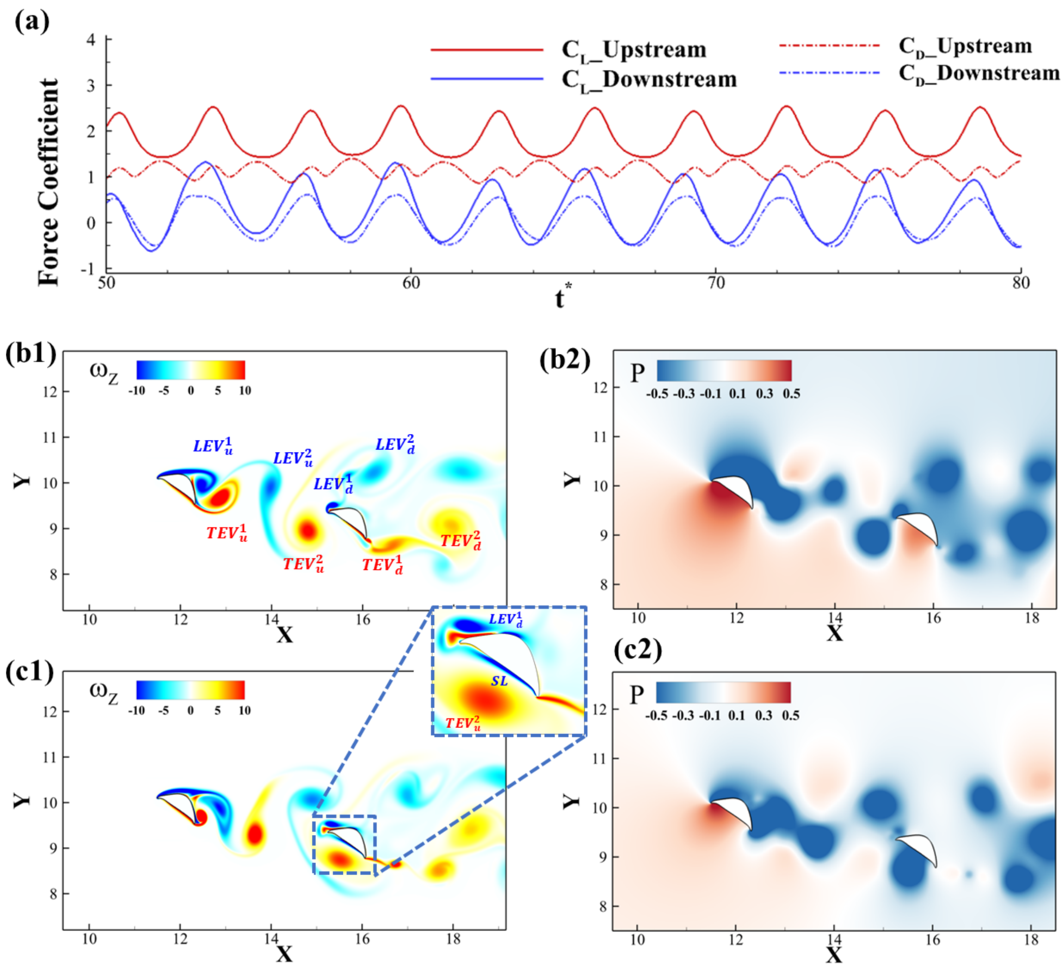

FIGURE 5.4: (a1) Vorticity contours and (a2) pressure contours for the configuration Δx = 3.75c, Δy = -0.75c at the snapshot of the maximum lift production on downstream foil. (b1) and (b2) show the same information in the snapshot of the minimum lift production.

5.3.2 Wake structure

In Figure 5.4, the flow information for the best-performed configuration (Δx = 3.75c, Δy = -0.75c) is presented. From Figure 5.4 (a1), the TEV_U^1 shed off from the trailing edge of upstream foil propagates downstream. Meanwhile, the LEV_D^1 and TEV_D^1 formed on the edges provide two low-pressure regions, which are shown in Figure 5.4 (a2). With the vortex TEV_U^1 traveling downstream, it will reach the ventral surface of the downstream foil, inducing a negative shear layer. As shown in Figure 5.4 (a2) and (b2), the least lift productions come with the two negative vortex region leading to low-pressure regions on both surfaces. The low lift production does not necessarily mean low lift-to-drag ratio performance since its drag is also small due to a small pressure difference.

The time-averaged stream-wise velocity contour is presented in Figure 5.5 to investigate the relationship between different configurations. The best-performed cases usually happen in the wake of the upstream airfoil. By taking advantage of the oncoming vortex, the downstream foil almost reaches zero drag, leading to high L/D performance, which is in Figure 5.5 (a). For worst performance cases, as shown in Figure 5.5 (b), two parallelly formed wakes separate from each other and cannot take advantage of each other. Figure 5.6 summarizes the primary vortex structure for different configurations of the foils. As previously mentioned, the upstream wake is a typical von-Kármán vortex street. When the downstream foil is located in the

The wake information also explains the lift production in Figure 5.3. The high lift production for upstream or downstream foil locates at $\Delta y \leq -1.5c$ and $\Delta y \geq 1.5c$. Those are the positions where the wakes are separated. With Newton's third law, when the upstream foil is higher, it

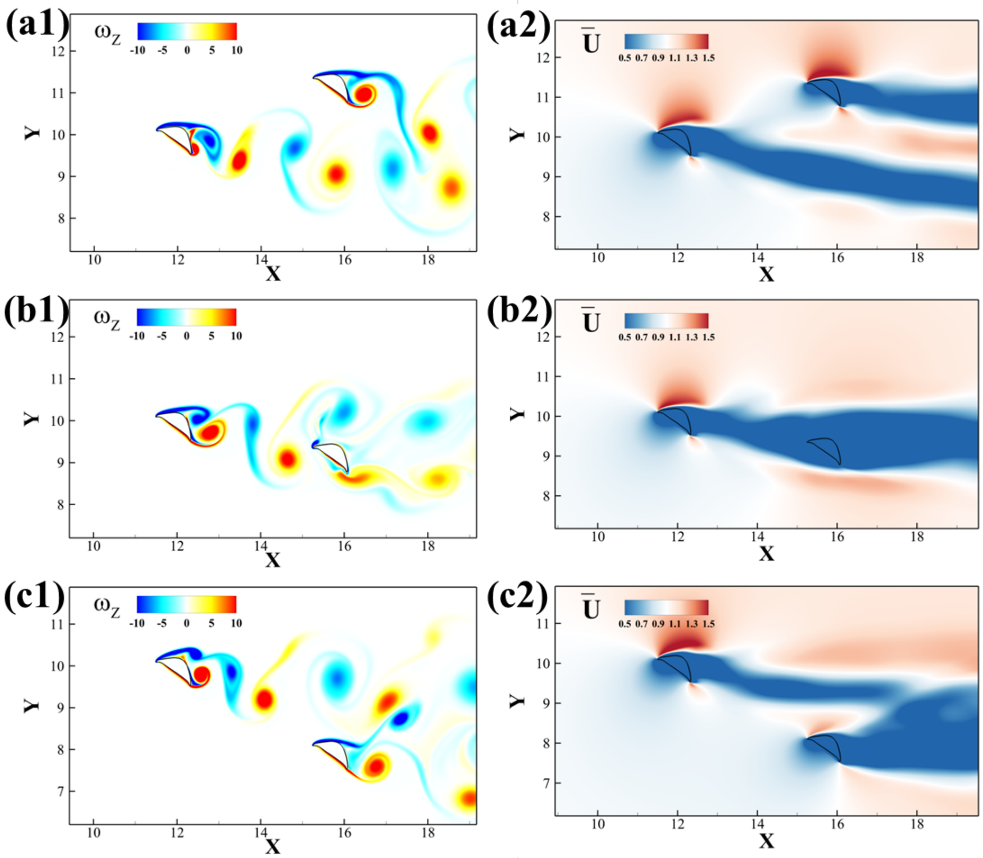

FIGURE 5.5: (a) Vortex contours and (b) time-averaged stream-wise velocity fields of two tandem flying snake airfoils under different configurations: (1) Δx = 3.75c, Δy = 1.25c (2) Δx = 3.75c, Δy = -0.75c (3) Δx = 3.75c, Δy = -2.00c

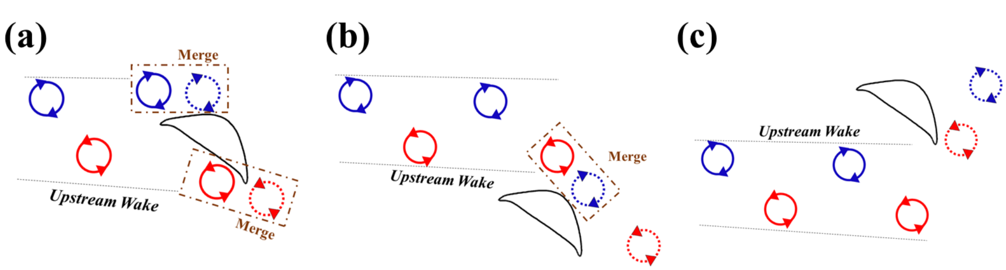

FIGURE 5.6: Schematic of vortex interaction when the downstream foil is located (a) in the middle of (b) below (c) above the upstream wake.

will experience the interaction and the force lifting it while the downstream foil's lift reduces. The same explanation holds when the upstream foil is lower and the downstream foil has a better overall performance. Nevertheless, when the wake merges into one, the downstream foil takes advantage of the wake and brings higher performance in lift-to-drag ratio, leading to higher gliding efficiency.

5.4 Effects of Reynolds number

In this section, we focus on the effects of the Reynolds number on aerodynamic performance and vortex dynamics.

5.4.1 Aerodynamic performance

The same two-foil study is conducted, and the aerodynamic performance as the baseline cases are presented in Figure 5.7.

Generally speaking, Re=500 and Re=1000 share a similar pattern in aerodynamic performance. When downstream foil locates at $\Delta y \leq -1.5c$, the lift production for upstream foil outperforms the solitary foil. Yet, when downstream foil locates between $\Delta y - 1.5c$, the lift production for downstream foil is better than the solitary foil. The high L/D region for the downstream foil is still located in the wake of the upstream foil. By calculating the cycle average, it is shown in Figure 5.7 (a3) that the lift production of the system is reduced due to the interaction. The lift-to-drag ratio, on the other hand, is raised when the downstream foil is located in the wake of the upstream foil. However, there are some differences that need to be noted. First, the

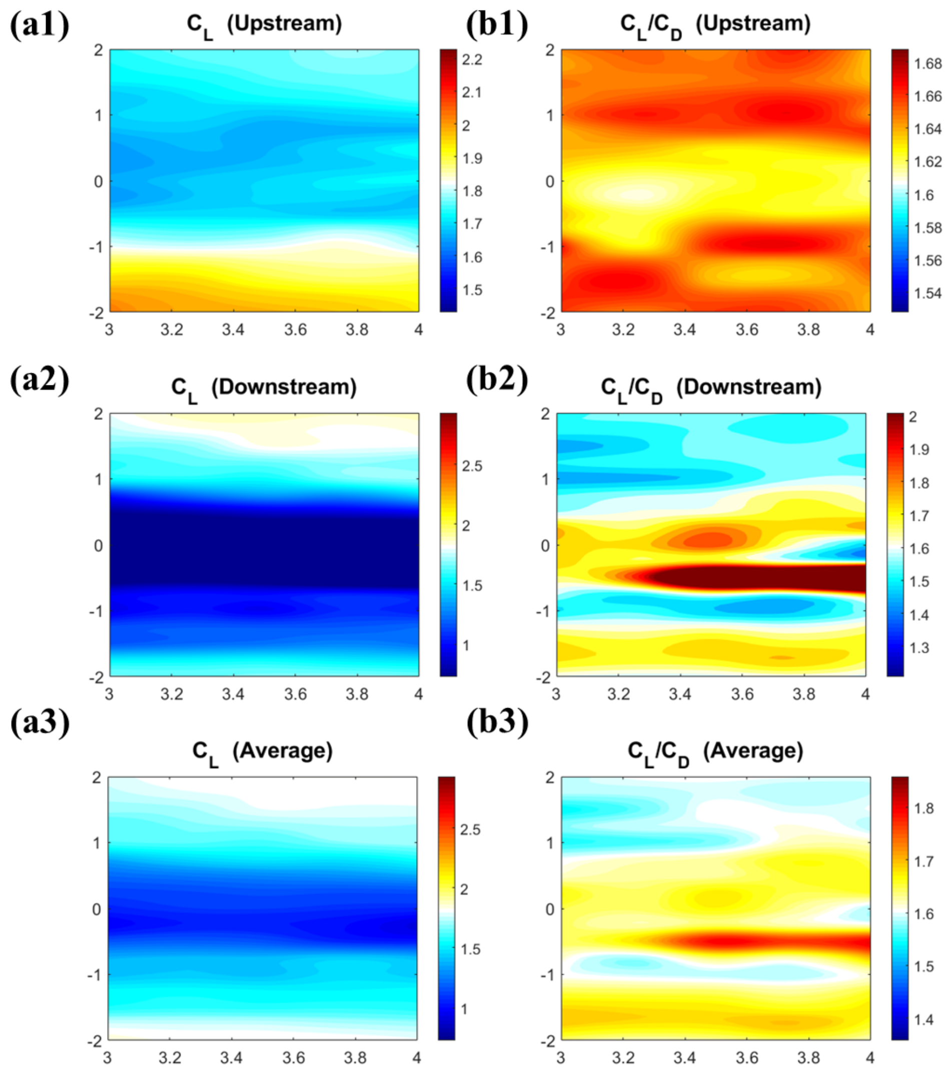

FIGURE 5.7: Aerodynamic performance of two tandem flying snake airfoils at Re = 500. (a1)-(a3): Time-averaged lift coefficients for upstream foil, downstream foil, and system average; (b1 $\sim$ b3): Lift-to-drag ratio for upstream foil, downstream foil, and system average.

average value of solitary foil is now $\overline{C_L}$ = 1.8276, $\overline{L/D}$ =1.6078, which shows a similar trend as previous Reynolds number effect studies[42], [43]. Second, the high L/D region's width reduces, indicating that the strength of the wake fades. Also, the hot region shifts upwards compared with the higher Reynolds number case, corresponding with the wake deviation results presented in the upcoming section.

5.4.2 Vortex dynamics

In this section, we made a comparison between different Reynolds number cases to provide a better understanding of vortex dynamics and its relation to aerodynamic performance. We kept the exact configuration of Δx = 3.75c, Δy = -0.75c and altered the Reynolds number.

From the performance contour presented in Figure 5.3 and 5.7, it can be predicted that with the Reynolds number increase, the lift production reduces in the wake region, yet the lift-to-drag ratio increases. Also, the wake region will shift slightly with the Reynolds number increase. The aerodynamic performance is presented in Figure 5.8. From the results, it has been seen that for the best lift-to-drag ratio configuration at Re=1000, either increasing or decreasing the Reynolds number will affect the performance of the downstream snake foil. We will prove this by providing more information about the wake and vortex dynamics.

We presented the time-averaged velocity fields in Figure 5.9. The deviation angles of the wake from the upstream foil increase with the Reynolds number, which is indicated by the dashed line. A higher deviation angle corresponds with the lift production increase for upstream foil. The performance of the downstream airfoil is also highly related to the wake and vortex interaction, yet less explicit.

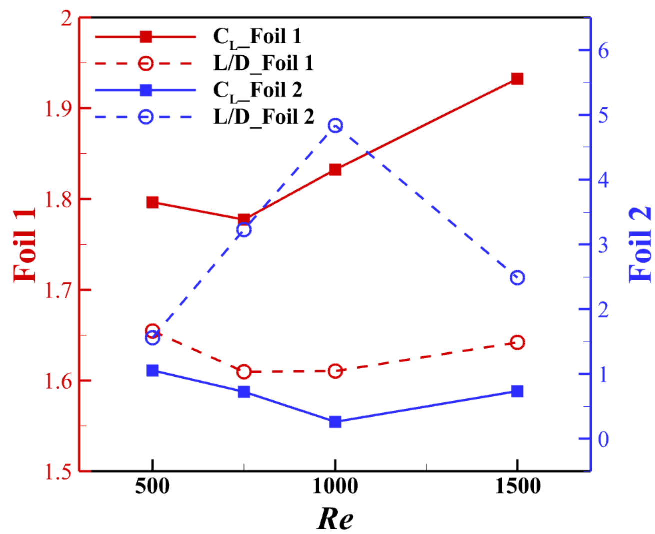

FIGURE 5.8: Aerodynamic performance of different Reynolds number at configuration Δx = 3.75c, Δy = -0.75c

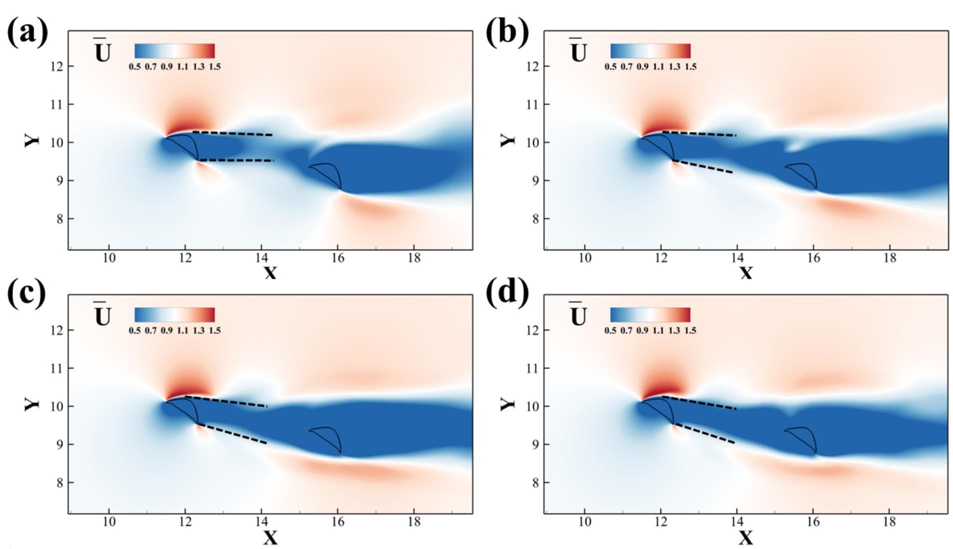

FIGURE 5.9: Time-averaged stream-wise velocity fields of two tandem flying snake airfoils under different Reynolds numbers: (a) Re= 500, (b) Re=750, (c) Re=1000, (d) Re=1500.

To further investigate the formation and interaction of the vortices near the downstream snake foil, the instantaneous vorticity contours at maximum lift production for different Reynolds number cases are presented in Figure 5.10. In Figure 5.10 (a1), (b1) and (c1), the TEV_U^2 meets the leading edge of the downstream airfoil. Different Reynolds numbers have slightly different angles of incidence and initial position, leading to different vortex-wedge interaction patterns. In Figure 5.10 (a2), the TEV_U^2 collides with the wedge (leading edge) of the downstream foil. Tucker *et al.*'s work[84] provided similar vortex-wedge interaction profiles. By shifting the initial position of the vortex downwards with the increasing of Reynolds number, the vortex breakdown switches from the dorsal surface to the ventral surface, which happens in Figure 5.10 (b2) at Re=750. As a result, TEV_U^2 distorts and merges with the shear layer on the ventral surface. At a higher Reynolds number Re=1500, the TEV_U^2 advects downstream without breaking down at the wedge. Figure 5.10 (c2) shows that it maintains its shape before merging and interacting with the TEV_D generated at the trailing edge of the downstream foil. Similar trends of position shift along with vortex breakdown have been summarized in Ref [85], [86].

Thus, the lift production is slightly reduced while the lift-to-drag ratio increases compared with Re=1000 cases. Another feature is the wider lift reduction region and the narrower high L/D region for foil 2. All the features represent the effect of Reynolds number of the wake formation from foil 1 and the vortex-body interaction for foil 2.

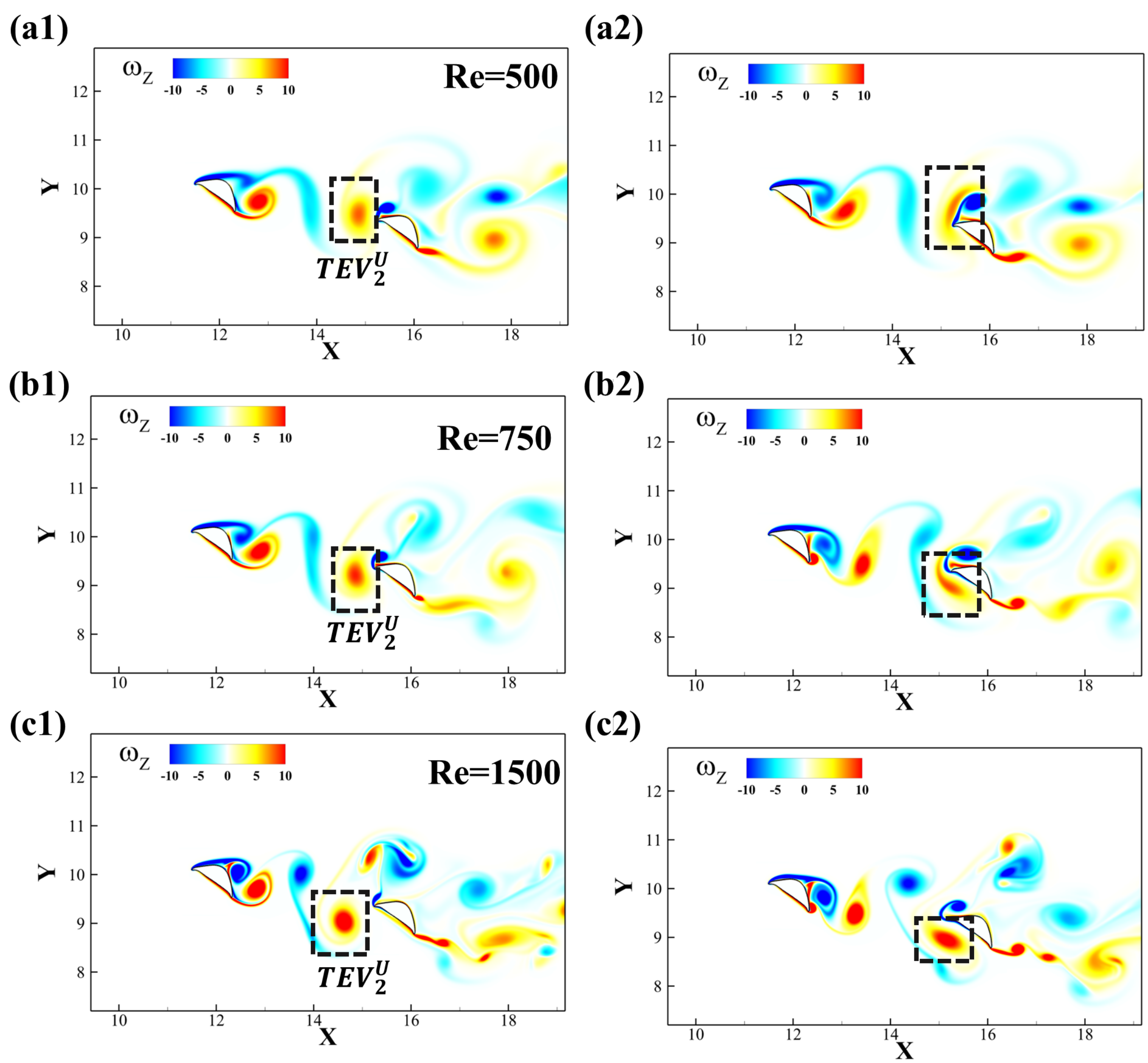

FIGURE 5.10: Vorticity contour for the configuration Δx = 3.75c, Δy = -0.75c at Re = 500, 750 and 1500 for (a), (b) and (c). (1) and (2) represent the snapshot of the maximum and minimum lift production on foil 2, respectively.

5.5 Effects of the pitching motion

In this section, the effects of the dynamic motion of the downstream snake airfoil on the system's hydrodynamic performance and wake evolution are investigated. As proposed in the methodology section, dynamic motion is applied with pitching, including different pitching amplitude and frequencies.

5.5.1 Effect of Pitching Amplitude

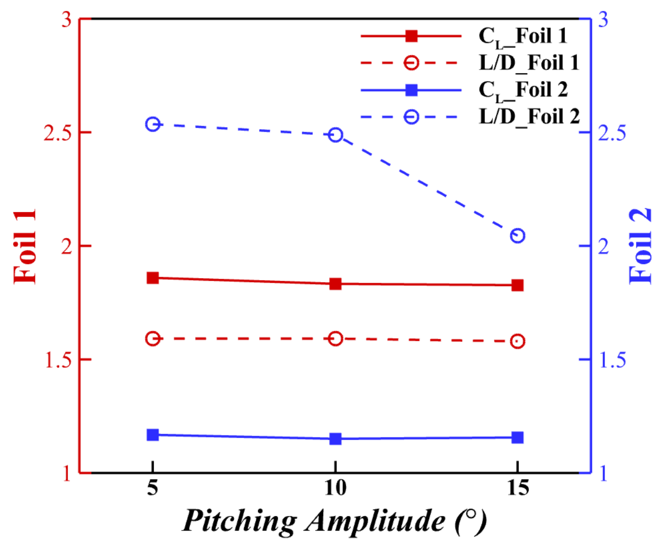

FIGURE 5.11: Aerodynamic performance of different pitching amplitudes at configuration Δx = 3.75c, Δy = -0.75c

In Fig. 5.12, it is shown that the vortex interaction between the foils is more complicated. The introduction of the pitching motion will lead to the variation of AOA on the downstream foil, which changes the vortex formation pattern on the leading edge and the trailing edge (the mean AOA=35° provides maximum lift as well as the transition of the vortex generation[43]). Meanwhile, the incident angle of the upstream vortices towards the downstream foil wedge will

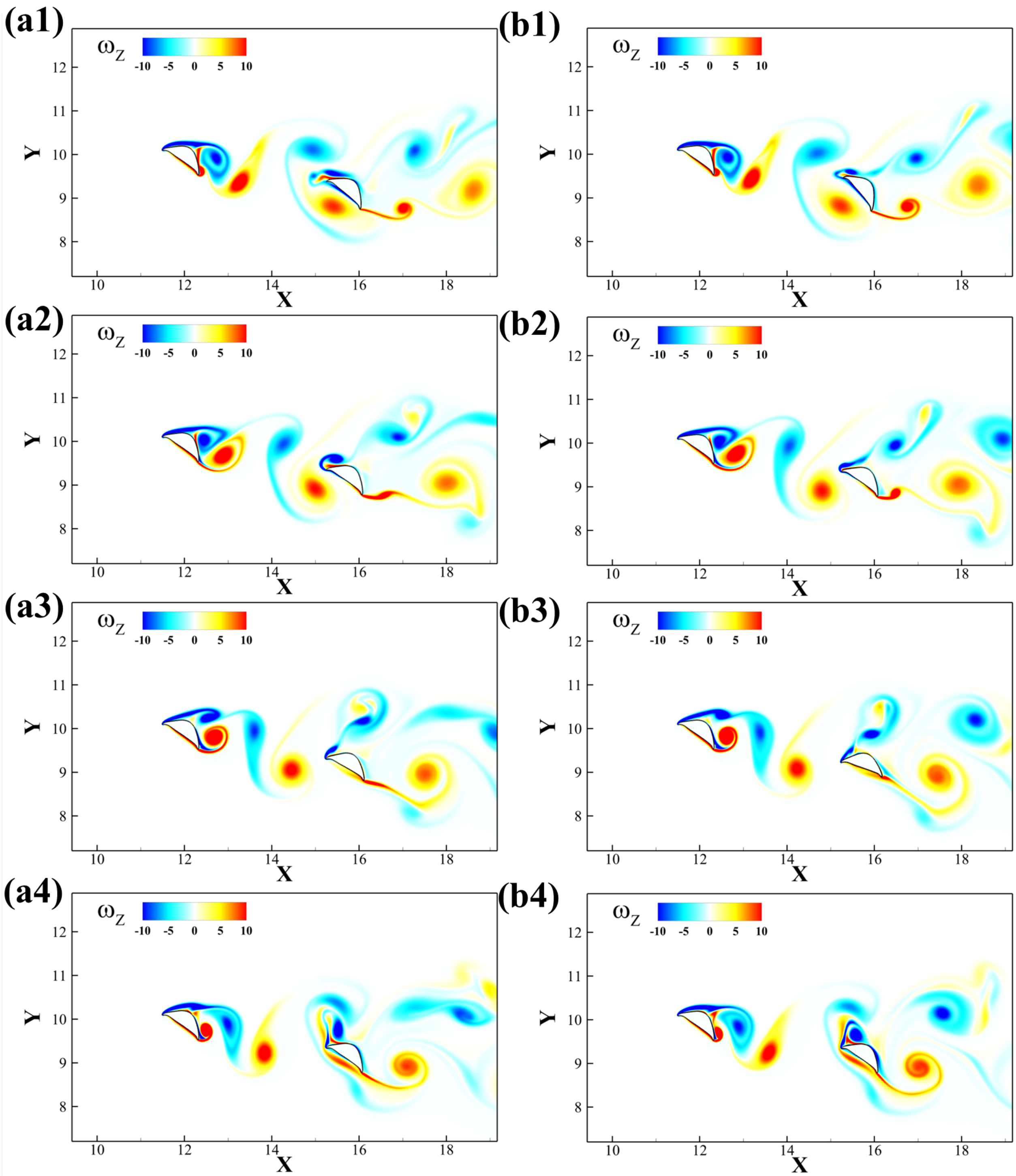

FIGURE 5.12: Evolutions of the vortex structures in one pitching period for the pitching amplitude 5° (a1 ∼ a4) and 15° (b1 ∼ b4).

constantly change. Thus, the vortex interaction between the foils becomes more complicated. Figure 5.12 presents the vortex formation process at different amplitudes 5° and 15°.

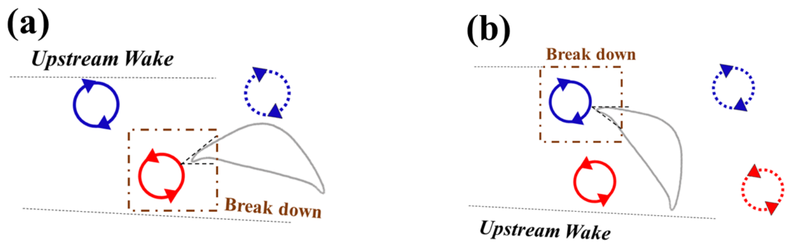

FIGURE 5.13: Schematic of vortex interaction when the downstream foil is at (a) maximum (b) minimum pitching amplitude.

In Figure 5.12 (a2) and (b2), the TEV_U^1 advects downstream to the ventral surface of the downstream foil. Due to different amplitudes, TEV_D^2 at low amplitude breaks down into a thin layer, yet high amplitude forms a compact vortex. Also, in Figure 5.12 (a4) and (b4) the LEV_D^2 merges with TEV_U^2, yet the LEV_D^2 distorts and stretches in low amplitude case.

5.5.2 Effect of Pitching frequency

In this section, the pitching frequency of the downstream foil is changed. According to the definition:

$$T = \frac{1}{2\pi f} \tag{5.5}$$

we conducted the simulation using T=1 $\sim$ 6. The time period also corresponds with the simulation time. The force history shows that the solitary foil vortex shedding period is T = 3.2 using FFT. However, with the introduction of downstream foil, the period rises to T = 4. According to previous studies, phase change affects the interaction between tandem foils. Therefore, the frequency variation will affect the vortex formation and interaction accordingly.

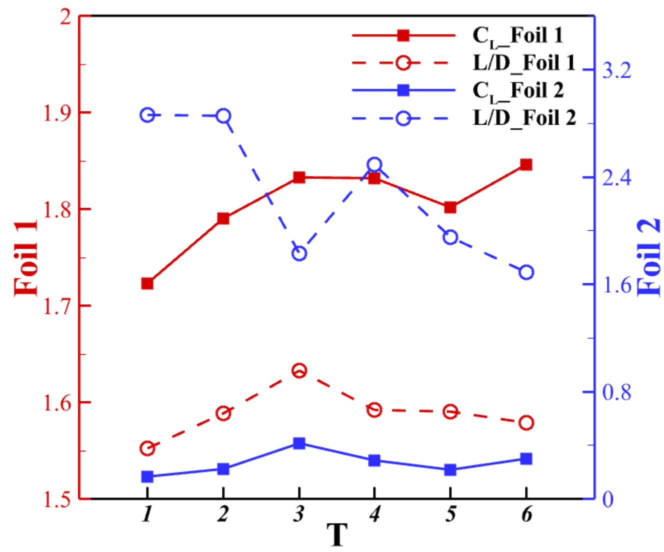

FIGURE 5.14: Aerodynamic performance of different pitching frequencies at configuration Δx = 3.75c, Δy = -0.75c

The time-averaged aerodynamic performance is presented in Figure 5.14. It is observed that for the upstream foils, the lift production and the lift-to-drag ratio will be affected by the interaction with the downstream airfoil, but only within 5 %. The downstream airfoil's performance changes significantly with the pitching frequency. At T=3, when the pitching motion is in-line with vortex shedding frequency from the upstream wake, it will provide a high lift production. Further vortex analysis shows that in Figure 5.15, the vortex interaction shows a different pattern by comparing the same time frame of peak lift. In Figure 5.15 (b) and (d), the pressure contour near the upstream foil shows a similar pattern, yet the pressure difference is higher at T=3. For the downstream foil, the pressure difference of the T=3 is even more considerable, thus leading to the 93% increase in lift production.

The vortex interaction contributes not only to lift production but also to the lift-to-drag ratio. At T=1,2 and 4, the L/D ratio of the downstream foil reaches a higher level than others. The

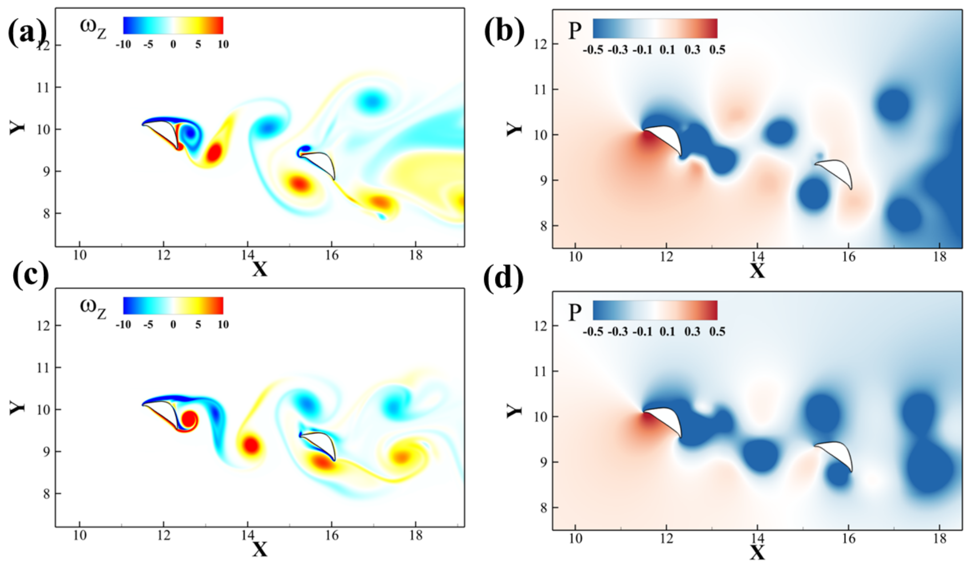

FIGURE 5.15: (a) and (b) show the instantaneous vorticity and pressure contour at T=3, respectively. (c) and (d) show the same information for T=5

picked-out cases show integer multiples of pitching frequency, where the vortex interaction is in-line with each other.

5.6 Effects of heaving motion

5.6.1 The introduction of heaving motion

In this section, the impact of dynamic motion on foil 2's aerodynamic performance and wake evolution is examined. Consistent with the methodologies outlined earlier, dynamic motion is implemented via heaving, incorporating a variety of amplitudes and frequencies.

In this section, the effect of dynamic motion of the foil 2 on the system's aerodynamic performance and wake evolution are investigated. As proposed in the methodology section, the dynamic motion is applied with heaving, including different heaving amplitudes and frequencies.

To start with, the amplitude $\Delta H_m = 0.1c$ and heaving period $T = 3.2t^*$. The heaving period is calculated based on the fast Fourier transform (FFT) analysis of the force history in the steady case. This period corresponds with the vortex shedding frequency from foil 1 and it also agrees with the peak-to-peak time period in lift and drag generation. The motion of heaving has been sketched in the schematic plot in Figure 5.1.

We first present the force history of the two foils as investigated in the steady case in Figure 5.16. In this figure, the force generation of foil 1 has shown a similar trend as the steady case. The force production is also consistent with the heaving frequency. However, the lift generation peak value of foil 2 has shown a higher value than foil 1, which is different from the steady case. We picked four time frames of $t/T = 7.10, 7.31, 7.62, 7.85$, representing the two troughs and two peaks of foil 1 and foil 2 to investigate the vortex formation difference (see Figure 5).

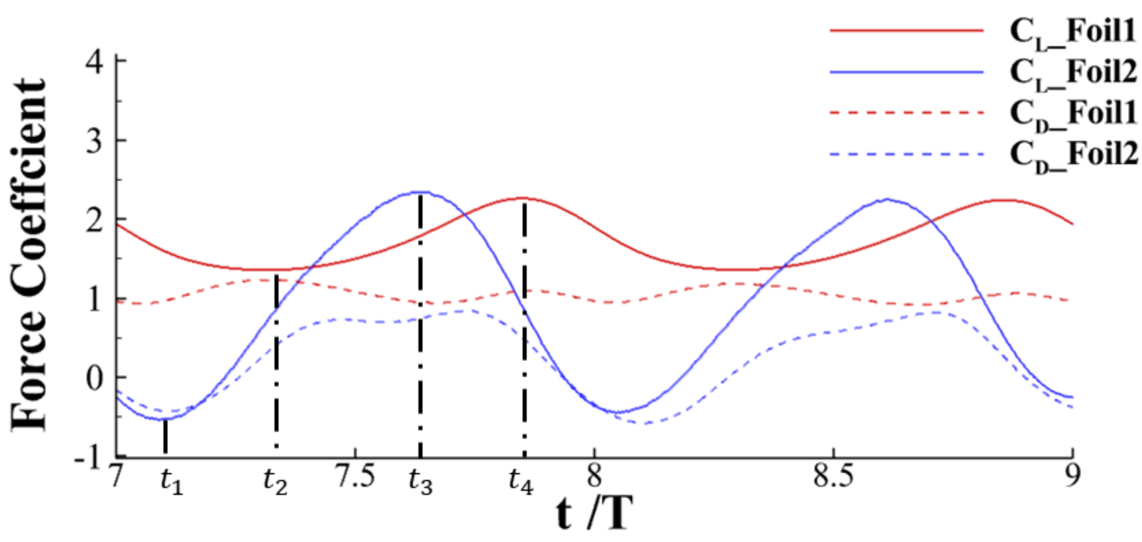

FIGURE 5.16: Instantaneous force history of the case with heaving motion. The time axis has been normalized with heaving motion period $T = 3.2t^*$.

In Figure 5.17, the vorticity and pressure contour at four time frames are presented. At $t_1 =$

$7.10T$, the TEV from foil 1 propagated to the ventral surface of foil 2. There are two low-pressure regions on both sides of foil 2 (Figure 5.17 (a1) (b1)). Similarly, the low-pressure region reached the trailing edge of foil 1 (Figure 5.17 (b2)) where the new TEV is generating (Figure 6 (a2)). This will reduce the pressure difference on the trailing edge thus provide a lift production trough.

For $t_3 = 7.62T$ and $t_1 = 7.84T$, high lift production is observed on foil 2 and foil 1. The mechanism for high lift production is similar for both foil 1 and foil 2, as indicated in Figure 5.17 (c2) and (d2). The attachment of the shear layer on the ventral surface, while the TEV sheds off the trailing edge, provides a high-pressure region, whereas the attachment of the LEV on the dorsal surface results in a low-pressure region. These conditions account for the peak lift production on the foils. Simultaneously, the foils experience peak drag production due to the angle of attack, such that the pressure difference provides both x and y components. The difference in LEV formation on foil 1 and 2 results from both vortex interaction and the heaving motion. In Figure 5.17 (d1), the vortex formed on the leading edge is stretched, forming a long shear layer. Meanwhile, in Figure 5.17 (c1), since foil 2 is heaving downwards, the LEV on the leading edge can maintain its shape before shedding off.

5.6.2 Effect of heaving amplitude

The heaving amplitude is defined by the vertical displacement of the foil, which can be modulated by altering the posterior body's dorsal-ventral bending. By incorporating equation 1, the downstream foil's vertical position varies constantly. Figure 5.18 presents the aerodynamic performance, showing that as the amplitude increases, lift production on foil 1 slightly decreases

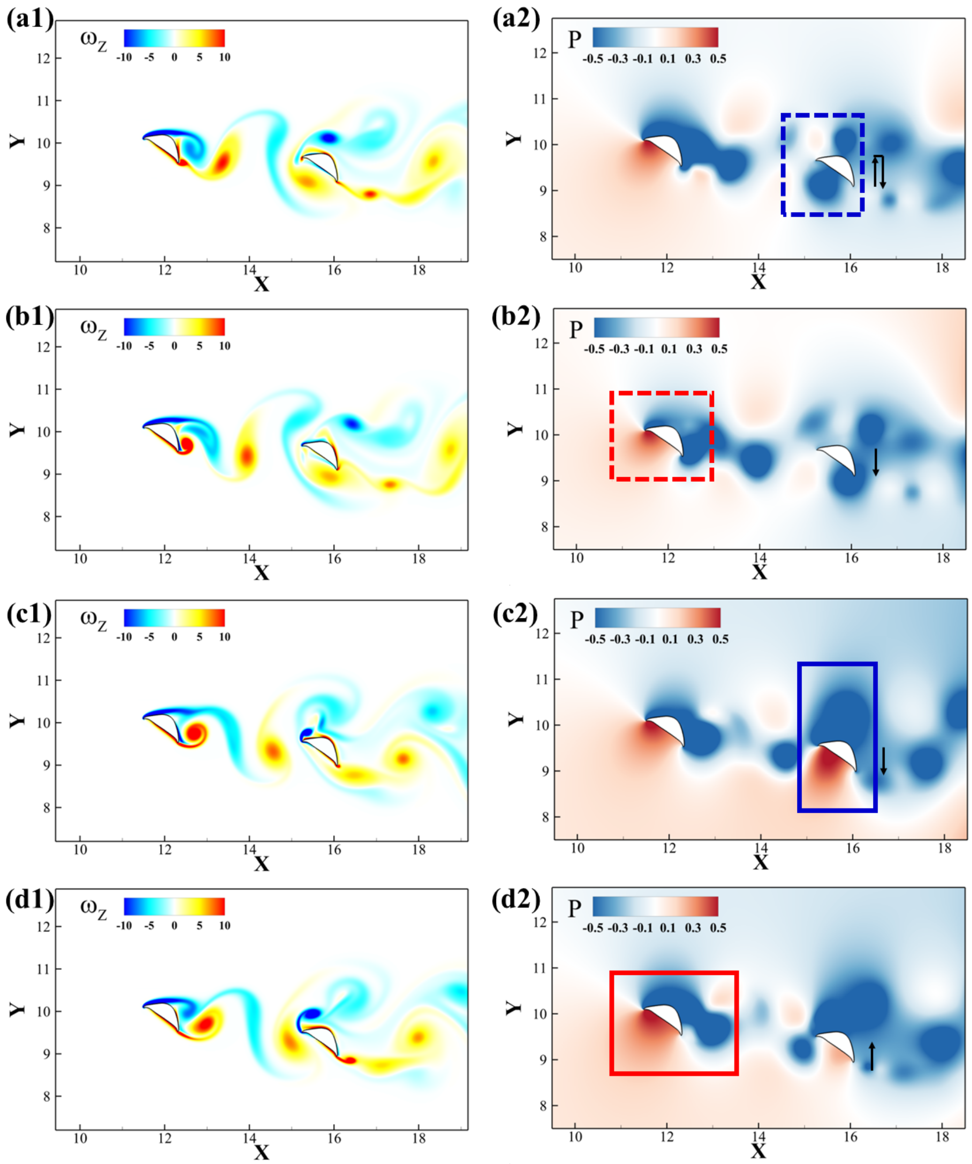

FIGURE 5.17: At (a) $t_1 = 7.10T$, (b) $t_2 = 7.31T$, (c) $t_3 = 7.62T$, and (d) $t_4 = 7.84T$, the evolution of the (1) vortex structures and (2) pressure contour are presented over one complete heaving period. The time frames are selected based on trough and peak lift production instances for foil 1 and foil 2, as indicated in the force history shown in Fig. 5.16.

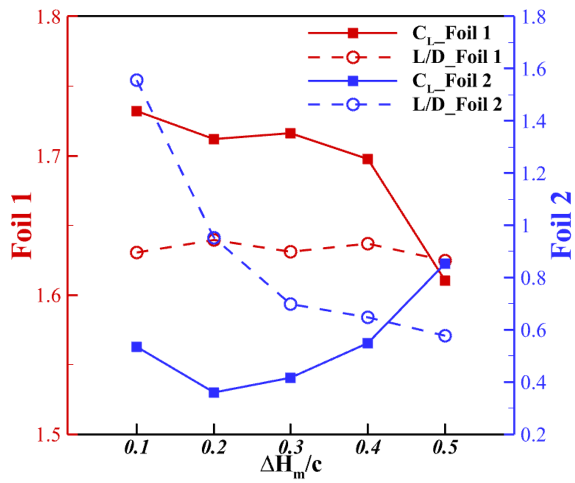

FIGURE 5.18: Cycle-averaged lift coefficient and lift-to-drag ratio at different heaving amplitudes (ΔH_m).

due to foil 2's instability. Conversely, foil 2 experiences an increase in lift production after surpassing a minimum value at $\Delta H_m = 0.2$. However, this increased lift production results in decreased efficiency, as indicated by the rapid decline in the lift-to-drag ratio for foil 2. It suggests that the snake might employ high amplitude heaving motions to enhance lift generation on foil 2, providing a counter-clockwise moment to the two-foil system, aiding in pitch maneuvers.

Fig. 5.19 illustrates that higher heaving amplitudes of foil 2 lead to more complex vortex formations. The heaving motion alters the vortex formation patterns on foil 2's leading and trailing edges by changing the effective angle of attack, and also affects the incidence angle of upstream vortices towards the downstream foil. Consequently, the vortex interaction between the foils becomes more intricate. Fig. 5.19 displays the vorticity and pressure contours, as well as cycle-averaged stream-wise velocity for amplitudes $\Delta H_m = 0.3c$ (a) and $0.5c$ (b). At smaller amplitudes, LEV and TEV from foil 1 collide with foil 2's wedge, while the shear layer on foil 2's leading edge remains attached. However, at higher amplitudes, the stronger LEVs merge with foil 1's TEVs, deviating from low amplitude cases where TEVs merged into the shear layer on the ventral surface. Instead, they collide with the edge and, due to high unsteadiness, break into two smaller vortices. The upper vortex merges with foil 2's LEV and propagates downstream with an upward deviation, while the lower vortex remains beneath the airfoil. The motion of foil 2 determines whether the wedge collides with the upper or lower surface, leading to different vortex-wedge interaction profiles as summarized in Ref [84], [86].

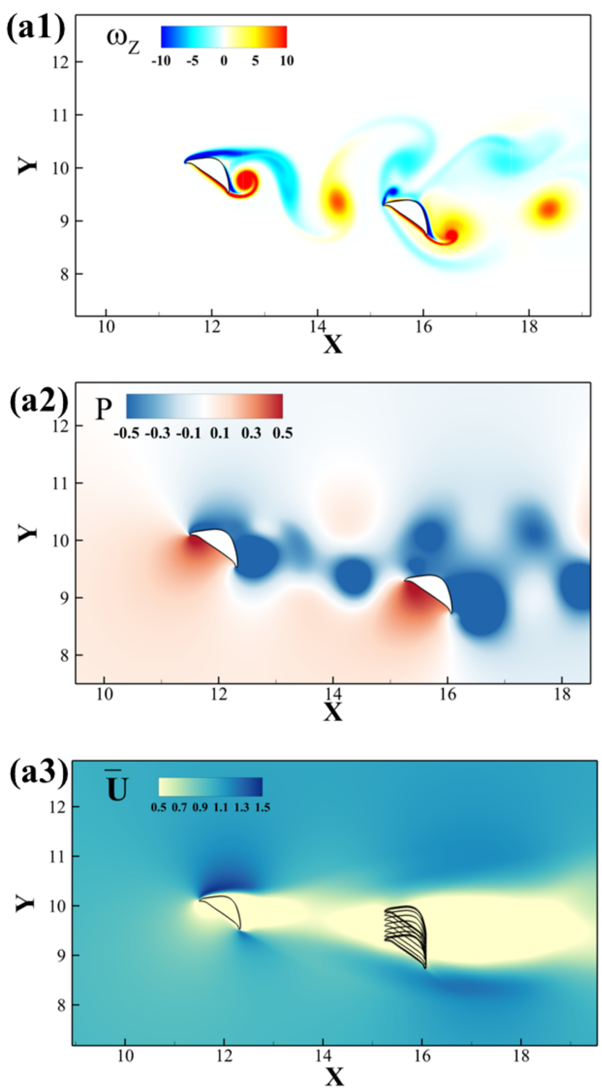

FIGURE 5.19: At $\Delta H_m = 0.3c$ and $\Delta H_m = 0.5c$, the vortex structures (a), pressure contour (b), and time-averaged stream-wise velocity (c) are depicted. The vortex and pressure contours are selected at the peak lift time frame.

Also, this leads to higher pressure difference at higher amplitude(Figure 5.19 (a2) and (b2)). The wake information shown in Figure 5.19 (a3) and (b3) showed that the more substantial heaving motion leads to the wake deflection. The vortex formation will be more complicated and the induced vortex pair actually increased the drag production as well.

5.6.3 Effect of heaving frequency

In this section, we explore the effect of varying the heaving frequency of the downstream foil. Following the relationship defined as $T = \frac{1}{f}$, we adjust the co-frequency value of $T = 3.2t^*$ to integer periods to facilitate clearer results. Lower period values correspond to higher frequencies. For simplicity in discussion, $T = 3.0$ is used to denote the original value of $T = 3.2t^*$.

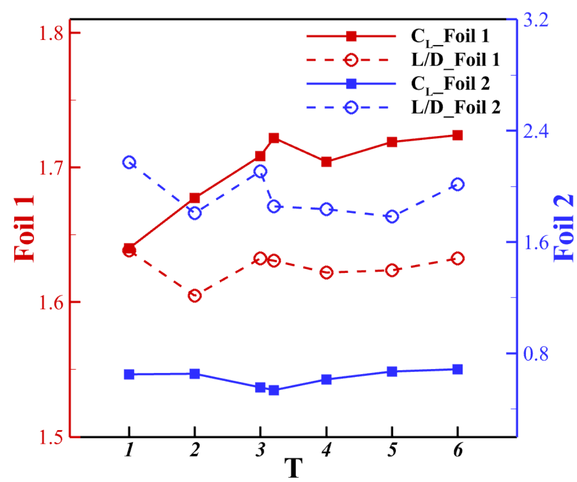

FIGURE 5.20: Cycle-averaged lift coefficient and lift-to-drag ratio at different heaving periods T ($T = \frac{1}{f}$).

The cycle-averaged lift coefficient and lift-to-drag ratio are presented in Figure 5.20. The data indicate that a decrease in the heaving frequency results in an increase in lift generation for both foils. Notably, when the co-frequency aligns closely with the vortex shedding period, a significant enhancement in the lift-to-drag ratio is observed. Specifically, $T = 1, 3$, and 6 correspond to approximately $1/3, 1$, and 2 times the vortex shedding period, respectively.

Figure 5.21, featuring $T = 1.0$ and $T = 6.0$, delves into the vortex dynamics. The vorticity and pressure contours are illustrated at the peak lift production timeframe. Given that the lift values differ by less than 10%, the mechanisms of lift production are presumed to be similar across frequencies. As shown in Figure 5.21 (a1) and (a2), the presence of the shear layer on the ventral surface and the leading-edge vortex (LEV) on the dorsal surface contribute to a significant pressure differential, marked by high and low-pressure regions. The unsteadiness of the motion leads to fragmentation of the vortex structure near foil 2's leading edge, resulting in the formation of two secondary vortices. One aligns with the LEV, and the other positions beneath foil 2, merging into the shear layer. The varying heaving frequencies represent two extremes: a larger period (lower frequency) resembles a more steady system, while a shorter period (higher frequency) introduces both higher lift production and increased unsteadiness. The wake patterns further support this observation, with a wider wake at $T = 1.0$ compared to $T = 6.0$, indicating that higher heaving frequencies contribute to more unstable vortex patterns and divergent propagation of vortex pairs.

5.6.4 Expansion to three foils

In this final section, we extend the analysis from a two-foil configuration to a three-foil system, adopting the parameters $L = 3.75c$ and $H = -0.5c$, akin to those used in horizontal undulation studies [66]. This expansion is also prompted by the observation of three distinct sections in some aircraft configurations.

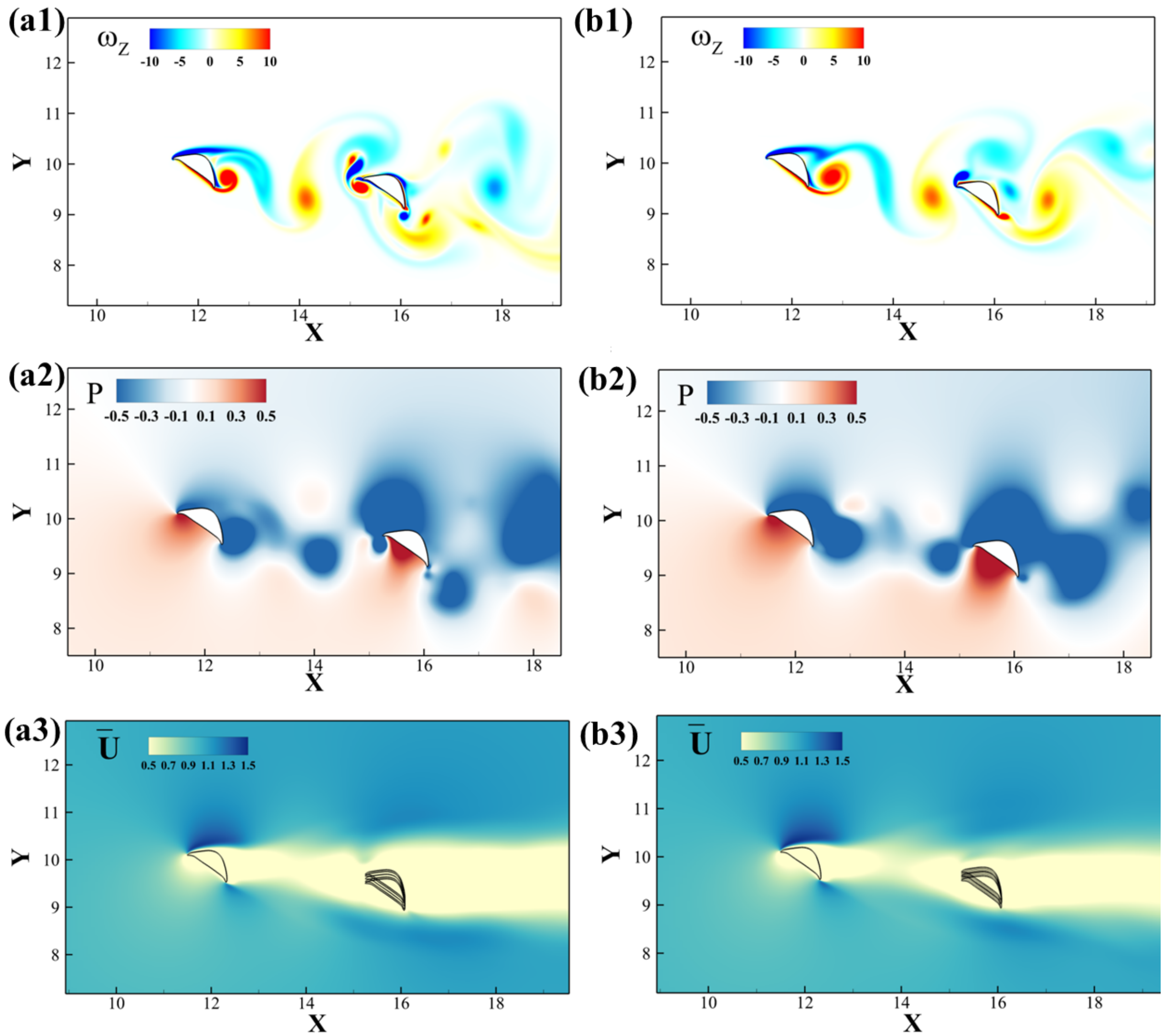

FIGURE 5.21: At (a)T = 1.0 and (b)T = 6.0, the (1) vortex structures, (2) pressure contour and (3) time-averaged stream-wise velocity are presented. The vortex and pressure contour are chosen at peak lift time frame.

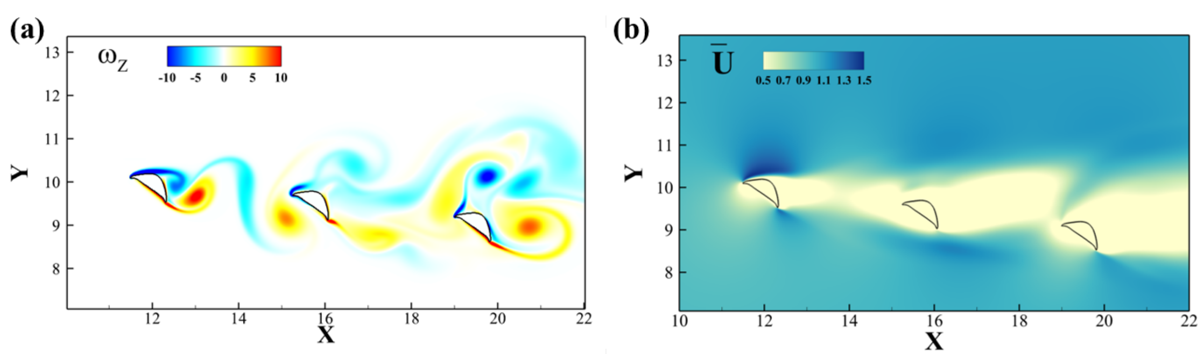

FIGURE 5.22: (a)Vortex dynamics of three foils. (b) Time-averaged stream-wise velocity.

	C_L	C_D	L/D
Foil 1	1.7210	1.0501	1.6389
Foil 2	0.6777	0.2805	2.4160
Foil 3	1.2961	0.6656	1.9473

TABLE 5.1: Aerodynamic performance of three steady tandem foils at configuration $L = 3.75c$ and $H = -0.5c$

The aerodynamic performance of the three-foil system exhibits patterns similar to those observed in the two-foil setup. Typically, when downstream foils are situated within the wake of an upstream foil, they experience vortex-induced effects leading to a reduction in lift and an enhancement in the lift-to-drag ratio (L/D). For the second and third foils, both exhibit lower lift production compared to the first foil, yet their L/D ratios surpass that of the first foil. It's noteworthy, however, that the average lift coefficient (C_L) for the third foil is 1.2961, which is superior to the second foil's performance, and its L/D ratio of 1.9473 is slightly inferior to that of the third foil.

Vorticity contours and time-averaged velocity fields are illustrated in Figure 5.22 to further elucidate the distinctions among the foils. The leading-edge vortex (LEV) interaction near the third foil's leading edge is markedly more pronounced than that of the second foil. The LEV shed from the second foil amalgamates with the LEV on the third foil and detaches from its dorsal surface, leading to a unique vortex interaction pattern. The wake pattern, particularly after the second foil as shown in Figure 5.22 (b), reveals an upward deviation, indicating that the wake-foil interaction for the third foil diverges from that of the first two foils.

Future investigations will delve deeper into the three-foil configuration, examining the effects of dynamic motion and various configurations on the aerodynamic interactions and performance.

This research aims to shed light on the intricate dynamics of tandem foil interactions and optimal body arrangements for multi-body gliding robots, with the ultimate goal of enhancing their aerodynamic efficiency.

5.7 Conclusions and discussion

This section presents the numerical simulation of a two tandem-airfoil model, which was inspired by the cross-section of a flying snake. A thorough investigation of the aerodynamic performance of the upstream and downstream airfoil was conducted. We conducted a more detailed investigation of the parameters associated with the relative position configuration, the Reynolds number and the effect of dynamic motion in our study. The detailed analysis has revealed the structure of the vortex, which includes the leading-edge vortex (LEV) and trailing-edge vortex (TEV). Additionally, the interaction between the wake of the tandem airfoils has been studied.

Compared with solitary snake airfoil, the performance of the two-foil system was influenced by the relative positions of the foils for all conditions considered. For the upstream foil, the change was relatively small and it could outperform or underperform relative to the solitary foil depending on the relative spacing. The downstream foil experienced a significant decline in performance when it was located in the upstream foil wake. Due to the interaction, the downstream foil experiences lift reduction by 86.5% and the drag reduction by 96.3%. Thus, the lift-to-drag ratio increased by 377% compared to a single foil. The system performance is following the same pattern as the downstream foil.

The results of flow field analysis showed that the lift-to-drag ratio of the downstream foil would be maximized when it was situated in the wake of the upstream foil. The lift and drag production will both be reduced as a result of the interaction between the vortex-wedge and the pressure differential between the dorsal and ventral surfaces will be substantially minimized when the vortex is break down and merged into the ventral surface. As a result, the posterior body of the snake sacrifices lift production to reach higher efficiency in gliding. Further study changing the Reynolds number revealed that the flow structure would be similar by increasing the *Re*. It will primarily affect the strength of the vortices and also lead to the deviation of the wake. When the Reynold number increases, the best-performed region shift downwards and the downstream foil need to move accordingly to optimize its performance.

The two-foil steady system has been augmented with a downstream pitching foil, and the aerodynamic performance and vortex dynamics of it have been studied. The aerodynamic performance of the system and the corresponding vortex wakes vary in accordance with the pitching amplitude and frequency, owing to the phase modification of the vortex capture. When the shed vortex travels downstream to the posterior foil, the motion of the leading edge alters the pattern of interaction between the vortex and wedge, depending on the phase. When the vortex shedding lines up with the dynamic pitching motion, the production of the lift will augment through the introduction of a movement with the proper amplitude and frequency, however, the L/D efficiency will be compromised.

By applying heaving motion into the best performed two-tandem-configuration, higher lift production while maintaining high L/D can be achieved by carefully choosing heaving amplitude and frequency.The increase of heaving amplitude brings higher lift production at the cost of gliding efficiency. By adjusting the heaving frequency to be consistent with the vortex shedding, the foil 2 in the downstream can take more advantage from the upstream wake.

Detailed analysis has revealed the vortex structure and the wake interaction between the tandem foils, which showed some significant difference between steady and dynamic systems. The motion changes the interaction between the wake and the leading edge of foil 2 in the downstream.

6 Conclusions

6.1 Summary of Contributions

6.1.1 Concluding remarks

This investigation will then extend to analyzing flow around 3D models demonstrating horizontal undulations and vertical bendings, to unravel the underlying flow physics.Furthermore, the research will delve into a detailed examination of two snake cross-sections arranged in a 2D space, providing a fundamental understanding of the interaction mechanisms between different body segments of the snake during gliding. Real snake models will also be employed to examine the aerodynamic benefits contributed by the motion of the head and tail, aspects often overlooked in prior studies.This research will encompass a wide range of facets related to snake gliding, including various motion types, undulating frequencies, angles of attack, Reynolds numbers, spatial arrangements in 2D, and dynamic motion frequencies. An integrated approach, combining high-fidelity 3D surface reconstruction with computational fluid dynamics, will be employed to fill the gaps in understanding the aerodynamics of flying snake gliding.Upon completion, this dissertation is expected to unveil the 3D vortex formation in flying snake gliding, marking the first study of its kind. It will reveal the LEV concentration mechanism on a curved moving body in horizontally undulating flying snakes, and analyze the effect of Reynolds number, undulating frequency, and angle of attack on the aerodynamics of snake gliding. The study will also investigate the vortex-body interaction between snake body segments and its link to aerodynamic performance, and explore the control of aerodynamic moments by adjusting interactions in snake body segments arranged in three-dimensional space.

Chapter 3 numerically studies the flow dynamics of aerial undulation of a snake-like model, which is adapted from the kinematics of the flying snake (*Chrysopelea*) undergoing a gliding process. The model applies aerial undulation periodically in a horizontal plane where a range of angle of attack (AOA) is assigned to model the real gliding motion. The flow is simulated using an immersed-boundary-method-based incompressible flow solver. Local Mesh Refinement (LMR) mesh blocks are implemented to ensure the grid resolutions around the moving body. Results show that the undulating body produces the maximum lift at 45° of AOA. Vortex dynamics analysis has revealed a series of vortex structures including leading-edge vortices (LEV), trailing edge vortices (TEV), and tip vortices (TV) around the body. Changes in other key parameters including the undulation frequency and Reynolds number are also found to affect the aerodynamics of the studied snake-like model, where increasing of undulation frequency enhances vortex steadiness and increasing of Reynolds number enhances lift production due to the strengthened LEVs.

Chapter 4 presents a numerical investigation into the aerodynamic characteristics and fluid dynamics of a flying snake-like model employing vertical bending locomotion during aerial undulation in steady gliding. In addition to its typical horizontal undulation, the modeled kinematics incorporates vertical undulations and dorsal-to-ventral bending movements while in motion.

Using a computational approach with an incompressible flow solver based on the immersed-boundary method, the study employs Local Mesh Refinement (LMR) mesh blocks to ensure the high resolution of the grid around the moving body. Initially, we applied a vertical wave undulation to a snake model undulating horizontally, investigating the effects of vertical wave amplitudes (ψ_m) and dorsal-ventral bending amplitudes (ψ_{DV}). The vortex dynamics analysis unveiled alterations in leading-edge vortices (LEV) formation within the midplane due to changes in the effective angle of attack resulting from vertical bending, directly influencing lift generation. Our findings highlighted peak lift production at $\psi_m = 2.5^\circ$ and the highest lift-to-drag ratio at $\psi_m = 5^\circ$, with aerodynamic performance declining beyond this threshold. Subsequently, we studied dorsal-ventral bending, revealing a tail-up/down posture that influenced interactions between body segments. A 5° dorsal-ventral bend increased lift by 17.3% but reduced gliding efficiency, showing reverse effects with $\psi_{DV} = -5^\circ$. This study explains the flow dynamics associated with vertical bending and uncovers fundamental mechanisms governing body-body interaction, contributing to the enhancement of lift production and efficiency of aerial undulation in snake gliding.Chapter 4 also explores the aerodynamic mechanisms underpinning the rolling control of flying snakes during gliding flight. The ability of these creatures to maintain stability without static wings is a phenomenon that has puzzled researchers. Our numerical study simulates the aerodynamics of a flying snake's body, both static and in motion, to understand the forces that contribute to rolling stability. We find that a static snake model, due to the asymmetry inherent in its shape, cannot maintain rolling stability, as the unbalanced rolling moments lead to an unstable flight trajectory.

However, when horizontal undulation is introduced, the dynamic motion of the body balances these moments. This constant undulatory movement redistributes the aerodynamic forces along the body, offering a means to counteract instabilities. While this dynamic balance does not yield a static equilibrium, it provides an effective averaged moment to counteract rolling deviations. The addition of vertical undulation further enhances stability by introducing span-wise velocity components, which stabilize vortex formation along the body. Our results demonstrate that in response to small roll perturbations, the system generates a restorative negative moment, effectively returning the snake to a neutral position. This discovery has significant implications for the design of bio-inspired robotic systems that utilize undulatory locomotion for stable flight without the need for static wing structures. The rolling control mechanisms identified in this study illuminate a path toward more agile and adaptive aerial robots.

Chapter 5 investigates the interaction when flying snakes adopt an S-shaped posture, flattening their ribs to create an airfoil-like cross-section, impacting their aerodynamic performance due to the interaction between body segments using numerical simulations on two-dimensional snake cross-sectional airfoils. Employing an immersed-boundary-method flow solver with direct numerical simulation and tree-topological local mesh refinement, the study analyzes different body positions and movements. Findings reveal a decrease in lift production by 86.5% and a 96.3% drop in drag when the downstream body aligns with the upstream foil. This alignment leads to a 377% lift-to-drag ratio increase compared to a single foil, attributed to vortex-wedge interaction. Although it enhances posterior body gliding efficiency by balancing lift reduction, specific pitching motion integration with coordinated vortex shedding can further optimize lift production. The heaving motion have shown lift change with the wake capture for the downstream body. Results from this study will bring detailed knowledge of flying snakes' gliding mechanism and control and provide inspiration for bio-inspired robots designing from an aerodynamic perspective.

Through our research, the leading edge vortex (LEV) is the key thread which connects the flow physics and the aerodynamic performance appearing in all different kinematics in flying snake gliding.

- LEV contributes to the lift production.The LEV attachment to the dorsal surface of the body brings the low pressure region on the top. It brings the pressure force difference which contributes the components of lift and drag.

- The 3D steady shape brings change to the LEV formation. The straight portion of the body forms the strong LEV while the curved portion of the body didn't encounter the flow directly.

- The horizontal undulation with span-wise motion introduces the temporal-spacial evolution of LEV, which deforms the vortex topology to be a oblique vortex tube near the leading edge.

- Less portion of the body can maintain LEV attachment, while the turning motion stabilized the LEV. This is reflected on the lift concentration on the curved on the snake body.

- The vertical bending motion affects the effect of angle of attack on the body which affects the LEV strength.The force concentration on the curved on the snake body enhances so that produces stronger recovery rolling moment.

- The intra-body interaction between segments is the LEV-edge interaction between the anterior and the posterior body. Changing configurations or motion will affect the LEV collision pattern with the posterior foil edge which affect the vortex structure near the body.The full collision breaks down the LEV on the dorsal surface and provides less lift and drag, which increases overall L/D (efficiency).

6.1.2 Contributions and and means of dissemination

This research aims to systematically explore the aerodynamic interactions and mechanisms enhancing performance in flying snake gliding, focusing on the effects of horizontal and vertical undulations on aerodynamic performance through the use of 2D and 3D model.The study will initiate with the application of prescribed undulation kinematics to a snake model to simulate the natural gliding behaviors observed in flying snakes.

To the best of the author's knowledge, this study is

- The first to unveil the 3D vortex formation in flying snake gliding.
- The first to unveil the LEV concentration mechanism on a curved moving body in the horizontal undulating flying snake.
- The first to study the effect of Reynolds number, undulating frequency, and angle of attack on the aerodynamic performance of snake gliding.

- The first to deeply explore the aerodynamic moment control by adjusting undulation posture.
- The first to analyze the vortex-body interaction between segments of snake bodies and link the interaction to aerodynamic performance.

The findings will be disseminated in journal papers, conference proceedings, and presentations to the scientific community.

Journal publications

- Gong, Y., Wang, J., Zhang, W., Socha, J. J., & Dong, H. (2022). Computational analysis of vortex dynamics and aerodynamic performance in flying-snake-like gliding flight with horizontal undulation. *Physics of Fluids*, 34(12), 121907.
- Gong, Y., Huang, Z., & Dong, H. TVertical Bending and Aerodynamic Performance in Flying Snake-Inspired Aerial Undulation. *Bioinspiration & Biomimetics* (Under Review).

Journal articles under preparation

- Gong, Y., He, A. & Dong, H. Numerical analysis of the interaction between two tandem flying snake foils with pitching motion. Target: *Biomemetics MDPI*. (Under process)

Conference proceedings and presentations

- Zhang, W., Pan, Y., Gong, Y., Dong, H., & Xi, J. (2021, August). A Versatile IBM-Based AMR Method for Studying Human Snoring. In *Fluids Engineering Division Summer Meeting* (Vol. 85284, p. V001T02A039). American Society of Mechanical Engineers.

- Gong, Y., Wang, J., Socha, J., & Dong, H. (2022). Aerodynamics and flow characteristics of a flying snake gliding with undulating locomotion. In *AIAA SCITECH 2022 Forum* (p. 1054).

- Gong, Y., & Dong, H. (2023). Computation study about the interaction between the tandem flying snake airfoils with dynamic motion. In *AIAA SCITECH 2023 Forum* (p. 2460).

- Gong, Y., Wang, J., Zhang, W., Socha, J., & Dong, H. (2023). Numerical Investigation of Flow Dynamics in Gliding Snake-Like Models: Vortex Structures and Aerodynamic Performance.

6.2 Future Work

The proposed research systematically studies the aerodynamic interactions and performance enhancement mechanisms in flying snake gliding. Specifically, the effect of horizontal and vertical undulation on aerodynamic performance will be studied with 3D model. The flying snake's gliding mechanism, however, is still undiscovered. Some of the future work is listed below to provide some inspirations for the following researchers:

- In the current work, the horizontal and vertical bending motion are prescribed. However, in the process of landing to the ground, there will be take-off, acceleration, steady gliding and landing stages. In the earlier stages, the snake was more like a straight body than curved in the S shape. We could dynamically change the horizontal and vertical undulation amplitude combinations. This would mimic the transition from straight posture to bending posture and investigate the flow dynamics change during this process.

- By testing multiple combinations of horizontal and vertical bending amplitudes, we could choose the optimal for the best gliding performance.

- Free falling computational solver can be applied to test the real gliding process and whether it can maintain high lift and stay stable.

- A more realistic snake models will be examined.The aerodynamic benefits of the head and tail should be explored since the current undulation model didn't include this parts.The wide range of parameters such as the size and shape of the head, the length and waving motion of the tail should be included.

With an integrated approach combing high-fidelity 3D surface reconstruction and real snake motion, and computational fluid dynamics simulation, more and more undiscovered fluid mechanisms in flying snake gliding will be presented and analyzed in the future.

A Kinematics of the undulating flying snake model

This appendix shows the kinematics of different undulating flying snake models with corresponding top, side and perspective views for the first half of the cycle.

A.1 Model 1: Pure horizontal undulating model

A.2 Model 2: Vertical wave undulating model

A.3 Model 3 & 4: Dorsal-ventral bending undulating model

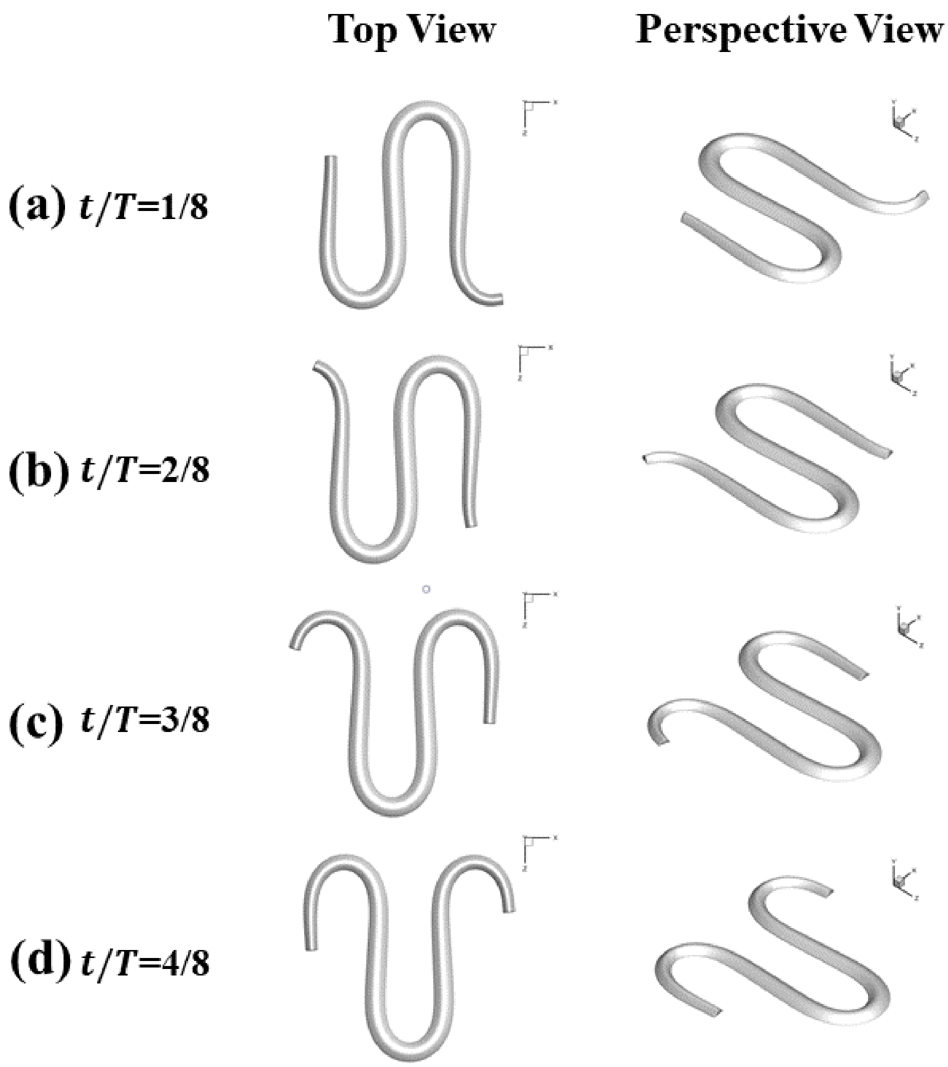

FIGURE A.1: Top and perspective view for the pure horizontal undulating model (Model 1: $\theta_m = 93^\circ$ and $\nu_\theta = 1.4$). at (a) t/T=1/8, (b) t/T=2/8, (c) t/T=3/8 and (d) t/T=4/8, respectively.

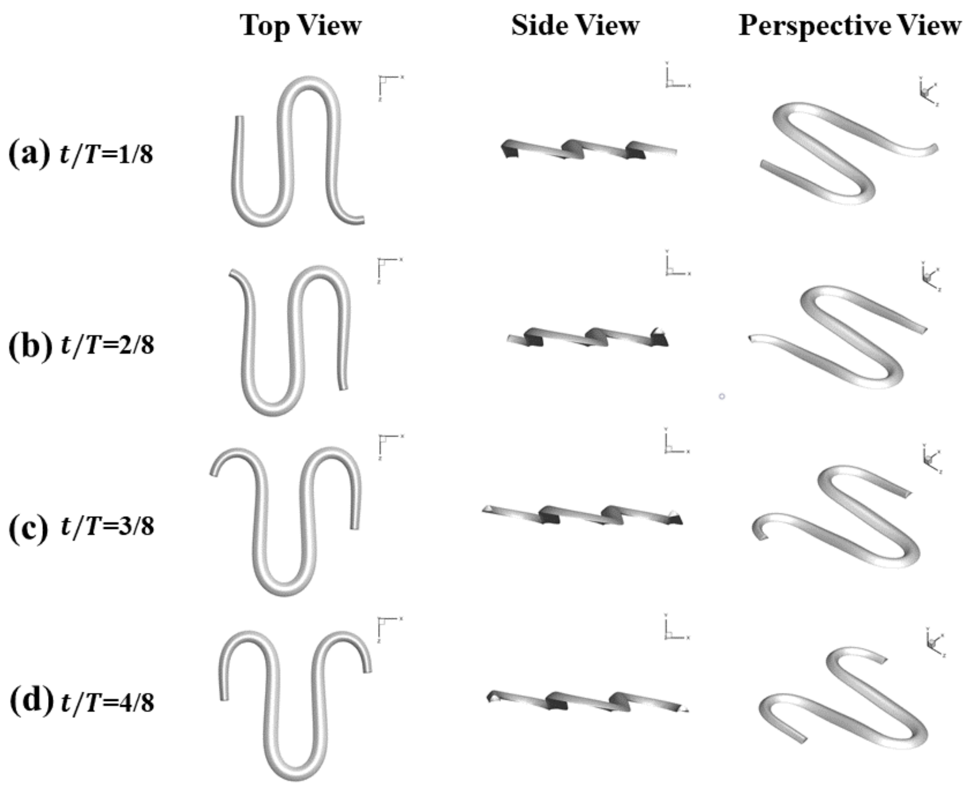

FIGURE A.2: Top, side perspective view for the vertical wave undulating model (Model 2: $\psi_m = 10°$) at (a) t/T=1/8, (b) t/T=2/8, (c) t/T=3/8 and (d) t/T=4/8, respectively. The horizontal undulation is not changed.

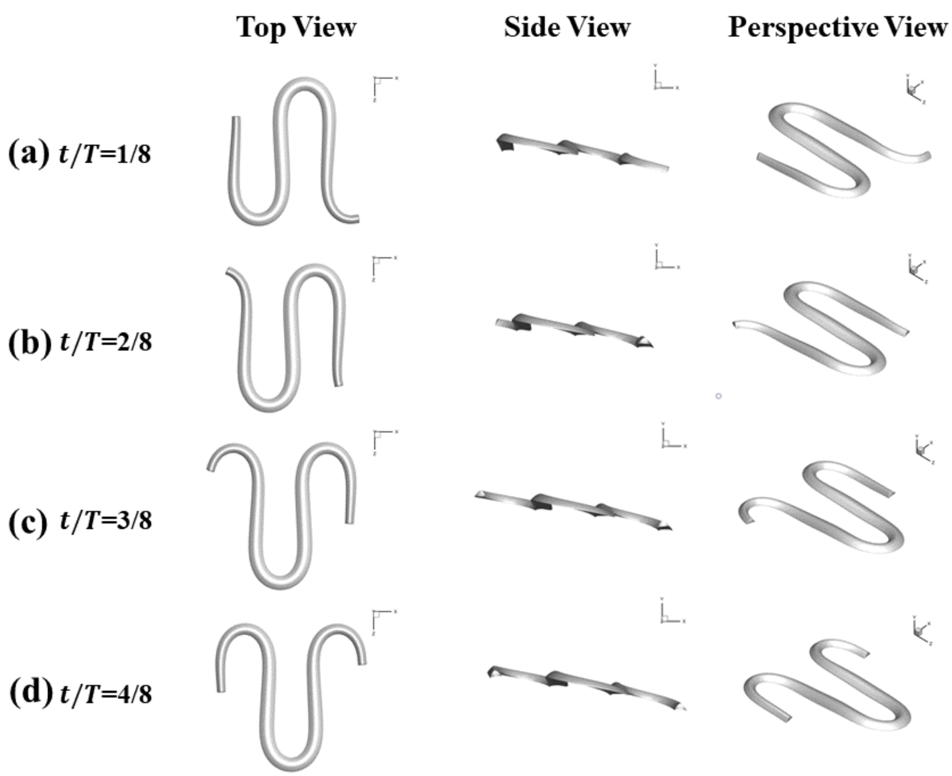

FIGURE A.3: Top, side perspective view for the dorsal-ventral bending model (Model 3: $\psi_{DV} = +5°$) at (a) t/T=1/8, (b) t/T=2/8, (c) t/T=3/8 and (d) t/T=4/8, respectively. The horizontal undulation and the vertical wave undulation are not changed.

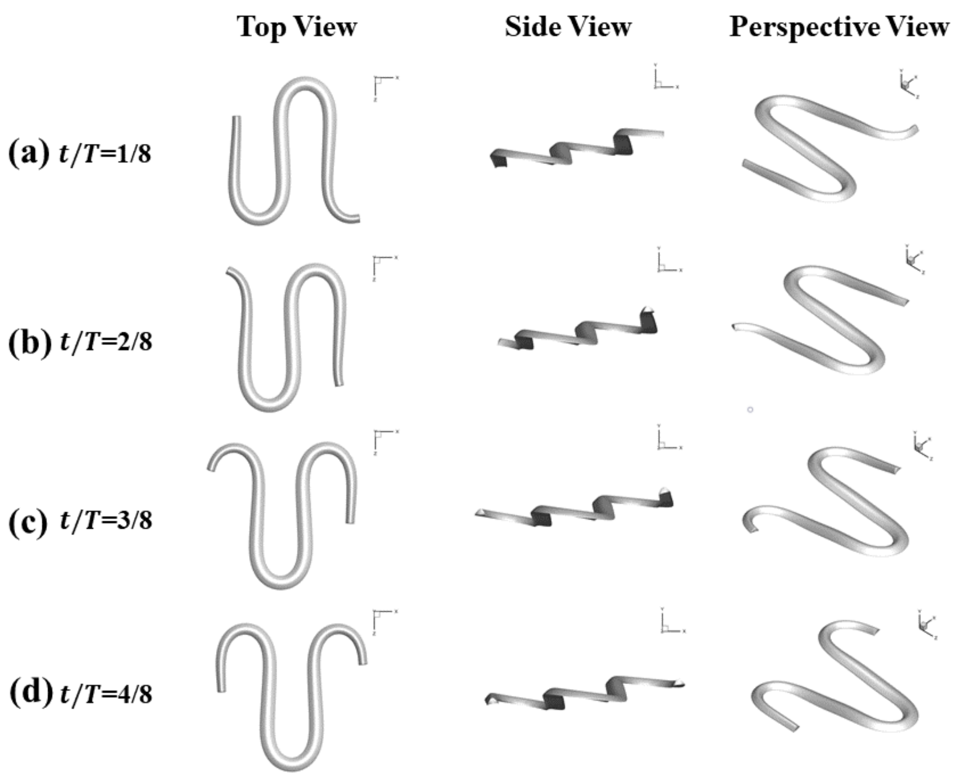

FIGURE A.4: Top, side perspective view for the dorsal-ventral bending model (Model 4: $\psi_{DV} = -5°$) at (a) t/T=1/8, (b) t/T=2/8, (c) t/T=3/8 and (d) t/T=4/8, respectively.T he horizontal undulation and the vertical wave undulation are not changed.

Bibliography

[1] R. Dudley, G. Byrnes, S. P. Yanoviak, B. Borrell, R. M. Brown, and J. A. McGuire, “Gliding and the functional origins of flight: Biomechanical novelty or necessity?” *Annual Review of Ecology, Evolution, and Systematics*, pp. 179–201, 2007.

[2] J. J. Socha, K. Miklasz, F. Jafari, and P. P. Vlachos, “Non-equilibrium trajectory dynamics and the kinematics of gliding in a flying snake,” *Bioinspiration & biomimetics*, vol. 5, no. 4, p. 045 002, 2010.

[3] J. Davenport, “How and why do flying fish fly?” *Reviews in Fish Biology and Fisheries*, vol. 4, pp. 184–214, 1994.

[4] K. L. Bishop, “The evolution of flight in bats: Narrowing the field of plausible hypotheses,” *The Quarterly Review of Biology*, 2008, Volume and pages information not provided.

[5] G. Byrnes, N. T. L. Lim, and A. J. Spence, “Takeoff and landing kinetics of a free-ranging gliding mammal, the malayan colugo (galeopterus variegatus),” *Proceedings of the Royal Society B: Biological Sciences*, vol. 275, pp. 1007–1013, 2008.

[6] S. B. Emerson and M. A. R. Koehl, “The interaction of behavioral and morphological change in the evolution of a novel locomotor type: ‘flying’ frogs,” *Evolution*, vol. 44, pp. 1931–1946, 1990.

[7] A. P. Russell and L. D. Dijkstra, “Patagial morphology of draco volans (reptilia: Agamidae) and the origin of glissant locomotion in flying dragons,” *Journal of Zoology*, vol. 253, pp. 457–471, 2001.

[8] J. J. Socha, “Gliding flight in chrysopelea: Turning a snake into a wing,” *Integrative and Comparative Biology*, vol. 51, no. 6, pp. 969–982, 2011.

[9] A. Jusufi, D. I. Goldman, S. Revzen, and R. J. Full, “Active tails enhance arboreal acrobatics in geckos,” *Proceedings of the National Academy of Sciences*, vol. 105, pp. 4215–4219, 2008.

[10] S. P. Yanoviak, B. L. Fisher, and A. Alonso, “Directed aerial descent behavior in african canopy ants (hymenoptera: Formicidae),” *Journal of Insect Behavior*, vol. 21, pp. 164–171, 2008.

[11] J. J. Socha, F. Jafari, Y. Munk, and G. Byrnes, “How animals glide: From trajectory to morphology,” *Canadian Journal of Zoology*, vol. 93, no. 12, pp. 901–924, 2015.

[12] J. J. Socha, T. O’Dempsey, and M. LaBarbera, “A 3-d kinematic analysis of gliding in a flying snake, chrysopelea paradisi,” *Journal of Experimental Biology*, vol. 208, no. 10, pp. 1817–1833, 2005.

[13] J. W. Bahlman, S. M. Swartz, D. K. Riskin, and K. S. Breuer, “Glide performance and aerodynamics of non-equilibrium glides in northern flying squirrels (glaucomys sabrinus),” *Journal of the Royal Society interface*, vol. 10, no. 80, p. 20 120 794, 2013.

[14] A. Hedenström and L. C. Johansson, “Bat flight: Aerodynamics, kinematics and flight morphology,” *The Journal of experimental biology*, vol. 218, no. 5, pp. 653–663, 2015.

[15] M. G. McCAY, “Aerodynamic stability and maneuverability of the gliding frog polypedates dennysi,” *Journal of Experimental Biology*, vol. 204, no. 16, pp. 2817–2826, 2001.

[16] W. Shyy, Y. Lian, J. Tang, D. Viieru, and H. Liu, "Aerodynamics of low reynolds number flyers," 2007, Journal information not provided.

[17] I. J. Yeaton, J. J. Socha, and S. D. Ross, "Global dynamics of non-equilibrium gliding in animals," *Bioinspiration & Biomimetics*, vol. 12, no. 2, p. 026 013, 2017.

[18] R. J. Humphrey, G. K. Taylor, and A. L. R. Thomas, "Smoke visualization of free-flying bumblebees indicates independent leading-edge vortices on each wing pair," *Experiments in Fluids*, vol. 46, pp. 811–821, 2009.

[19] C. P. Ellington, C. van den Berg, A. P. Willmott, and A. L. R. Thomas, "Leading-edge vortices in insect flight," *Nature*, vol. 384, pp. 626–630, 1996.

[20] R. J. Humphrey, T. Nakata, P. Henningsson, and H.-T. Lin, "Flight of the dragonflies and damselflies," *Philosophical Transactions of the Royal Society B: Biological Sciences*, vol. 371, 2016.

[21] D. R. Warrick, B. W. Tobalske, and D. R. Powers, "Lift production in the hovering hummingbird," *Proceedings of the Royal Society B: Biological Sciences*, vol. 276, no. 1674, pp. 3747–3752, 2009.

[22] S. P. Sane, "The aerodynamics of insect flight," *The Journal of Experimental Biology*, vol. 206, pp. 4191–4208, 2003.

[23] D. D. Chin and D. Lentink, "Flapping wing aerodynamics: From insects to vertebrates," *Journal of Experimental Biology*, vol. 219, pp. 920–932, 2016.

[24] G. Liu, H. Dong, and C. Li, "Vortex dynamics and new lift enhancement mechanism of wing–body interaction in insect forward flight," *Journal of Fluid Mechanics*, vol. 795, pp. 634–651, 2016.

[25] J. D. Eldredge and A. R. Jones, “Leading-edge vortices: Mechanics and modeling,” *Annual Review of Fluid Mechanics*, vol. 51, pp. 75–104, 2019.

[26] F. Manar, P. Mancini, D. Mayo, and A. R. Jones, “Comparison of rotating and translating wings: Force production and vortex characteristics,” *AIAA Journal*, vol. 54, no. 2, pp. 519–530, 2016.

[27] K. K. Chen, T. Colonius, and K. Taira, “The leading-edge vortex and quasi-steady vortex shedding on an accelerating plate,” *Physics of Fluids*, vol. 22, no. 3, pp. 1–11, 2010.

[28] J. R. Usherwood and C. P. Ellington, “The aerodynamics of revolving wings i. model hawkmoth wings,” *Journal of Experimental Biology*, pp. 1547–1564, 2002.

[29] D. J. Garmann and M. R. Visbal, “Dynamics of revolving wings for various aspect ratios,” *Journal of Fluid Mechanics*, vol. 748, pp. 932–956, 2014.

[30] I. J. Yeaton, S. D. Ross, G. A. Baumgardner, and J. J. Socha, “Undulation enables gliding in flying snakes,” *Nature Physics*, vol. 16, no. 9, pp. 974–982, 2020.

[31] K Miklasz, M LaBarbera, X Chen, and J. Socha, “Effects of body cross-sectional shape on flying snake aerodynamics,” *Experimental Mechanics*, vol. 50, no. 9, pp. 1335–1348, 2010.

[32] F. Jafari, D. Holden, R. LaFoy, P. P. Vlachos, and J. J. Socha, “The aerodynamics of flying snake airfoils in tandem configuration,” *Journal of Experimental Biology*, vol. 224, no. 14, jeb233635, 2021.

[33] Y. Gong and H. Dong, “Computation study about the interaction between the tandem flying snake airfoils with dynamic motion,” in *AIAA SCITECH 2023 Forum*, 2023, p. 2460.

[34] M. H. Dickinson, "Haltere–mediated equilibrium reflexes of the fruit fly, drosophila melanogaster," *Philosophical Transactions of the Royal Society of London. Series B: Biological Sciences*, vol. 354, no. 1385, pp. 903–916, 1999.

[35] R. Dudley, *The biomechanics of insect flight: form, function, evolution*. Princeton university press, 2002.

[36] J. A. Bender and M. H. Dickinson, "A comparison of visual and haltere-mediated feedback in the control of body saccades in drosophila melanogaster," *Journal of Experimental Biology*, vol. 209, no. 23, pp. 4597–4606, 2006.

[37] G. K. Taylor and H. G. Krapp, "Sensory systems and flight stability: What do insects measure and why?" *Advances in insect physiology*, vol. 34, pp. 231–316, 2007.

[38] Y.-L. Zhang and M. Sun, "Stabilization control of a hovering model insect: Lateral motion," *Acta Mechanica Sinica*, vol. 27, no. 5, pp. 823–832, 2011.

[39] B. Cheng and X. Deng, "Translational and rotational damping of flapping flight and its dynamics and stability at hovering," *IEEE Transactions on Robotics*, vol. 27, no. 5, pp. 849–864, 2011.

[40] M. Di Luca, S. Mintchev, G. Heitz, F. Noca, and D. Floreano, "Bioinspired morphing wings for extended flight envelope and roll control of small drones," *Interface focus*, vol. 7, no. 1, p. 20 160 092, 2017.

[41] F. Jafari, S. D. Ross, P. P. Vlachos, and J. J. Socha, "A theoretical analysis of pitch stability during gliding in flying snakes," *Bioinspiration & Biomimetics*, vol. 9, no. 2, p. 025 014, 2014.

[42] D. Holden, J. J. Socha, N. D. Cardwell, and P. P. Vlachos, "Aerodynamics of the flying snake chrysopelea paradisi: How a bluff body cross-sectional shape contributes to gliding performance," *Journal of Experimental Biology*, vol. 217, no. 3, pp. 382–394, 2014.

[43] A. Krishnan, J. J. Socha, P. P. Vlachos, and L. Barba, "Lift and wakes of flying snakes," *Physics of Fluids*, vol. 26, no. 3, p. 031 901, 2014.

[44] A. Menzer, Y. Gong, F. E. Fish, and H. Dong, "Bio-Inspired Propulsion : Towards Understanding the Role of Pectoral Fin Kinematics in Manta-like Swimming," *Biomimetics*, vol. 7, no. 45, 2022.

[45] G. Liu, Y. Ren, H. Dong, O. Akanyeti, J. C. Liao, and G. V. Lauder, "Computational analysis of vortex dynamics and performance enhancement due to body-fin and fin-fin interactions in fish-like locomotion," *Journal of Fluid Mechanics*, vol. 829, pp. 65–88, 2017.

[46] J. Wang, D. K. Wainwright, R. E. Lindengren, G. V. Lauder, and H. Dong, "Tuna locomotion: A computational hydrodynamic analysis of finlet function," *Journal of the Royal Society Interface*, vol. 17, no. 165, 2020.

[47] P. Han, G. Liu, Y. Ren, and H. Dong, "Computational Analysis of 3D Fin-Fin Interaction In Fish's Steady Swimming," *FEDSM2016*, pp. 1–6, 2016.

[48] Z. Huang, A. Menzer, J. Guo, and H. Dong, "Hydrodynamic analysis of fin–fin interactions in two-manta-ray schooling in the vertical plane," *Bioinspiration & Biomimetics*, vol. 19, no. 2, p. 026 004, 2024.

[49] J. Guo, P. Han, W. Zhang, *et al.*, "Vortex dynamics and fin-fin interactions resulting in performance enhancement in fish-like propulsion," *Physical Review Fluids*, vol. 8, no. 7, p. 073 101, 2023.

[50] A. Menzer, Y. Ren, J. Guo, B. W. Tobalske, and H. Dong, "Wing kinematics and unsteady aerodynamics of a hummingbird pure yawing maneuver," *Biomimetics*, vol. 7, no. 3, p. 115, 2022.

[51] J. Wang, Y. Ren, C. Li, and H. Dong, "Computational investigation of wing-body interaction and its lift enhancement effect in hummingbird forward flight," *Bioinspiration & biomimetics*, vol. 14, no. 4, p. 046 010, 2019.

[52] A. T. Bode-Oke, S. Zeyghami, and H. Dong, "Flying in reverse: Kinematics and aerodynamics of a dragonfly in backward free flight," *Journal of The Royal Society Interface*, vol. 15, no. 143, p. 20 180 102, 2018.

[53] A. T. Bode-Oke and H. Dong, "The reverse flight of a monarch butterfly (danaus plexippus) is characterized by a weight-supporting upstroke and postural changes," *Journal of the Royal Society Interface*, vol. 17, no. 167, p. 20 200 268, 2020.

[54] J. Kelly, H. Pan, H. Dong, and T. Van Buren, "Wake Structures and Effect of Hydrofoil Shapes in Efficient Flapping Propulsion," *FEDSM2021*, pp. 1–7, 2021.

[55] P. Han, Y. Pan, G. Liu, and H. Dong, "Propulsive performance and vortex wakes of multiple tandem foils pitching in-line," *Journal of Fluids and Structures*, vol. 108, p. 103 422, 2022.

[56] J. Kelly, Y. Pan, and H. Dong, "Body Shape Effects on the Hydrodynamic Performance of Bio-Inspired Undulating Swimmers," *FEDSM2022*, pp. 1–6, 2022.

[57] M. S. U. Khalid, J. Wang, H. Dong, and M. Liu, "Flow transitions and mapping for undulating swimmers," *Physical Review Fluids*, vol. 5, no. 6, p. 63 104, 2020.

[58] C. Li, H. Dong, and G. Liu, “Effects of a dynamic trailing-edge flap on the aerodynamic performance and flow structures in hovering flight,” *Journal of Fluids and Structures*, vol. 58, pp. 49–65, 2015.

[59] M. Bozkurttas, H. Dong, V. Seshadri, R. Mittal, and F. Najjar, “Towards numerical simulation of flapping foils on fixed cartesian grids,” *43rd AIAA Aerospace Sciences Meeting and Exhibit - Meeting Papers*, no. December 2014, pp. 15 801–15 809, 2005.

[60] R. Mittal, H. Dong, M. Bozkurttas, F. M. Najjar, A. Vargas, and A. von Loebbecke, “A versatile sharp interface immersed boundary method for incompressible flows with complex boundaries,” *Journal of Computational Physics*, vol. 227, no. 10, pp. 4825–4852, 2008.

[61] J. M. Birch, W. B. Dickson, and M. H. Dickinson, “Force production and flow structure of the leading edge vortex on flapping wings at high and low reynolds numbers,” *Journal of Experimental Biology*, vol. 207, no. 7, pp. 1063–1072, 2004.

[62] C. Koehler, Z. Liang, Z. Gaston, H. Wan, and H. Dong, “3d reconstruction and analysis of wing deformation in free-flying dragonflies,” *Journal of Experimental Biology*, vol. 215, no. 17, pp. 3018–3027, 2012.

[63] J. Guo, W. Zhang, P. Han, F. E. Fish, and H. Dong, “Thrust generation and propulsive efficiency in dolphin-like swimming propulsion,” *Bioinspiration & Biomimetics*, vol. 18, no. 5, p. 056 001, 2023.

[64] F. Jafari, S. Tahmasian, S. D. Ross, and J. J. Socha, “Control of gliding in a flying snake-inspired n-chain model,” *Bioinspiration & biomimetics*, vol. 12, no. 6, p. 066 002, 2017.

[65] W. Zhang, Y. Pan, J. Wang, V. Di Santo, G. V. Lauder, and H. Dong, "An efficient tree-topological local mesh refinement on cartesian grids for multiple moving objects in incompressible flow," *Journal of Computational Physics*, p. 111 983, 2023.

[66] Y. Gong, J. Wang, W. Zhang, J. J. Socha, and H. Dong, "Computational analysis of vortex dynamics and aerodynamic performance in flying-snake-like gliding flight with horizontal undulation," *Physics of Fluids*, vol. 34, no. 12, p. 121 907, 2022.

[67] K. Taira and T. Colonius, "Three-dimensional flows around low-aspect-ratio flat-plate wings at low reynolds numbers," *Journal of Fluid Mechanics*, vol. 623, pp. 187–207, 2009.

[68] C. Li, H. Dong, and B. Cheng, "Tip vortices formation and evolution of rotating wings at low reynolds numbers," *Physics of Fluids*, vol. 32, no. 2, 2020.

[69] J.-m. Zhan, Y.-t. Li, W.-h. O. Wai, and W.-q. Hu, "Comparison between the q criterion and rortex in the application of an in-stream structure," *Physics of Fluids*, vol. 31, no. 12, 2019.

[70] Y. Gong, J. Wang, J. Socha, and H. Dong, "Aerodynamics and flow characteristics of flying snake gliding with undulating locomotion," in *AIAA SCITECH 2022 Forum*, 2022, p. 1054.

[71] P. C. Khandelwal and T. L. Hedrick, "Combined effects of body posture and three-dimensional wing shape enable efficient gliding in flying lizards," *Scientific reports*, vol. 12, no. 1, p. 1793, 2022.

[72] S. Vogel, *Life in moving fluids: the physical biology of flow-revised and expanded second edition*. Princeton university press, 2020.

[73] C. Wang, Z. Xu, X. Zhang, and S. Wang, "Optimal reduced frequency for the power efficiency of a flat plate gliding with spanwise oscillations," *Physics of Fluids*, vol. 33, no. 11, 2021.

[74] J. C. Hunt, A. A. Wray, and P. Moin, "Eddies, streams, and convergence zones in turbulent flows," *Studying turbulence using numerical simulation databases, 2. Proceedings of the 1988 summer program*, 1988.

[75] D. T. McRuer, D. Graham, and I. Ashkenas, *Aircraft dynamics and automatic control*. Princeton University Press, 2014, vol. 2731.

[76] J. D. Anderson and M. L. Bowden, *Introduction to flight*. McGraw-Hill Higher Education New York, NY, USA, 2005, vol. 582.

[77] C. Carpenter, *Flightwise: Aircraft stability and control*. Airlife Publishing, 1997, vol. 2.

[78] C. Palmer, "The aerodynamics of gliding flight and its application to the arboreal flight of the chinese feathered dinosaur microraptor," *Biological Journal of the Linnean Society*, vol. 113, no. 3, pp. 828–835, 2014.

[79] H. Park and H. Choi, "Aerodynamic characteristics of flying fish in gliding flight," *Journal of Experimental Biology*, vol. 213, no. 19, pp. 3269–3279, 2010.

[80] J. A. Rader, T. L. Hedrick, Y. He, and L. D. Waldrop, "Functional morphology of gliding flight ii. morphology follows predictions of gliding performance," *Integrative and Comparative Biology*, vol. 60, no. 5, pp. 1297–1308, 2020.

[81] A. M. Heers, B. W. Tobalske, and K. P. Dial, "Ontogeny of lift and drag production in ground birds," *Journal of Experimental Biology*, vol. 214, no. 5, pp. 717–725, 2011.

[82] V. A. Tucker, "The effect of molting on the gliding performance of a harris' hawk (parabuteo unicinctus)," *The Auk*, vol. 108, no. 1, pp. 108–113, 1991.

[83] D. D. Chin and D. Lentink, "Birds both avoid and control collisions by harnessing visually guided force vectoring," *Journal of the Royal Society Interface*, vol. 19, no. 191, p. 20 210 947, 2022.

[84] B. Tucker and A. Conlisk, "Massive vortex motion in the presence of solid boundaries," *Physics of Fluids A: Fluid Dynamics*, vol. 4, no. 2, pp. 290–305, 1992.

[85] S. Ziada and D. Rockwell, "Vortex–leading-edge interaction," *Journal of Fluid Mechanics*, vol. 118, pp. 79–107, 1982.

[86] D. Rockwell, "Vortex-body interactions," *Annual review of fluid mechanics*, vol. 30, p. 199, 1998.